Diploma Thesis

Excitation Modes for the Cooling of the Ion motion in Penning Traps

Marco Rosenbusch

Institute of Physics
Ernst-Moritz-Arndt-University Greifswald

October 5, 2009

Contents

1 Introduction **11**

2 Theoretical Background **15**
2.1 The Eigenfrequencies of Charged Particles in the Ideal Penning Trap . . 15
2.2 Motion in the Ideal Penning Trap 17
2.3 Ion Motion with Excitations 19
2.3.1 Dipolar Excitation 20
2.3.2 Circularly Polarized Dipolar Excitation 22
2.3.3 Quadrupolar Excitation 23
2.3.4 Phase Dependency of Quadrupolar Excitation 24
2.3.5 Non Resonant Quadrupolar Excitation 25
2.3.6 Circularly Polarized Quadrupolar excitation 26
2.4 Ion Motion with Damping 28
2.4.1 Buffer Gas and Quadrupolar excitation 29
2.4.2 Resolving Power above the Fourier Limit by Radial Selection of Ions 32
2.5 Octupolar Excitation 33
2.5.1 Phase Dependency of an Octupolar Excitation 34
2.5.2 Octupolar Resonance Curves 35

3 Simulations **39**
3.1 Fifth order Gear Method 39
3.2 Test of the Gear method 40
3.3 Realistic Damping Approaches 41
3.3.1 Realistic Continuous Model with a Velocity Dependent Mobility 42
3.3.2 Elastic Collisions with Buffer Gas Atoms 43
3.4 Comparison of the OES and the QES in a Simulation for the Cooling Process 45
3.4.1 Procedure and Initial Conditions 45
3.4.2 Bisection Method and Resonance Shapes 47
3.4.3 Results for R_p and the efficiency from the Simulations with a continuous damping model $\delta = \delta(T_{\text{eff}})$ 48
3.4.4 Results for R_p and the efficiency from the Simulations with Elastic Collisions 50
3.4.5 Results for the Centering Quality from Both Simulations 52

4 Experimental Setup **55**
4.1 The ISOLTRAP Experiment 55
4.2 RFQ Buncher 56

4.3 Preparation Penning Trap 57
4.4 Precision Penning Trap and Discussion of the Mass Measurements . . . 58
4.5 Off-Line Reference Ion Sources 61
4.6 Experimental Setup for the Investigation of Excitation Modes in Cooling Processes 62
4.7 Procedure and Time Structure for the Measurement of Cooling Resonances 62
4.8 Application of Excitation schemes 65

5 Measurements and Discussion **71**
5.1 Investigation of Circularly Polarized Excitation Schemes 71
5.1.1 Confirmation of the Predictions for the CPDES 71
5.1.2 Confirmations of the Predictions for the CPQES 72
5.2 Test of the Ion cooling with Octupolar Excitation 74
5.3 Discussion of OES and QES in cooling processes 76
5.3.1 Amplitude Scans with the Resonance Frequency 76
5.3.2 Cooling Resonances as a Function of the Excitation Amplitude at a Pressure of $p = 3.0 \cdot 10^{-7}$ mbar 79
5.3.3 Cooling Resonances for Different Excitation Amplitudes and Pressures 80
5.3.4 Maximal Resolving Power as a Function of the Pressure 84
5.3.5 Maximal Resolving Power as a Function of the Excitation Time . 85
5.4 Energy Distribution of Pre-Cooled Ions 88
5.5 Test of the Conservation of the Motional Phases in a Buffer Gas Environment 90

6 Summary and Outlook **93**

A Solution of the Equations of motion in the Quadrupolar excitation scheme **95**

List of Figures

1.1 Sketch of the ISOLDE facility at CERN 12

2.1 Principle of the Penning trap 16
2.2 Eigenmotions of a charged particle in the Penning trap 19
2.3 Motion with dipolar excitation 21
2.4 Comparison of the motions in a linear and a circularly polarized dipolar excitation scheme 22
2.5 Conversion of the radial eigenmotions 24
2.6 Structure of quadrupolar resonance shapes for different amplitudes . . . 26
2.7 Comparison of the conversions in a linear and a circularly polarized quadrupolar excitation scheme 28
2.8 Damped motion of a particle in the xy-plane 29
2.9 Radii of quadrupolar excited ions as a function of the time with different pressures 30
2.10 Ion motion with damping and quadrupolar excitation 31
2.11 Resolving Power above the Fourier limit with a radial selection of ions . 32
2.12 Conversion of the radial eigenmotions in an octupolar excitation scheme 34
2.13 Radial energy as a function of time for different initial phases in an octupolar excitation scheme 35
2.14 Resonance shapes of the octupolar excitation scheme with different amplitudes and phases 36
2.15 Two dimensional cuts from octupolar resonance shapes 37
2.16 Dependency of the normalized width of octupolar resonance shapes on T_{exc} 38

3.1 Test of the fifth order Gear method 41
3.2 omparison of different damping schemes 44
3.3 Sketch for the determination of the efficiency and the average radius of the ions 45
3.4 Bisection algorithm for the determination of R_p 47
3.5 Numerical problems for the bisection method with resonance shapes . . 47
3.6 Resolving power and efficiency from the simulation with continuous damping 49
3.7 Conversion of spacial distributed ions with both excitation schemes . . . 50
3.8 Resolving power and efficiency from the simulation with elastic collisions 51
3.9 Radial motion of ions with collisions for both excitation schemes 52
3.10 Reciprocal of $\overline{\rho_{-,\mathrm{f}}}$ from both simulations and both excitation schemes . 53

4.1 Experimental setup of ISOLTRAP 56

4.2 Photo of the Preparation Penning Trap and sketch of the construction . 57
4.3 Photo of the Precision Penning Trap 59
4.4 Sketch of the Precision Penning Trap and the magnetic field gradient in the ToF section 59
4.5 ToF resonance for $^{229}Rn^{+}$ ions 60
4.6 Schematic sketch of the ISOLTRAP beam line with the reference ion sources 61
4.7 Sketch of the reference ion sources at ISOLTRAP 62
4.8 ISOLTRAP section with the Preparation Penning Trap and MCP detector 63
4.9 Typical ToF spectrum for cooled ions 64
4.10 Time structure of an experimental cycle in a cooling resonance measurement 65
4.11 Electrode allocation for the circularly polarized dipolar excitation scheme 67
4.12 Electrode allocation for the circularly polarized quadrupolar excitation scheme 68
4.13 Electrode allocation for the octupolar excitation scheme 69

5.1 Amplitude scan with a CPDES and a LPDES 72
5.2 Amplitude scan with a CPQES and a LPQES 73
5.3 Cooling resonance with a CPQES and a LPQES 74
5.4 Amplitude scan and cooling resonance with an OES 75
5.5 Amplitude scans for a QES for four different pressures 77
5.6 Amplitude scans for an OES for four different pressures 78
5.7 Resolving power as a function of the amplitude with a low pressure and small amplitude steps 79
5.8 Resolving power and efficiency for a pressure of $6.0 \cdot 10^{-7}$ mbar and $3.0 \cdot 10^{-7}$ mbar 81
5.9 Octupolar resonance curve with a pressure of $p = 3.0 \cdot 10^{-7}$ mbar 82
5.10 Resolving power and efficiency for a pressure of $p = 1.7 \cdot 10^{-6}$ mbar and $p = 1.2 \cdot 10^{-6}$ mbar 83
5.11 Resolving power as a function of the pressure 84
5.12 Resolving power of the QES as a function of the excitation duration at different pressures 85
5.13 Quadrupolar resonance curve with $p = 3.0 \cdot 10^{-7}$ mbar and $T_{exc} = 500$ ms 86
5.14 Resolving power of the OES in dependency of the excitation duration at different pressures 87
5.15 Octupolar resonance curve with $p = 3.0 \cdot 10^{-7}$ mbar and $T_{exc} = 750$ ms . 87
5.16 Ion energy distribution at the precision trap, I 88
5.17 Ion energy distribution at the precision trap, II 89
5.18 Excitation with two dipolar signals and a variable Waiting time in between 90
5.19 Determination of the reduced cyclotron phase conservation time in a buffer gas 91

List of Tables

3.1 Simulated bunch width of pre-cooled ions for three different pressures . 46

4.1 Voltages at the electrodes of the Preparation Penning Trap 58
4.2 List of the devices for the present measurements 66

5.1 Fit of the simulated pressures to the measured pressures 76
5.2 Waiting-time settings for the OES and the QES 81
5.3 Measured conservation times for the phase of the reduced cyclotron motion 92

List of Variables, Symbols, and Abbreviations

E	Energy
E_ρ	Radial Energy
K	Mobility of an Ion in a Buffer Gas
M	Mass of the Buffer Gas Atoms
N_{ion}	Ion Number
P	Probability
R_p	Resolving Power
T_+	Periodic Time of the Reduced Cyclotron Motion
T_-	Periodic Time of the Magnetron Motion
T_{eff}	Effective Temperature
U_{B}	Minimal Applied Voltage to Perform a Complete Conversion
U_{d}	Applied Voltage for a Dipolar Excitation
U_{exc}	Applied Voltage an Excitation in General
U_{oct}	Applied Voltage for a Octupolar Excitation
U_{q}	Applied Voltage for a Quadrupolar Excitation
$\Delta\nu_{\mathrm{D}}$	Width of a Resonance at the Diaphragm Radius
$\Delta\nu_{\mathrm{H}}$	Full Width at Half Maximum of a Resonance
Ω	Total Collision Cross Section
Θ	Scattering Angle
δ	Damping Parameter
γ	Modified Damping Parameter in V-Notation $\gamma = \frac{\delta}{\omega_+ - \omega_-}$
$\hat{\rho}$	Unit Vector in Radial Direction, $\hat{\rho} = (\hat{x} + \hat{y})/\sqrt{2}$
$\hat{e}_{\mathrm{rand}}$	Unit Vector in (x, y, z) with a Random Direction
$\hat{x}, \hat{y}, \hat{z}$	Unit Vector in (x, y, z)-Direction
u	Atomic Mass Unit
ν_+	Reduced Cyclotron Frequency
ν_-	Magnetron Frequency
ν_{B}	Beating Frequency
ν_{d}	Dipolar Excitation Frequency
ν_{exc}	Excitation Frequency in General
ν_{ion}	Determined Cyclotron Frequency of the Ion of Interest
ν_{oct}	Octupolar Excitation Frequency
ν_{q}	Quadrupolar Excitation Frequency
ν_{ref}	Determined Cyclotron Frequency of the Reference Ion
ν_c	Cyclotron Frequency
ω_i	Corresponding angular frequency of ν_i
ρ	Total Distance from the Trap Center

ρ_+	Cyclotron Radius
ρ_-	Magnetron Radius
$\rho_{-,\mathrm{f}}$	Final Magnetron Radius after the Cooling Process
ρ_D	Radius of the Diaphragm of the Preparation Penning Trap
$\vec{E}$	Electrical Field Vector
$\vec{F}$	Force Vector
$\vec{V}\pm$	Transformed Velocity Vectors
$\vec{\rho}$	Radial Position Vector in x, y-Direction
$\vec{r}$	Cartesian Position Vector
$\vec{v}$	Velocity Vector
$\vec{v}_\mathrm{d}$	Drift Velocity Vector of an Ion in a Buffer Gas
$\widetilde{\nu}_c$	Expected Cyclotron Frequency
b	Impact Parameter
k_0	Parameter for the strength of the Excitation
k_B	Bolzmann Constant
m	Mass of the Charged Particle
m_ion	Determined Mass of the Ion of Interest
m_ref	Mass of the Reference Ion
n_gas	Density of the Buffer Gas
p	Pressure
q	Electrical Charge
v_d	Drift Velocity of Ions in a Buffer Gas
x, y, z	Position in (x, y, z)-Direction
FWHM	Full Width at Half Maximum

1 Introduction

The knowledge of the binding energy of atomic nuclei is a key for the understanding of fundamental properties of the matter, since all interaction forces are involved. The properties of nuclei are studied in different disciplines of physics research on nuclear fine structure, weak interaction studies, and others [Bla06]. The binding energy and thus all properties of a nucleus are directly related to the mass via Einstein's relation $E = mc^2$. The highly precise determination of nuclear masses is therefore an important topic for experimental nuclear physics. Especially short-lived nuclei far away from stability are of high interest, because they allow one to observe nuclear structure effects, deformation effects, or pairing effects [MBB$^+$08]. For example in astrophysics, the masses of short lived nuclei are of great importance for research on the rapid neutron [DAB$^+$06],[BAB$^+$08] and rapid-proton capture process [RKA$^+$05],[HAB$^+$04].
ISOLTRAP [MBB$^+$08] is a Penning trap experiment, located at the radioactive ion beam facility ISOLDE at CERN. It has been developed for high precision mass measurements of short lived nuclei, far away from stability, via determining their cyclotron frequency

$$\nu_c = \frac{q \cdot B}{2\pi m}, \tag{1.1}$$

with q as the charge of the ion, m as the mass, and B as the strength of the magnetic field. More than 400 different masses with half-lives down to 65 ms [KAB$^+$04] have been determined. These mass measurements have been performed with a relative mass uncertainty down to $\delta m/m = 8 \cdot 10^{-9}$ [KBB$^+$03]. The required ions for the experiments are produced in the ISOLDE facility, which is illustrated in Fig. 1.1. The main components of the facility are a target area, two mass seperators (GPS (General Purpose Separator) and the HRS (High Resolution Separator)), and an experimental hall with several beam lines and dedicated experimental setups. A highly energetic proton beam hits a thick target [Kug00] (e.g. uranium carbide), whereby many different radioactive nuclides are produced as atoms. These atoms are later ionized, accelerated and separated in one of the two mass separators. These separators have a resolving power of up to $R_p = m/\delta m \approx 1000$ for the GPS, and $R_p \approx 5000$ for the HRS. Thus, the separators are suitable to isolate a single mass number, but other isobars and, in addition, long-lived isomeric states are not always resolved. The rate of contaminants depends on several parameters in the ionization process and the production cross-sections of the nuclei. To avoid frequency shifts due to the interaction with different ion species, the ensemble has to be purified from contaminants. At ISOLTRAP this is performed with a cylindrical Preparation Penning Trap, where the so-called buffer gas cooling technique is applied [SBB$^+$91]. A dipolar field drives all ions out of the trap center to a larger radius. A further excitation with an oscillating quadrupolar field at the cyclotron frequency ν_c of the ions of interest is exciting the ions motion, so that they are moved to the center of the trap in presence of a buffer gas. Afterwards they can pass a diaphragm towards the

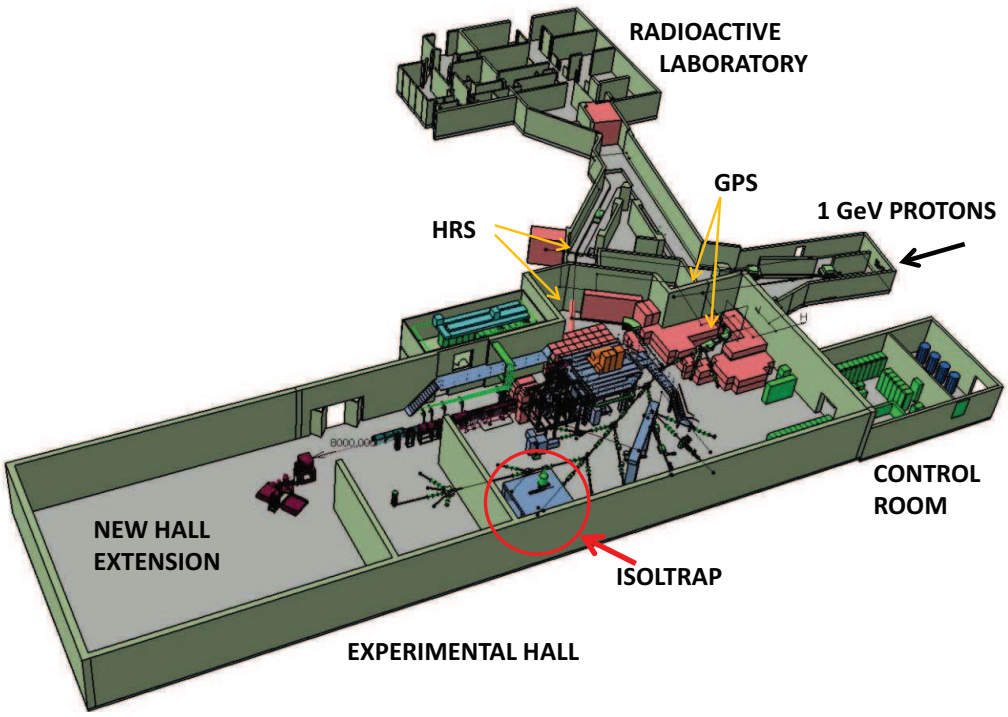

Figure 1.1: Sketch of the ISOLDE facility at CERN with the ISOLTRAP mass spectrometer.

next experimental step. This technique allows one to cool ions mass selectively with a resolving power of $R_p = \delta m/m = \nu_c/\Delta\nu_{\mathrm{H}} \approx 10^5$, where $\Delta\nu_{\mathrm{H}}$ is the uncertainty of the frequency. For a subsequent successful mass measurement on short-lived nuclei, four aspects have to be considered:

1. For many kinds of contaminants, especially many isomeric states, a high resolving power is required to purify the ions of interest. As an example, for the chain $^{210}\mathrm{Pb}^+$ to $^{214}\mathrm{Pb}^+$, the required resolving power is increasing fast with the mass number. For $^{210}\mathrm{Pb}^+$ a resolving power of 30000 is needed, whereas for $^{211}\mathrm{Pb}^+$, one needs $R_p = 100000$, and for $^{214}\mathrm{Pb}^+$, $R_p = 500000$ is required.

2. If the ions of interest are rarely present in the ensemble delivered from ISOLDE as $^{130}\mathrm{Cd}^+$, which is contaminated with much more $^{130}\mathrm{Cs}^+$, a high efficiency of the cooling process is necessary in order not to loose the rarely produced ions.

3. The time of the whole process is limited by the live time of the exotic ions.

4. To perform a precise mass measurement after the purification, the ions have to be well cooled and centered, since a large energy distribution causes also large uncertainties in the experimental results.

Under this thesis, the cooling and purification process in the Preparation Penning Trap of ISOLTRAP has been investigated. The attention is concentrated on the excitation modes. As an alternative to the commonly used dipolar and quadrupolar excitation scheme, a circularly polarized dipolar excitation scheme, a circularly polarized quadrupolar excitation scheme, and an octupolar excitation scheme is investigated for the cooling process by simulations and measurements. A motivation for the investigation of an octupolar excitation scheme is the fact that the resonance frequency $\nu_{\mathrm{oct}} = 2\nu_c$ [RBS$^+$07],[BAB$^+$08] causes a doubled resolving power $R_p = 2 \cdot \nu_c/\Delta\nu_H$ compared with the quadrupolar excitation scheme for the same resonance width $\Delta\nu_{\mathrm{H}}$. This is, in addition, an excitation mode which results in a nonlinear behavior of the ions, where the shape of resonance curves has a large spectrum. For well chosen conditions it is possible to achieve a much higher resolving power than in a quadrupolar excitation scheme [RBS$^+$07]. Therefore a simulation has been written which is specialized for a fast determination of the resolving power of excitation schemes and which is able to calculate the motion of ions under influence of collisions with neutral background atoms. Further the properties of the octupolar excitation scheme have been investigated in systematic measurements.

2 Theoretical Background

Penning traps allow a three dimensional confinement of charged particles. In the following ideal Penning traps are introduced as well as excitation schemes for manipulation of the ion ensembles. The purification and cooling of ions which is a fundamental technique to prepare ions for a precision measurement, will be discussed [BMSS90], [BG86]. Many diagrams in this chapter are illustrating examples which have been simulated. The simulations are described in 3.

2.1 The Eigenfrequencies of Charged Particles in the Ideal Penning Trap

In a Penning trap the confinement of charged particles is achieved by a magnetic field of the strength $\vec{B} = B\hat{z}$, with $\hat{z}$ as the unit vector in z-direction, superimposed with an axial quadrupolar field from hyperbolic electrodes as in Fig. 2.1. The quadrupolar potential in cylindrical coordinates with $\rho(x, y) = \sqrt{x^2 + y^2}$ is given by

$$\Phi(\rho, z) = \frac{U_0}{2d^2}\left(z^2 - \frac{\rho^2}{2}\right) \tag{2.1}$$

where d is the geometry parameter of the Penning trap $d^2 = \frac{1}{2}\left(r_0^2 + \frac{1}{2}z_0^2\right)$ [BG86]. The constants ρ_0 and z_0 describe the dimension of the trap where ρ_0 is the minimum distance between the trap center and the ring electrode and z_0 the minimum distance between the center and the endcaps.
The equation of motion for a particle of the mass m and the charge q is given by:

$$m\ddot{\vec{r}} = q\left(-\vec{\nabla}\Phi(\rho, z) + \dot{\vec{r}} \times \vec{B}\right) \tag{2.2}$$

with the components

$$\begin{aligned} \ddot{x} &= \omega_c\dot{y} + \frac{1}{2}\omega_z^2 x, \\ \ddot{y} &= -\omega_c\dot{x} + \frac{1}{2}\omega_z^2 y, \\ \ddot{z} &= -\omega_z^2 z. \end{aligned} \tag{2.3}$$

The frequency $\omega_c = \frac{q \cdot B}{m}$ is the cyclotron frequency of a charged particle in the magnetic field. The motion in z direction is decoupled from the magnetic field and the solution is a simple harmonic oscillation at the frequency $\omega_z = \sqrt{\frac{q}{m}\frac{U_0}{d^2}}$.
To derive the eigenfrequencies of the motions in the xy-plane, a complex variable $u =$

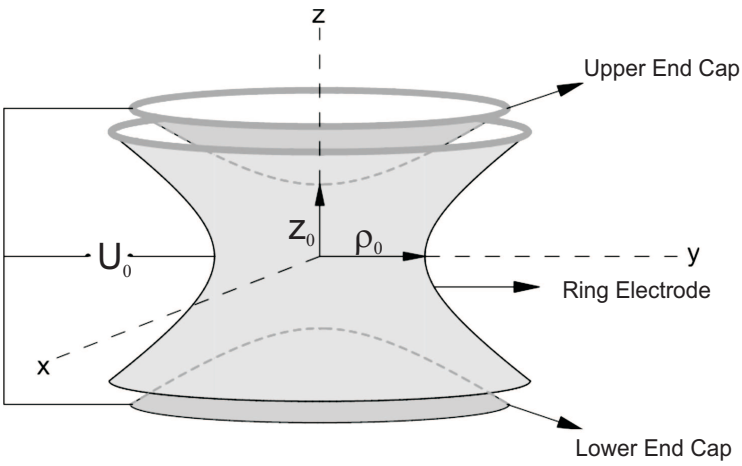

Figure 2.1: The principle of the Penning trap. A magnetic field is superimposed with an axial quadrupolar potential from hyperbolic electrodes.

$x + \mathrm{i}y$ is used [Kre91]. The x and y component of Eq. (2.3) are reduced to:

$$\ddot{u} + \mathrm{i}\omega_c \dot{u} - \frac{1}{2}\omega_z^2 u = 0. \tag{2.4}$$

With the ansatz $u = u_0 \cdot e^{\mathrm{i}\omega t}$ an equation for the radial eigenfrequencies is obtained:

$$\omega^2 - \omega_c \omega + \frac{1}{2}\omega_z^2 = 0. \tag{2.5}$$

Thus the radial eigenfrequencies are:

$$\omega_\pm = \frac{1}{2}\left(\omega_c \pm \sqrt{\omega_c^2 - 2\omega_z^2}\right). \tag{2.6}$$

The condition for eigenfrequencies with real values and thus the condition to trap ions is $\omega_c^2 - 2\omega_z^2 \geq 0$. The particle oscillates with three independent eigenmotions. The three eigenfrequencies fulfill the following relations:

$$\omega_c = \omega_+ + \omega_-, \tag{2.7}$$
$$\omega_c^2 = \omega_+^2 + \omega_-^2 + \omega_z^2, \tag{2.8}$$
$$\omega_z^2 = 2\omega_+\omega_-. \tag{2.9}$$

The charge of the particle is implemented in ω_c, which means that ω_c is positive for negative ions, and ω_c is negative for positive ions in the mathematical sense (counter clockwise). To fulfill the relation $\omega_c = \omega_+ + \omega_-$, the eigenfrequencies ω_+ and ω_- have the same sign as ω_c. In most mass spectrometry experiments the relations $\omega_- < \omega_z < \omega_+$

and also $\omega_z \ll \omega_c$ are fulfilled as well [SZBL95],[MF09]. For the latter relation the square root in Eq. (2.6) can be expanded to the first order:

$$\omega_+ \approx \omega_c - \frac{U_0}{2d^2B}, \tag{2.10}$$

$$\omega_- \approx \frac{U_0}{2d^2B}. \tag{2.11}$$

2.2 Motion in the Ideal Penning Trap

To solve the equations of motion a substitution is used which decouples the x and y component of Eq. (2.3) [BG86]. The velocity vectors $\vec{V}^{\pm}$ are introduced as follows:

$$\vec{V}^{\pm} = \dot{\vec{\rho}} - \omega_{\mp}\hat{z} \times \vec{\rho}, \tag{2.12}$$

with their components

$$\vec{V}^{\pm} = \begin{pmatrix} \dot{x} + \omega_{\mp} y \\ \dot{y} - \omega_{\mp} x \end{pmatrix}, \tag{2.13}$$

and the corresponding derivatives

$$\dot{\vec{V}}^{\pm} = \begin{pmatrix} \ddot{x} + \omega_{\mp} \dot{y} \\ \ddot{y} - \omega_{\mp} \dot{x} \end{pmatrix}. \tag{2.14}$$

If the frequency relations (2.7) and (2.9) are used in the radial part of Eq. (2.3) it follows that

$$\begin{aligned} \ddot{x} &= -\left(\omega_+ + \omega_-\right) \dot{y} + \omega_+ \omega_- x, \\ \ddot{y} &= \left(\omega_+ + \omega_-\right) \dot{x} + \omega_+ \omega_- y. \end{aligned} \tag{2.15}$$

In Eq. (2.14) and Eq. (2.15) there are two different expressions for each $\ddot{x}$ and $\ddot{y}$, and the combination with Eq. (2.13) gives

$$\begin{aligned} \ddot{x} &= \dot{V}_x^{\pm} - \omega_{\mp}\dot{y} = -((\omega_+ + \omega_-)\,\dot{y} - \omega_+\omega_- x) = -\omega_{\pm} V_y^{\pm} - \omega_{\mp}\dot{y}, \\ \ddot{y} &= \dot{V}_y^{\pm} + \omega_{\mp}\dot{x} = (\omega_+ + \omega_-)\,\dot{x} + \omega_+\omega_- y = \omega_{\pm} V_x^{\pm} + \omega_{\mp}\dot{x}. \end{aligned} \tag{2.16}$$

If the term $\omega_{\mp}\dot{y}$ is added to $\ddot{x}$ and $-\omega_{\mp}\dot{x}$ is added to $\ddot{y}$, the equation for $\dot{\vec{V}}^{\pm}$ is

$$\dot{\vec{V}}^{\pm} = \begin{pmatrix} 0 & -\omega_{\pm} \\ \omega_{\pm} & 0 \end{pmatrix} \vec{V}^{\pm}. \tag{2.17}$$

The second derivatives are therefore two independent equations for V^+ and V^-:

$$\ddot{\vec{V}}^{\pm} = -\omega_{\pm}^2 \vec{V}^{\pm}. \tag{2.18}$$

With the standard ansatz

$$\vec{V}^{\pm} = \vec{A}^{\pm} e^{\lambda t + \varphi_{\pm}}, \tag{2.19}$$

where

$$\begin{aligned} \lambda^2 &= -\omega_{\pm}^2, \\ \lambda &= \pm \mathrm{i}\omega_{\pm}, \end{aligned} \tag{2.20}$$

and with Eq. (2.17) it follows that

$$\pm \mathrm{i}\omega_{\pm} \vec{A}^{\pm} e^{\pm \mathrm{i}\omega_{\pm} t + \varphi_{\pm}} = \begin{pmatrix} 0 & -\omega_{\pm} \\ \omega_{\pm} & 0 \end{pmatrix} \vec{V}^{\pm}, \tag{2.21}$$

which leads to

$$A_x^{\pm} = \pm \mathrm{i} A_y^{\pm} = \pm \mathrm{i} A^{\pm}. \tag{2.22}$$

Thus, the solution of Eq. (2.17) is given by

$$\vec{V}^{\pm} = \begin{pmatrix} \pm \mathrm{i} \\ 1 \end{pmatrix} A^{\pm} e^{\pm \mathrm{i}(\omega_{\pm} t + \varphi_{\pm})}. \tag{2.23}$$

The velocity vectors $\vec{V}^{+}$ and $\vec{V}^{-}$ are rotating in opposite directions with respect to the frequencies ω_{+} and ω_{-}. To transform the vectors back into spacial coordinates x and y, Eq. (2.13) is used:

$$\begin{aligned} x &= -\frac{V_y^{+} - V_y^{-}}{\omega_{+} - \omega_{-}}, \\ y &= +\frac{V_x^{+} - V_x^{-}}{\omega_{+} - \omega_{-}}. \end{aligned} \tag{2.24}$$

After the substitution of Eq. (2.23) in Eq. (2.24) and isolating the real part it follows that

$$\begin{aligned} x &= -\frac{A^{+}}{\omega_{+} - \omega_{-}} \cos(\omega_{+} t + \varphi_{+}) + \frac{A^{-}}{\omega_{+} - \omega_{-}} \cos(\omega_{-} t + \varphi_{-}), \\ y &= -\frac{A^{+}}{\omega_{+} - \omega_{-}} \sin(\omega_{+} t + \varphi_{+}) + \frac{A^{-}}{\omega_{+} - \omega_{-}} \sin(\omega_{-} t + \varphi_{-}), \end{aligned} \tag{2.25}$$

where x and y are a combination of oscillations with the frequencies ω_{+} and ω_{-}. The factors

$$\frac{A^{\pm}}{\omega_{+} - \omega_{-}} = \rho_{\pm,0} \tag{2.26}$$

are the radii of the oscillations and Eq. (2.25) can be written as

$$\begin{aligned} x &= \rho_{+} \cos(\omega_{+} t + \varphi_{+}) + \rho_{-} \cos(\omega_{-} t + \varphi_{-}), \\ y &= \rho_{+} \sin(\omega_{+} t + \varphi_{+}) + \rho_{-} \sin(\omega_{-} t + \varphi_{-}), \end{aligned} \tag{2.27}$$

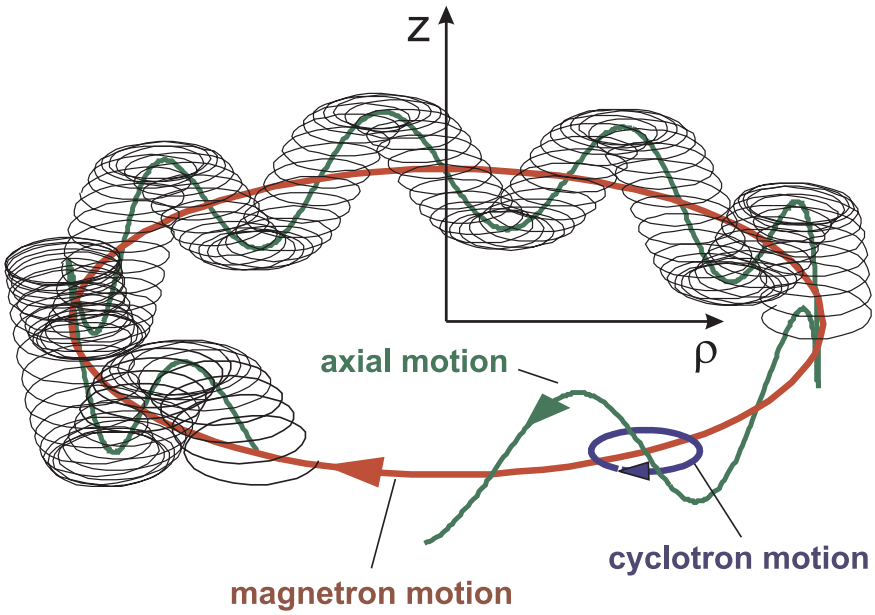

Figure 2.2: Schematical trajectory of the three eigenmotions in an ideal Penning trap. An axial motion with the angular frequency ω_z and a corresponding amplitude z_0, the cyclotron motion with ω_+ and ρ_+ and the magnetron motion ω_- and ρ_- are superimposed. The projection of the motion in the xy-plane is a cycloid.

where the initial phases φ_+ and φ_- are chosen to be zero for $t = 0$ and $\vec{\rho} = (x, y) = ((\rho_+ + \rho_-), 0)$. The sign of the frequencies $\omega_\pm$ depend on the sign of the charge, as discussed for Eq. (2.7). The resulting motion of the charged particle is the superposition of two radial motions: The cyclotron motion at the reduced cyclotron frequency ω_+ and the radius ρ_+ and the magnetron motion with the frequency ω_- and the radius ρ_- (Fig. 2.2).

2.3 Ion Motion with Excitations

If the ion motion is excited by electric fields $\vec{E} = (E_x, E_y, 0)$, the Eq. (2.16) changes to:

$$\ddot{x} = \dot{V}_x^\pm - \omega_\mp \dot{y} = -((\omega_+ + \omega_-)\,\dot{y} - \omega_+\omega_- x) + \frac{q}{m}E_x = -\omega_\pm V_y^\pm - \omega_\mp \dot{y} + \frac{q}{m}E_x, \quad (2.28)$$

$$\ddot{y} = \dot{V}_y^\pm + \omega_\mp \dot{x} = (\omega_+ + \omega_-)\,\dot{x} + \omega_+\omega_- y + \frac{q}{m}E_y = \omega_\pm V_x^\pm + \omega_\mp \dot{x} + \frac{q}{m}E_y$$

and hence Eq. (2.17) obtains additional terms:

$$\dot{\vec{V}}^\pm = \begin{pmatrix} 0 & -\omega_\pm \\ \omega_\pm & 0 \end{pmatrix} \vec{V}^\pm + \frac{q}{m}\vec{E}. \quad (2.29)$$

These additional terms are causing inhomogeneities in the equations of motion, where the analytical solution, if possible, can be a challenge.

2.3.1 Dipolar Excitation

A dipolar excitation is commonly applied as a linearly oscillating homogeneous electric field. The effect on the ion motion depends on the frequency and the initial phase of the field as compared to the ions eigenfrequency and phase. The equation of motion for a linear dipolar excitation in x direction, written in V-notation is

$$\dot{\vec{V}}^{\pm} = \begin{pmatrix} 0 & -\omega_{\pm} \\ \omega_{\pm} & 0 \end{pmatrix} \vec{V}^{\pm} + \frac{q}{m} \begin{pmatrix} \frac{U_\mathrm{d}}{\rho_0} \cos(\omega_\mathrm{d} t + \varphi_\mathrm{d}) \\ 0 \end{pmatrix}, \tag{2.30}$$

with U_d as amplitude of the excitation and φ_d as initial phase. These equations are solved by a Laplace transformation with the results [Koe91]:

$$\begin{aligned} V_x^{\pm} &= A^{\pm} \cos(\omega_{\pm} + \varphi_{\pm}) + \frac{U_\mathrm{d}}{\rho_0} \frac{(q/m)}{\omega_\mathrm{d}^2 - \omega_{\pm}^2} (\omega_\mathrm{d} \sin(\omega_\mathrm{d} t) - \omega_{\pm} \sin(\omega_{\pm} t)), \\ V_y^{\pm} &= -A^{\pm} \sin(\omega_{\pm} + \varphi_{\pm}) + \frac{U_\mathrm{d}}{\rho_0} \frac{(q/m)\omega_{\pm}}{\omega_\mathrm{d}^2 - \omega_{\pm}^2} (\cos(\omega_{\pm} t) - \cos(\omega_\mathrm{d} t)). \end{aligned} \tag{2.31}$$

For a resonant excitation i.e. $\omega_\mathrm{d} = \omega_+$, l'Hopital's rule is applied:

$$\begin{aligned} &\lim_{\omega_\mathrm{d} \to \omega_+} \left(\frac{\omega_\mathrm{d} \sin(\omega_\mathrm{d} t) - \omega_{\pm} \sin(\omega_{\pm} t)}{\omega_\mathrm{d}^2 - \omega_{\pm}^2} \right) \\ &= \left. \frac{\frac{d}{d\omega_\mathrm{d}} \left[\omega_\mathrm{d} \sin(\omega_\mathrm{d} t) - \omega_{\pm} \sin(\omega_{\pm} t) \right]}{\frac{d}{d\omega_\mathrm{d}} \left[\omega_\mathrm{d}^2 - \omega_{\pm}^2 \right]} \right|_{\omega = \omega_+} \\ &= \frac{\sin(\omega_+ t) + \omega_+ \cdot t \cdot \cos(\omega_+ t)}{2\omega_+} \end{aligned} \tag{2.32}$$

for $V_x^{\pm}$, and

$$\begin{aligned} &\lim_{\omega_\mathrm{d} \to \omega_+} \left(\frac{\omega_{\pm} \cos \omega_{\pm} t) - \cos(\omega_\mathrm{d} t)}{\omega_\mathrm{d}^2 - \omega_{\pm}^2} \right) \\ &= \left. \frac{\frac{d}{d\omega_\mathrm{d}} \left[\omega_{\pm} \cos \omega_{\pm} t) - \cos(\omega_\mathrm{d} t) \right]}{\frac{d}{d\omega_\mathrm{d}} \left[\omega_\mathrm{d}^2 - \omega_{\pm}^2 \right]} \right|_{\omega = \omega_+} \\ &= \frac{t \cdot \sin(\omega_+ t)}{2\omega_+} \end{aligned} \tag{2.33}$$

for $V_y^{\pm}$. The spacial coordinates x and y for the case $\omega_\mathrm{d} = \omega_+$ are obtained with Eq. (2.13)

$$x(t) = \frac{1}{\omega_+ - \omega_-}\left(A^+\sin(\omega_+ t + \varphi_+) + \frac{U_\mathrm{d}}{\rho_0}\frac{(q/m)}{2}t\sin(\omega_+ t)\right. \tag{2.34}$$
$$\left. -A^-\sin(\omega_- t + \varphi_-) - \frac{U_\mathrm{d}}{\rho_0}\frac{(q/m)\omega_-}{\omega_+^2 - \omega_-^2}(\cos(\omega_- t) - \cos(\omega_+ t))\right),$$
$$y(t) = \frac{1}{\omega_+ - \omega_-}\left(A^+\cos(\omega_+ t + \varphi_+) + \frac{U_\mathrm{d}}{\rho_0}\frac{(q/m)}{2\omega_+}t(\sin(\omega_+ t) + \omega_+ t\cos(\omega_+ t))\right.$$
$$\left. -A^-\cos(\omega_- t + \varphi_-) - \frac{U_\mathrm{d}}{\rho_0}\frac{(q/m)}{\omega_+^2 - \omega_-^2}(\omega_+\cos(\omega_+ t) - \omega_-\sin(\omega_- t))\right).$$

The calculation for $\omega_\mathrm{d} = \omega_-$ is analog. If a particle starts in the center of the trap, the coefficients A^+ and A^- are zero. With the assumption that $\omega_- \ll \omega_+$, the radius of one of both radial ion motions, which is not excited resonantly remains close to zero, since the excitation frequency is far away from the corresponding eigenfrequency. Thus the distance from the trap center $\sqrt{x(t)^2 + y(t)^2}$ is well approximated with $\rho_\pm$ for $\omega_\mathrm{d} = \omega_\pm$. The additional negligence of small terms leads to a simplified expressions for the radii

$$\rho_\pm(t) \approx \sqrt{x(t)^2 + y(t)^2} \approx \frac{U_\mathrm{d}}{\rho_0}\frac{(q/m)}{2(\omega_+ - \omega_-)}\sqrt{t^2 \mp \frac{2t\sin(\omega_\pm t)\cos(\omega_\pm t)}{\omega_\pm}}. \tag{2.35}$$

Combined with oscillations as shown in Fig. 2.3 (a), the radius is increasing with the

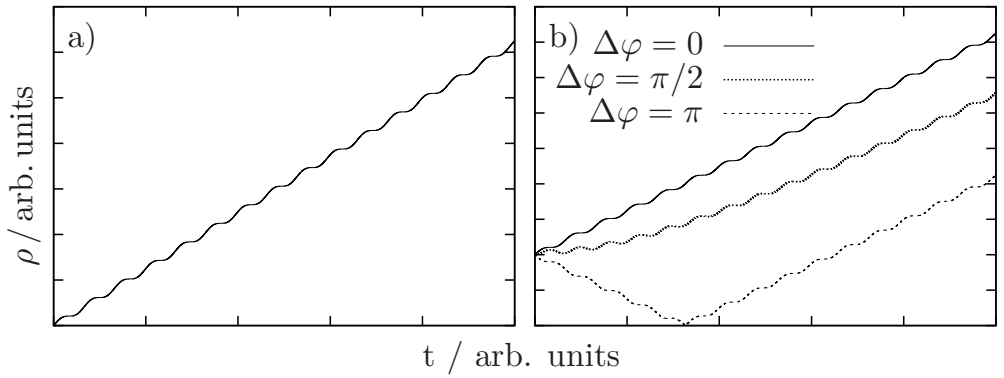

Figure 2.3: Radius of the motion $\rho_\pm$ as a function of time. Part (a): A particle which is placed in the trap center is excited by a dipolar excitation field with $\omega_\mathrm{d} = \omega_\pm$. Part (b): The initial radius of the particle is nonzero and a dipolar excitation is applied in phase $\Delta\varphi = 0$, with $\Delta\varphi = \pi/2$, and out of phase $\Delta\varphi = \pi$.

linear part $(q/m)(U_\mathrm{d}/\rho_0)/2(\omega_+ - \omega_-) \cdot t$. The oscillations are a result of the exciting force, which is not affecting the radius in the moments when the motional phase is perpendicular to the field. If the initial radius is not zero as shown in Fig. 2.3 (b), the initial phase difference $\Delta\varphi = \varphi_{exc} - \varphi_\pm$ with $\Delta\varphi = 0...\pi$ plays an important role. The radius $\rho_\pm$ is increased directly for $\Delta\varphi = 0$. For $0 < \Delta\varphi \leq \pi/2$ the radius is increased slowly in the beginning, and for $\pi/2 < \Delta\varphi \leq \pi$ the radius is first decreasing and afterwards increasing where for $\Delta\varphi = \pi$ the motion decreases to zero for a moment.

2.3.2 Circularly Polarized Dipolar Excitation

The circularly polarized dipolar excitation is a superposition of two perpendicular linearly polarized dipolar oscillating fields which are shifted by 90° in space (azimuthally) and time. The equation of motion obtains an additional term

$$\dot{\vec{V}}^\pm = \begin{pmatrix} 0 & -\omega_\pm \\ \omega_\pm & 0 \end{pmatrix} \vec{V}^\pm + \frac{q}{m} \begin{pmatrix} (U_\mathrm{d}/\rho_0)\cos(\omega_\mathrm{d} t + \varphi_\mathrm{d}) \\ (U_\mathrm{d}/\rho_0)\sin(\omega_\mathrm{d} t + \varphi_\mathrm{d}) \end{pmatrix}. \tag{2.36}$$

The field is moving in line with the motional phase of the particle, which results in double the radius as compared to the linear dipolar excitation scheme for the same amplitude and excitation time. Another effect is the vanishing of the oscillating term of Eq. (2.35) as shown in Fig. 2.4. Since the ion is accelerated continuously with the

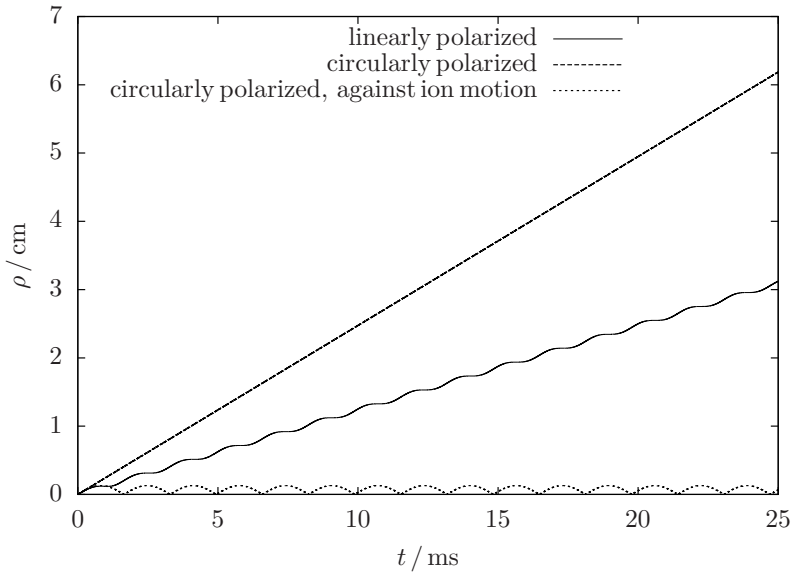

Figure 2.4: Simulated radial motion as a function of time for the linearly polarized, and the circularly polarized dipolar excitation scheme with an excitation amplitude of 500 mV. The motion for the circularly polarized dipolar excitation scheme is plotted for both rotational directions.

circularly polarized excitation, the radius is a straightly increasing. The final radius of an excited particle starting from the center is given by [SA93]

$$\rho_{\pm}(t) = \frac{U_{\mathrm{d}}}{\rho_0} \frac{(q/m)}{(\omega_+ - \omega_-)} \cdot t. \tag{2.37}$$

If the field is rotating against the ion motion of the ion, the radius is not increased and the ion is moving with small oscillations [SA93] (see Fig. 2.4). The superposition of both rotational directions for the circular dipolar field is the common used linearly polarized dipolar excitation. Both properties are then connected, an increased radius, and the small oscillations due to the contribution of the rotating field against the motional direction of the ion (see Eq. (2.35)).

2.3.3 Quadrupolar Excitation

The quadrupolar excitation is one of the most important techniques in penning traps [BG86], [BMSS90]. As commonly used, an oscillating quadrupolar potential Φ_{q} with the excitation amplitude U_{q} is applied

$$\Phi_{\mathrm{q}}(x, y) = \frac{2U_{\mathrm{q}}}{r_0^2} xy \cdot \cos(\omega_{\mathrm{q}} t + \varphi_{\mathrm{q}}) \tag{2.38}$$

which leads to the field vector

$$\vec{E} = \begin{pmatrix} y \cdot a_{\mathrm{q}} \cos(\omega_{\mathrm{q}} t + \varphi_{\mathrm{q}}) \\ x \cdot a_{\mathrm{q}} \cos(\omega_{\mathrm{q}} t + \varphi_{\mathrm{q}}) \end{pmatrix}, \tag{2.39}$$

with the parameter $a_{\mathrm{q}} = -2U_{\mathrm{q}}/r_0^2$ for an ideal quadrupolar field. The sign $(-)$ from $\vec{E} = -\vec{\nabla}\Phi_{\mathrm{q}}(x, y)$ is included in a_{q}. The initial phase of the quadrupolar excitation field φ_{q} as well as the initial phases of the two radial eigenmotions φ_+ and φ_- are set to zero for this approach. The equations of motion for $\vec{V}^+$ and $\vec{V}^+$ are

$$\dot{\vec{V}}^{\pm} = \begin{pmatrix} 0 & -\omega_{\pm} \\ \omega_{\pm} & 0 \end{pmatrix} \vec{V}^{\pm} + \begin{pmatrix} \frac{q}{m} y \cdot a_{\mathrm{q}} \cos(\omega_{\mathrm{q}} t) \\ \frac{q}{m} x \cdot a_{\mathrm{q}} \cos(\omega_{\mathrm{q}} t) \end{pmatrix}. \tag{2.40}$$

With the expression for x and y in Eq. (2.24) they can be rewritten in V components as follows

$$\begin{aligned} \dot{V}_x^{\pm} &= -\omega_{\pm} V_y^{\pm} + k V_x^{+} - k V_x^{-}, \\ \dot{V}_y^{\pm} &= \omega_{\pm} V_x^{\pm} - k V_y^{+} + k V_y^{-} \end{aligned} \tag{2.41}$$

where

$$k = k_0 \cdot \cos(\omega_{\mathrm{q}} t) \qquad k_0 = \frac{q}{m} \frac{a_{\mathrm{q}}}{\omega_+ - \omega_-}. \tag{2.42}$$

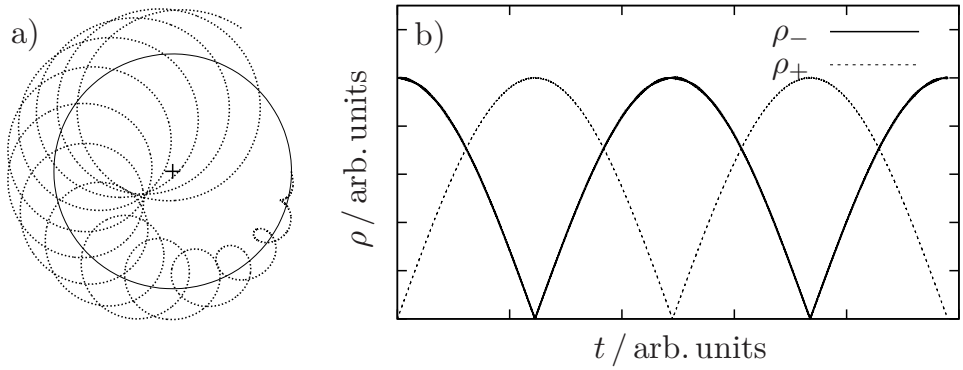

Figure 2.5: Conversion of the radial motions affected by a quadrupolar excitation with $\omega_\mathrm{d} = \omega_c$. In part (a) the beginning of a conversion from pure magnetron motion into cyclotron motion is illustrated schematically as a projection in the xy-plane. The ion has a positive charge ($\omega_\pm < 0$). In part (b) the radii ρ_+ and ρ_- in the periodic conversion are plotted as a function of time.

A solution of Eq. (2.41), which can be seen detailed in A, is given by

$$\begin{aligned} x(t) &= \rho_0 \left(\cos\left(\omega_+ t\right) \sin\left(\omega_\mathrm{B} t\right) + \cos\left(\omega_- t\right) \cos\left(\omega_\mathrm{B} t\right)\right), \\ y(t) &= \rho_0 \left(\sin\left(\omega_+ t\right) \sin\left(\omega_\mathrm{B} t\right) + \sin\left(\omega_- t\right) \cos\left(\omega_\mathrm{B} t\right)\right). \end{aligned} \tag{2.43}$$

In Eq. (2.43), a pure initial magnetron motion with the radius ρ_0 is converted into cyclotron motion and vice versa periodically with the so called beating frequency $\omega_\mathrm{B} = k_0/2$, as shown in Fig. 2.5 (b). The part (a) in Fig. 2.5 illustrates the beginning of the progress as a projection of the motion into the xy-plane.

2.3.4 Phase Dependency of Quadrupolar Excitation

The initial phases of the radial eigenmotions $\varphi_\pm$ and the quadrupolar field φ_q are crucial for the motion of the particles as discussed for dipolar excitation. With respect to the initial phases the solution for the ion motion is obtained as a complex expression [KBK+95]

$$\begin{aligned} \rho_+(t) &= \rho_{+,0} \cos\left(\omega_\mathrm{B} t\right) - \rho_{-,0} \sin\left(\omega_\mathrm{B} t\right) e^{\mathrm{i}\Delta\varphi}, \\ \rho_-(t) &= \rho_{-,0} \cos\left(\omega_\mathrm{B} t\right) + \rho_{+,0} \sin\left(\omega_\mathrm{B} t\right) e^{-\mathrm{i}\Delta\varphi}, \end{aligned} \tag{2.44}$$

with

$$k_0^{\pm} = k_0 e^{\pm \mathrm{i}\Delta\varphi} \quad , \quad \Delta\varphi = \varphi_\mathrm{q} - \varphi_+ - \varphi_- . \tag{2.45}$$

The radial kinetic ion energy $E_\rho(t)$ as a real expression, is proportional to the squares of the radii, whereas the magnetron motion is neglected [KBK+95]

$$E_\rho(t) \propto \omega_+^2 \rho_+^2 + \omega_-^2 \rho_-^2 \approx \omega_+^2 \rho_+^2 = \omega_+^2 \rho_\pm \rho_\pm^* . \tag{2.46}$$

For a pure initial magnetron motion, the radial energy is obtained as [RBS+07]:

$$E_\rho(t) \propto \rho_{+,0}^2 \cos^2(\omega_\mathrm{B} t) + \rho_{-,0}^2 \sin^2(\omega_\mathrm{B} t) + \rho_{+,0}\rho_{-,0} \sin(2\omega_\mathrm{B} t)\cos(\Delta\varphi). \tag{2.47}$$

Hence the phase dependency vanishes for initial conditions chosen so that one of the initial radii is zero. In the experiment this case is aimed for to keep phase related phenomena in a small range.

2.3.5 Non Resonant Quadrupolar Excitation

If the ions in the trap are not excited at the resonance frequency $\omega_\mathrm{q} \neq \omega_c$, the conversions between the eigenmotions are not complete [KBK+95]:

$$\rho_\pm(t) = \left[\rho_{\pm,0} \cos(\omega_\mathrm{B} t) \mp \frac{1}{2} \frac{\rho_{\pm,0}\left[\mathrm{i}(\omega_\mathrm{q} - \omega_c)\right] + \rho_{\mp,0} k_0^{\pm}}{\omega_\mathrm{B}} \right] \cdot \sin(\omega_\mathrm{B} t) e^{\frac{1}{2}\mathrm{i}(\omega_\mathrm{q} - \omega_c)t} \tag{2.48}$$

where ω_B is now given by

$$\omega_\mathrm{B} = \frac{1}{2}\sqrt{(\omega_\mathrm{q} - \omega_c) + k_0^2}. \tag{2.49}$$

A plot of a variable as a function of the excitation frequency ν_B is a resonance curve, where at this point the radial energy will be taken into account. In a motion initialized with a pure magnetron motion the radial energy, calculated as in Eq. (2.47) has the following proportionality:

$$E_\rho(\omega_\mathrm{B}) \propto \frac{\sin^2(\omega_\mathrm{B} T_\mathrm{exc})}{\omega_\mathrm{B}^2}, \tag{2.50}$$

with T_exc as the duration of excitation. In the discussion and the figures, the angular frequencies ω_q, ω_c, ω_+, and ω_- are written as $\nu_i = \omega_i/(2\pi)$. An overview of the quadrupolar resonance scheme is shown in Fig. 2.6. The unit $\Delta\nu \cdot T_\mathrm{exc}$ for the shapes is universal for every excitation duration since $\Delta\nu_H \propto 1/T_\mathrm{exc}$. In the overview, the resonance shapes are propagating waves, starting from a central point at $\Delta\nu = 0$ and $k_0 \cdot T_\mathrm{exc} = \pi/2$. In the lower part are 2-D cuts for $k_0 \cdot T_\mathrm{exc} = \pi/2$ (a), π (b) (minimum at the center for (b)), $k_0 \cdot T_\mathrm{exc} = 3\pi/2$ (c), $5\pi/2$ (d), $7\pi/2$ (e), and $9\pi/2$ (f). In part (a), E_ρ has a global maximum, centered at $\Delta\nu = 0$, with small secondary maxima. In this case the numerically determined full width at half maximum (FWHM) is $\Delta\nu_H = 0.8/T_\mathrm{exc}$ [KBK+95], which is the minimal possible value for FWHM, which is also known as Fourier limitation. With the increasing of $k_0 \cdot T_\mathrm{exc}$ the shapes of E_ρ are oscillating between a center peak domination and a domination of the secondary maxima (b). For every scan with $k_0 \cdot T_\mathrm{exc} = (2n+1) \cdot \pi/2$, $(n = 0, 1, 2, ...)$ the maximum of the radial energy is at the center point $\Delta\nu = 0$, where the FWHM and the secondary maxima are

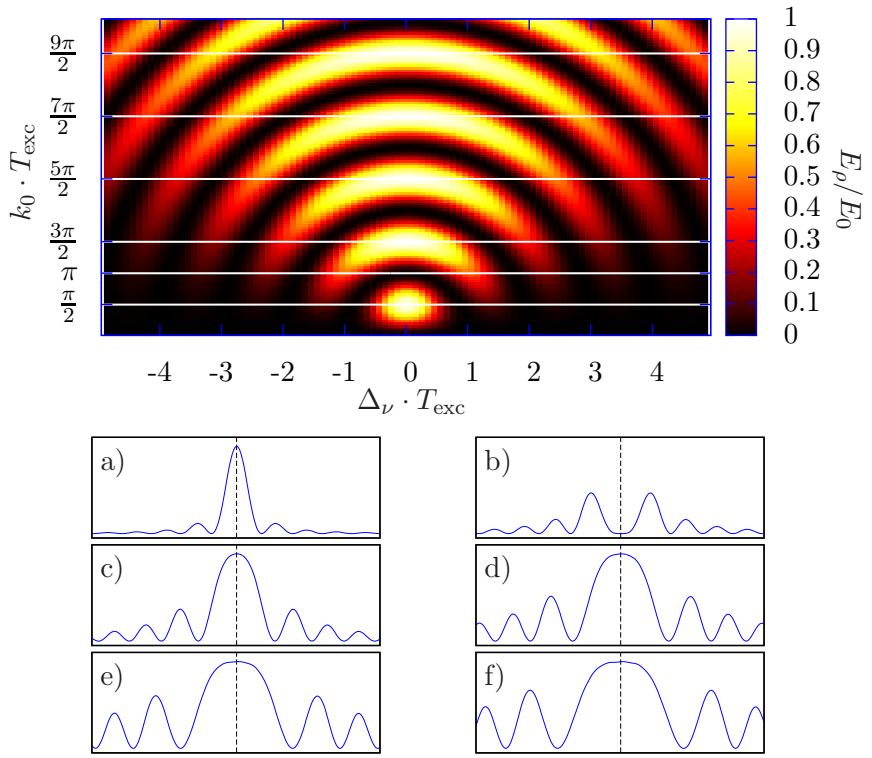

Figure 2.6: Upper Part: Simulated contour plot of the radial energy as a function of the detuning $\Delta\nu \cdot T_{\mathrm{exc}}$ of the frequency on the abscissa, and $k_0 \cdot T_{\mathrm{exc}}$ on the ordinate. The values on the color axis are normalized to the maximum of the radial energy E_0 which implies a pure cyclotron motion. The horizontal white lines are plotted to guide the eye to compare the xz-cuts in the images below. Lower Part: Cuts of the 3D-plot.

increased by n.

2.3.6 Circularly Polarized Quadrupolar excitation

The Circularly Polarized Quadrupolar excitation is a superposition of two quadrupolar oscillating fields shifted by 45° in space (azimuthally) and shifted by 90° in time. This leads to a rotation of the field in analogy to a circularly polarized dipolar excitation. The potential of the excitation is given by:

$$\Phi_{qr}(x,y) = \frac{U_{\mathrm{q}}}{r_0^2}(2xy \cdot \cos(\omega_{\mathrm{q}} t + \varphi_{\mathrm{q}}) \mp (x^2 - y^2)\sin(\omega_{\mathrm{q}} t + \varphi_{\mathrm{q}})) \tag{2.51}$$

where the second part can be subtracted or added from the first part which means that the field is rotating forward or backward. The field vector for a forward rotation is

$$\vec{E} = \begin{pmatrix} y \cdot a_\mathrm{q} \cos(\omega_\mathrm{q} t + \varphi_\mathrm{q}) - x \cdot \sin(\omega_\mathrm{q} t + \varphi_\mathrm{q}) \\ x \cdot a_\mathrm{q} \cos(\omega_\mathrm{q} t + \varphi_\mathrm{q}) + y \cdot \sin(\omega_\mathrm{q} t + \varphi_\mathrm{q}) \end{pmatrix}. \tag{2.52}$$

This leads to additional components for Eq. (2.41) in V notation

$$\begin{aligned} \dot{V}_x^\pm &= -\omega_\pm V_y^\pm + k_1 V_x^+ - k_1 V_x^- + k_2 V_y^+ - k_2 V_y^-, \\ \dot{V}_y^\pm &= \omega_\pm V_x^\pm - k_1 V_y^+ + k_1 V_y^- + k_2 V_x^+ - k_2 V_x^-, \end{aligned} \tag{2.53}$$

$$k_1 = k_0 \cdot \cos(\omega_\mathrm{q} t) \quad k_2 = k_0 \cdot \sin(\omega_\mathrm{q} t) \quad k_0 = \frac{q}{m} \frac{a_\mathrm{q}}{\omega_+ - \omega_-}. \tag{2.54}$$

After using the ansatz from Eq. (A.1) for the additional terms with the factor k_2, and following the steps from Eq. (A.2) to Eq. (A.4), the additional part $P_{x,y}^\pm$ for the x and y component is obtained as

$$P_{x,y}^\pm = \frac{k_0}{2\mathrm{i}} \left(\pm A_{y,x}^\pm \left(e^{\mathrm{i}\omega_\mathrm{q} t} - e^{-\mathrm{i}\omega_\mathrm{q} t} \right) - A_{y,x}^\mp \left(e^{\pm \mathrm{i}(\omega_\mathrm{q} - \omega_c)} - e^{\mp \mathrm{i}(\omega_\mathrm{q} + \omega_c)} \right) \right). \tag{2.55}$$

With the simplification for a motion close to a circle in Eq. (A.6), the amplitudes $A_{x,y}^\pm$ can be written as $\pm \mathrm{i} A_{y,x}^\pm$ thus the imaginary unit from $\frac{k_0}{2\mathrm{i}}$ is eliminated. The addition of the new parts $P_{x,y}^\pm$ to Eq. (A.4) eliminates the high frequency term $e^{\mp \mathrm{i}(\omega_\mathrm{q} + \omega_c)}$ and a factor of 2 for all terms is obtained. The Eq. (A.4) is rewritten as:

$$\begin{aligned} \dot{A}_x^\pm &= \pm k_0 \left(A_x^\pm e^{\mp \mathrm{i}\omega_\mathrm{q} t} - A_x^\mp e^{\pm \mathrm{i}(\omega_\mathrm{q} - \omega_c) t} \right), \\ \dot{A}_y^\pm &= \mp k_0 \left(A_y^\pm e^{\mp \mathrm{i}\omega_\mathrm{q} t} - A_y^\mp e^{\pm \mathrm{i}(\omega_\mathrm{q} - \omega_c) t} \right). \end{aligned} \tag{2.56}$$

The only remaining term for high frequency oscillations $e^{\mp \mathrm{i}\omega_\mathrm{q} t}$ is neglected as discussed for the linear quadrupolar excitation scheme in the appendix. Equation (A.7) is rewritten as:

$$\begin{aligned} \dot{A}^+ &= -k_0 A^- \cdot e^{\mathrm{i}(\omega_\mathrm{q} - \omega_c) t}, \\ \dot{A}^- &= +k_0 A^+ \cdot e^{-\mathrm{i}(\omega_\mathrm{q} - \omega_c) t}, \end{aligned} \tag{2.57}$$

which leads to the same solution as for the previous introduced quadrupolar excitation scheme, with double the beating frequency ω_B, which is illustrated in Fig. 2.7. Note that, if the rotational direction of the exciting circular quadrupolar field is opposite to the motion of the ion, the Eq. (2.56) changes to

$$\begin{aligned} \dot{A}_x^\pm &= \pm k_0 \left(A_x^\pm e^{\pm \mathrm{i}\omega_\mathrm{q} t} - A_x^\mp e^{\mp \mathrm{i}(\omega_\mathrm{q} + \omega_c) t} \right), \\ \dot{A}_y^\pm &= \mp k_0 \left(A_y^\pm e^{\pm \mathrm{i}\omega_\mathrm{q} t} - A_y^\mp e^{\mp \mathrm{i}(\omega_\mathrm{q} + \omega_c) t} \right). \end{aligned} \tag{2.58}$$

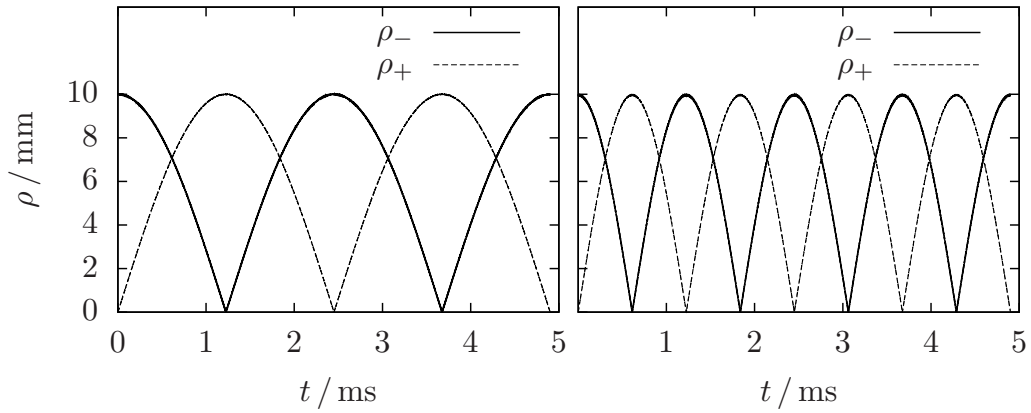

Figure 2.7: Left: Conversions of the eigenmotions (simulated) in a linearly polarized quadrupolar excitation scheme. Right: Conversions of the eigenmotions in a circularly polarized quadrupolar excitation scheme. In both simulations, $^{133}Cs^+$ ions are excited with the same amplitude $U_q = 0.78V$.

where the low frequency term is missed, which results in a non-appearance of conversions. Just small high-frequency oscillations are performed, similar to a circularly polarized dipolar excitation which is rotating against the ion motion.

2.4 Ion Motion with Damping

If the trap is filled with a buffer gas, i.e. helium, the ions are loosing energy by collisions with the neutral background. The damping of the ion motion can be approximated with a velocity-dependent force which is given by:

$$\frac{\vec{F}_d}{m} = -\delta \begin{pmatrix} \dot{x} \\ \dot{y} \end{pmatrix} = -\gamma \begin{pmatrix} -\omega_+ V_x^+ + \omega_- V_x^- \\ -\omega_+ V_y^+ + \omega_- V_y^- \end{pmatrix} \tag{2.59}$$

with:

$$\gamma = \frac{\delta}{\omega_+ - \omega_-}. \tag{2.60}$$

The coefficient δ is a constant in the following discussion. Other models of damping will be discussed in 3.3. The decoupled motion in z-direction is a damped harmonic oscillator. For the radial components the new equation of motion is:

$$\begin{aligned} \dot{V_x}^{\pm} &= -\omega_\pm V_y^\pm + \gamma(\omega_+ V_x^+ - \omega_- V_x^-), \\ \dot{V_y}^{\pm} &= \omega_\pm V_x^\pm + \gamma(\omega_+ V_y^+ - \omega_- V_y^-). \end{aligned} \tag{2.61}$$

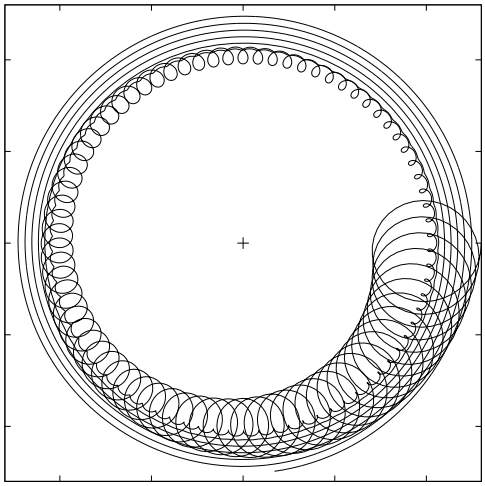

Figure 2.8: Schematic view of the damped motion of a particle in the xy-plane with the decreasing cyclotron motion and the increasing magnetron motion.

The solution of the radial equation for the amplitudes $A^{\pm}$ is:

$$A^{\pm}(t) = A_0^{\pm} e^{\mp \epsilon_{\pm} t} \tag{2.62}$$

with the coefficient:

$$\epsilon_{\pm} = \delta \frac{\omega_{\pm}}{\omega_+ - \omega_-}. \tag{2.63}$$

The energy loss of the two eigenmotions leads to a fast decreasing of the high-frequency cyclotron motion and a slow widening of the magnetron motion [SBB+91]. Figure 2.8 illustrates the damped ion motion in a Penning trap without excitation.

2.4.1 Buffer Gas and Quadrupolar excitation

For the purpose of ion centering, a cooling process without excitation is not adequate since the magnetron motion is widening which leads to a loss of all ions. If a quadrupolar excitation is added, the eigenmotions are converted into each other as discussed in 2.3.3. Since the cyclotron radius in a buffer gas is decreasing much faster than the magnetron radius grows $\omega_- \ll \omega_+$, it is possible to move the ions to the axes. For a quadrupolar excitation in a buffer gas environment the sum of the forces in V-notation is:

$$\begin{aligned} \dot{V_x}^{\pm} &= -\omega_{\pm} V_y^{\pm} + k(V_x^+ - V_x^-) + \gamma(\omega_+ V_x^+ - \omega_- V_x^-), \\ \dot{V_y}^{\pm} &= \omega_{\pm} V_x^{\pm} - k(V_y^+ - V_y^-) + \gamma(\omega_+ V_y^+ - \omega_- V_y^-). \end{aligned} \tag{2.64}$$

The solution of Eq. (2.64) can be found by a Laplace transformation [KBK+95]. In the resonance case $\omega_q - \omega_c = 0$ and with $\Delta\phi = 0$ it is obtained as

$$\rho_{\pm}(t) = e^{-\frac{\delta}{2}t}\left[\rho_{\pm,0}\cosh(\omega_B t) \mp \frac{1}{2}\frac{\rho_{\pm,0}\gamma\omega_c + \rho_{\mp,0}k_0}{\omega_B}\cdot\sinh(\omega_B t)\right] \tag{2.65}$$

with a new expression for the beating frequency ω_B

$$\omega_B = \sqrt{\gamma^2\omega_c^2 - k_0^2}. \tag{2.66}$$

This solution includes oscillating as well as exponential motion schemes of the radii depending on whether ω_B is complex or real. One can distinguish between four different cases for the parameter set as shown with a simulation in Fig.2.9. For a fixed excitation duration and amplitude, different damping constants γ are chosen to study the motion schemes of a single ion in the trap. In part (a) the parameters are set to $\gamma > k/\sqrt{2}\cdot\omega_z$

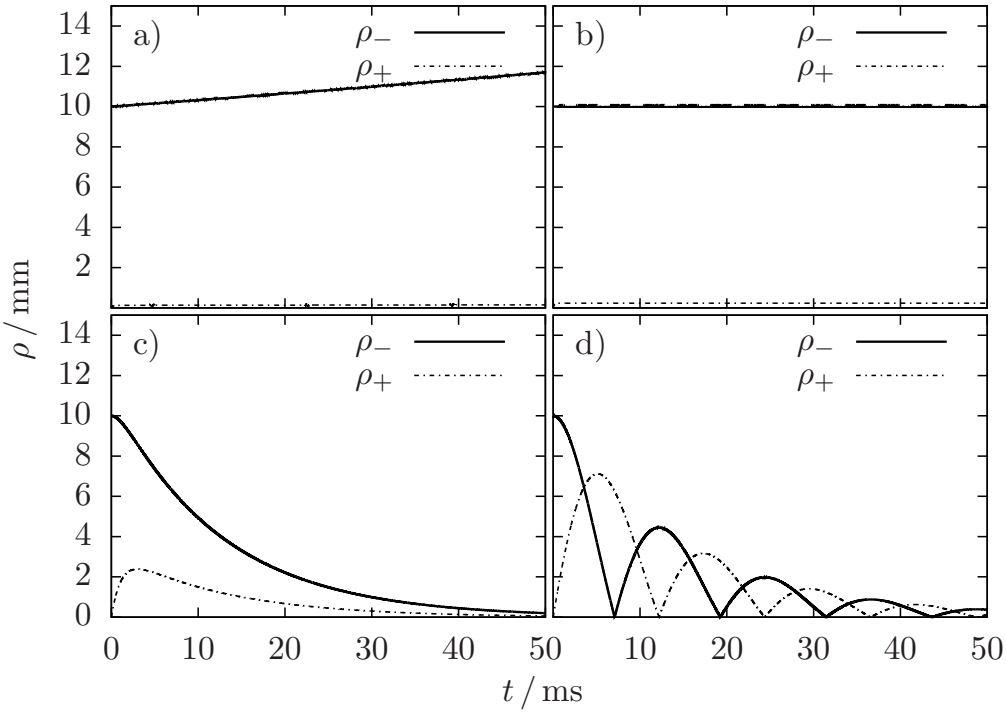

Figure 2.9: Radii of quadrupolar excited ions as a function of the time with different pressures.

where the widening of the magnetron motion is faster than the conversion into cyclotron motion. In part (b) the magnetron radius stays in an equilibrium with $\gamma = k/\sqrt{2}\cdot\omega_z$. If $k_0/\omega_c < \gamma < k/\sqrt{2}\cdot\omega_z$ the magnetron motion is decreasing exponentially as in part (c) and the condition $\gamma < k_0/\omega_c$ leads to an oscillating behavior where several conversions

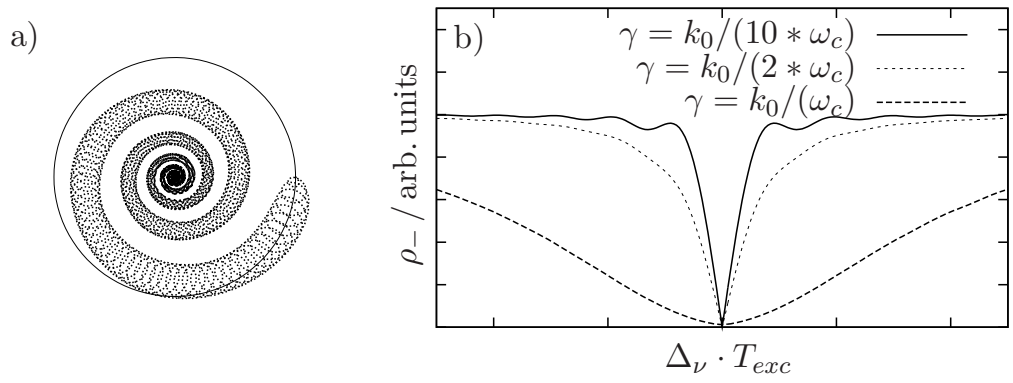

Figure 2.10: Ion motion with damping and quadrupolar excitation. (a) Trajectory of an ion in the *xy*-plane. (b) Resonance curve: magnetron radius after a quadrupolar excitation as a function of the normalized frequency detuning. The resonance curve is widening in presence of a damping force as illustrated for three different damping constants (simulation).

are possible before the ion is centered as in part (d). With a closer view, one can see small oscillations on the plotted lines, they belong to the high frequency terms of the motion which are not neglected in a numerical simulation. The radial motion for a centered ion is illustrated in Fig. 2.10 (a). A resonant excited ion in a quadrupolar excitation scheme is centered in a buffer-gas environment. The conditions chosen for this movement are similar to the parameters in Fig. 2.9 (c). The buffer gas cooling technique is mass selective. If the excitation frequency is detuned from the center frequency the ions are not centered since the conversions are incomplete. An increasing of the pressure leads to a better centering even for non resonant excited ions. This means that a higher pressure causes broader resonances curves which is shown with the magnetron radius in Fig. 2.10 (b), which is the more important motional parameter for the buffer-gas cooling technique.
Note that resonance curves which are affected by a damping force are not invariant for the scaling with $\Delta\nu \cdot T_{\mathrm{exc}}$. For a comparison of the resonances with those of the vacuum case, the excitation duration has to be known. Furthermore the conversion scheme is not invariant for $k_0 \cdot T_{\mathrm{exc}}$ as for the vacuum case. For a possible normalized scaling one could use $U_{\mathrm{q}} \,/\, U_{\mathrm{B}}$ with $U_{\mathrm{q}} \,/\, U_{\mathrm{B}} = 1$ for the amplitude which is required to perform a complete conversion (see measurements 5).

2.4.2 Resolving Power above the Fourier Limit by Radial Selection of Ions

In the experiment, the ions with a radius larger than the bores in the end caps $\rho_- > \rho_\mathrm{D}$ are selected from the ions with $\rho_- < \rho_\mathrm{D}$, and thus it is possible to obtain smaller FWHM ($\Delta\nu_\mathrm{H}$) values than the Fourier limit predicts, which leads to higher resolving powers $R_p = \nu_c/\Delta\nu$. The magnetron radius of a quadrupolar resonance curve (vacuum) with $k_0 \cdot T_\mathrm{exc} = \pi/2$ is illustrated in Fig. 2.11 with a black line. If all ions with a radius

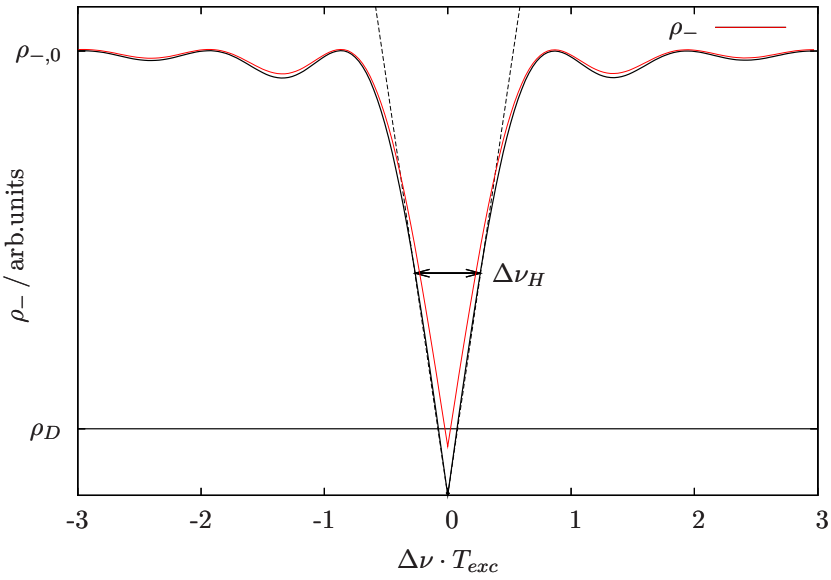

Figure 2.11: Black solid line: Magnetron radius for $k_0 \cdot T_\mathrm{exc} = \pi/2$ as a function of $\Delta\nu$. Red line: Magnetron radius for a detuned amplitude (schematic). Black dashed line: Approximation of the shape (see text).

$\rho_- > \rho_\mathrm{D}$ are not detected, the width of the resonance changes. Near the minimum of the radius, the resonance curve is well approximated with a straight (dashed black lines in Fig. 2.11), and thus the new width $\Delta\nu_\mathrm{D}$ at ρ_D is given by

$$\Delta\nu_\mathrm{D} = \frac{\Delta\nu_H \cdot \rho_\mathrm{D}}{(\rho_{-,0}/2)}, \tag{2.67}$$

where $\Delta\nu_\mathrm{D} < \Delta\nu_H$ for $\rho_{-,0} > 2\rho_\mathrm{D}$. At ISOLTRAP, the radial selection is realized with a small diaphragm in the axial center of the Preparation Penning Trap which separates resonantly excited from non resonantly excited ions (see 4.3). For a fixed ρ_D, the resolving power is increased by optimizing the initial magnetron radius [Bec97]. Note that the width $\Delta\nu_\mathrm{H}$ of a resonance curve for the magnetron radius is not $0.8/T_\mathrm{exc}$ as for the radial energy, but $0.53/T_\mathrm{exc}$, which has been determined in test simulations. If the amplitude is detuned, so that the ions are not completely centered for $\nu_\mathrm{exc} = \nu_c$ as illustrated with the red line in Fig. 2.11, the resolving power is further increased. In

this case just a dip of the resonance shape reaches the center region and the effective ρ_{D} value decreases to zero with further detuning of the excitation amplitude, until no ions are detected anymore. Theoretically the resolving power would increase to infinity, but in the experiment this is not the case since the radial selection is not ideal.

2.5 Octupolar Excitation

In an oscillating octupolar field the ions are excited with double the number of nodes and anti-nodes than in a quadrupolar field. The potential of a radial oscillating octupolar excitation is given by

$$\Phi_{\mathrm{oct}}(x,y) = \frac{U_{\mathrm{oct}}}{r_0^4}(x^4 - 6x^2y^2 + y^4)\cos(\omega_{\mathrm{oct}}t + \varphi_{\mathrm{oct}}). \tag{2.68}$$

Thus, the components of the field are [RBS+07]

$$\begin{aligned} E_x &= (x^3 - 3xy^2)\cdot a_{\mathrm{oct}}\cos(\omega_{\mathrm{oct}}t + \varphi_{\mathrm{oct}}), \\ E_y &= (y^3 - 3x^2y)\cdot a_{\mathrm{oct}}\cos(\omega_{\mathrm{oct}}t + \varphi_{\mathrm{oct}}) \end{aligned} \tag{2.69}$$

with

$$a_{\mathrm{oct}} = \frac{4U_{\mathrm{oct}}}{r_0^4}. \tag{2.70}$$

In V-notation the equations of motion are obtained as

$$\begin{aligned} \dot{V}_x^{\pm} &= -\omega \pm V_y^{\pm} + k\frac{(V_x^+ - V_x^-)^2\left[(V_x^+ - V_x^-)^2 - 3(V_y^+ - V_y^-)^2\right]}{(\omega_+ - \omega_-)^3}, \\ \dot{V}_x^{\pm} &= \omega \pm V_x^{\pm} + k\frac{(V_y^+ - V_y^-)^2\left[(V_x^y - V_y^-)^2 - 3(V_x^+ - V_x^-)^2\right]}{(\omega_+ - \omega_-)^3} \end{aligned} \tag{2.71}$$

where

$$k = k_0\cdot\cos(\omega_{\mathrm{q}}t) \qquad k_0 = \frac{q}{m}\frac{a_{\mathrm{oct}}}{\omega_+ - \omega_-}.$$

The octupolar excitation scheme is a young research topic in experimental Penning trap physics [BAB+08],[RBS+07],[EBC+07],[BZH+07] and it is as well a research topic in theoretical physics, since an analytical solution of Eq. (2.71) has not yet been obtained. The excitation couples the two radial eigenmotions in analogy to the quadrupolar excitation, but the terms are more complicated. Since the azimuthal symmetry of the octupolar field is doubled as compared with a quadrupolar field, the frequency for the resonant coupling of the radial eigenmotions is $2\cdot\omega_c$ [RBS+07]. In this case complete conversions are performed similar to a quadrupolar excitation as shown in Fig. 2.12 (a). The conversions of the radii differ from the harmonic shape in a quadrupolar excitation scheme with a shape close to a rectangular function. With regard to the excitation amplitude and the initial magnetron radius, the beating frequency ω_{B} is a nonlinear function in both ρ_0 and U_{oct} [RBS+07],[BAB+08]. To remain the same beating frequency, the product $\rho_0\cdot U_{\mathrm{oct}}$ has to be maintained as shown in Fig. 2.12 (b), where

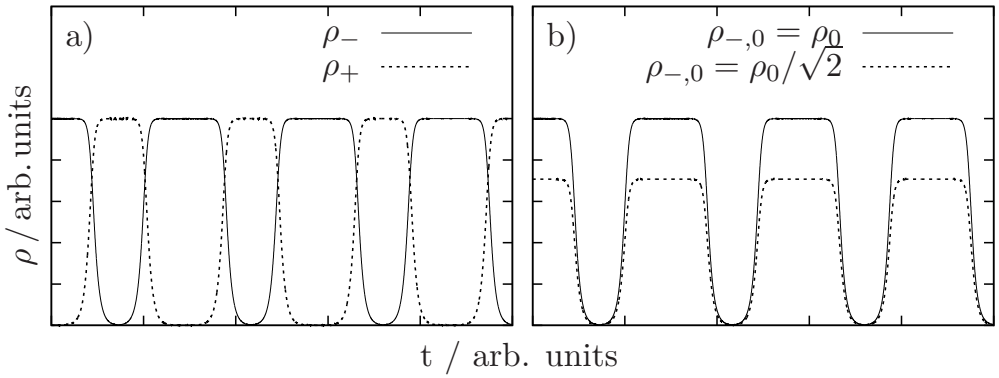

Figure 2.12: Magnetron and cyclotron radius as a function of time. (a) Periodically conversion of magnetron and cyclotron motion in an octupolar excitation scheme. (b) Magnetron radii of two equal ions as a function of time. The ion with the larger radius $\rho_{-,0} = \rho_0$ is excited with the amplitude U_0 and the other ion ($\rho_{-,0} = \rho_0/\sqrt{2}$) with the amplitude $2 * U_0$. Both have the same beating frequency.

$\rho_0 = \sqrt{\rho_{-,0}^2 + \rho_{+,0}^2}$ [RBS+07]. Since ν_B is not linear in U_oct, a normalization for the excitation amplitude $k_0 \cdot T_\mathrm{exc}$ as for a quadrupolar excitation scheme is not possible, similar to the damped quadrupolar excitation scheme.

2.5.1 Phase Dependency of an Octupolar Excitation

The phase dependency of the octupolar excitation scheme is much more complicated than the phase dependency of a quadrupolar excitation scheme [RBS+07]. Several simulations of the ion motion for the tree initial phases $\varphi_{+,0}$, $\varphi_{-,0}$, and $\varphi_{oct,0}$ have been performed to obtain an overview, where $\varphi_{oct,0}$ is the initial phase of the octupolar field. Four examples are chosen for illustration (Fig. 2.13). In the upper part of Fig. 2.13 the particle is initialized so that both radii are nonzero with $\rho_{-,0}/\rho_{+,0} = 100$ where in part (a) the phase $\varphi_{-,0}$ is scanned and in part (b) φ_+, both from zero to 2π with $\varphi_{\mathrm{oct},0} = 0$. The structures in both scans is completely different and thus there are no symmetries expected for the combination of φ_- and φ_+. In part (c) the conditions are the same as in part (b) but the phase of the external field $\varphi_{oct,0}$ is set from 0° to 45°. That results also in a completely different shape of the scan for φ_+. In part (d) the particle is initialized with a pure magnetron motion and φ_- is scanned for $\varphi_{\mathrm{oct},0} = 0$. This is illustrating that the phase dependency is not vanishing for $\rho_{\pm,0} = 0$ like in a quadrupolar excitation scheme. In other simulated examples (not plotted here), it is confirmed that even if $\rho_{\pm,0} = 0$ the complete phase scan of $\varphi_{-,0}$ changes with $\varphi_{oct,0}$. This means that a three dimensional field of phases has to be taken into account for the excitation. Note that as Fig. 2.13 shows, the conversion is not period. Thus no beating

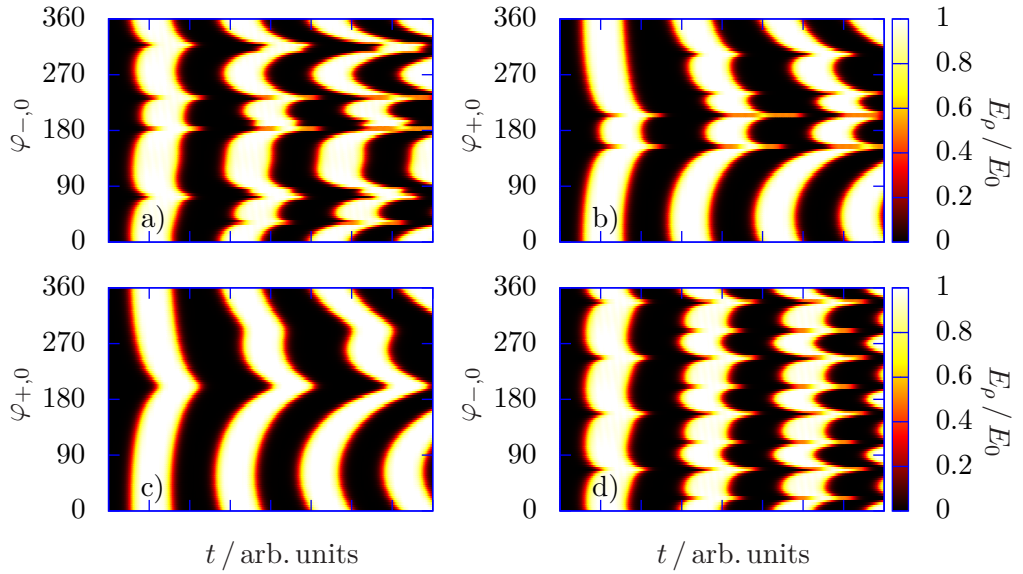

Figure 2.13: Radial normalized energy E_ρ/E_0 as a function of time and the initial phases. (a), (b), and (c): $\rho_{+,0} \neq 0$, $\rho_{-,0} \neq 0$, $\rho_{-,0}/\rho_{+,0} = 100$. (d): $\rho_{+,0} = 0$, $\rho_{-,0} \neq 0$.

frequency in the proper sense can be assigned.

2.5.2 Octupolar Resonance Curves

In the following the particular case of a pure initial magnetron radius is discussed. The shapes of the resonance curves differ from those of a quadrupolar excitation scheme, since the motion is much more sensitive with respect to U_{oct} and the initial phases. The additional dependency of ν_{B} on the initial radius is a very important difference to the quadrupolar excitation scheme. Figure 2.14 shows simulations of octupolar resonance shapes for different amplitudes and four initial phases (φ_-). The resonances seem to be a compound of a phase independent part and additional phase dependent secondary maxima which are moving through the resonance curve when the phase is changed. For several phases, the secondary maxima in the resonances vanish as in part (a) of the figure. Generally the resonances depend strongly on the excitation amplitude and include a large spectrum of possible shapes. For well chosen conditions it is possible to reach a resolving power much higher than the Fourier limit with 1/100 of the resonance width as compared to a quadrupolar excitation scheme for the same T_{exc} [RBS+07]. Double and multi peak structures of the resonance are also part of the spectrum. Note that in all four 3-D plots of Fig. 2.14, the first conversion seems to be free of the phase related secondary maxima. This is not the case for all initial phases

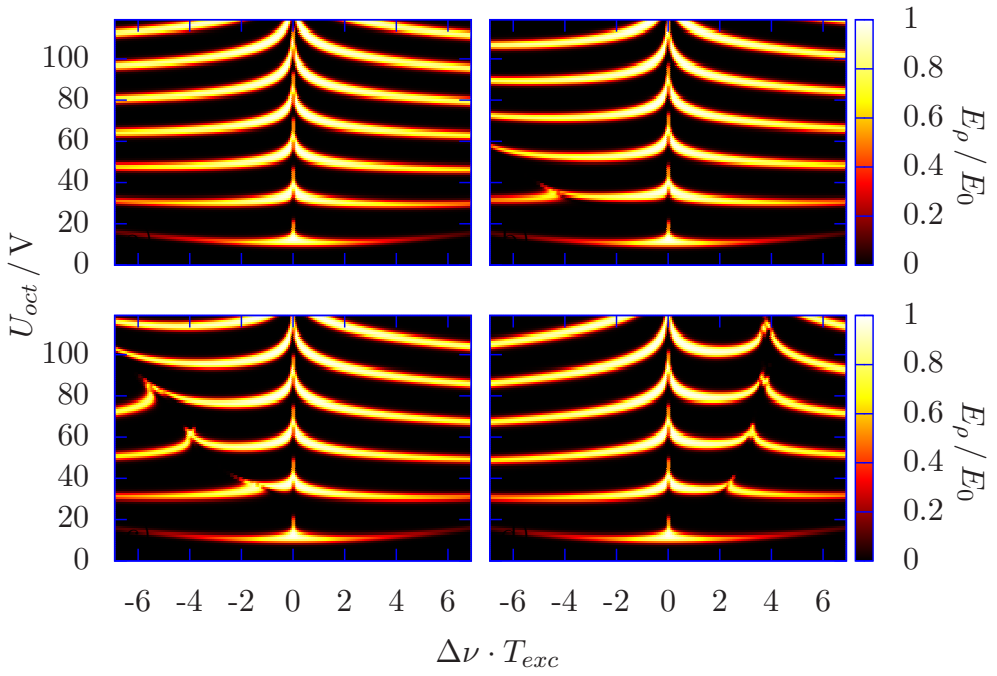

Figure 2.14: Radial energy (simulation) which is normalized to the maximal energy E_ρ/E_0 as a function of the frequency detuning and the amplitude. (a): $\varphi_{-,0} = 0°$, (b): $\varphi_{-,0} = 18°$, (c): $\varphi_{-,0} = 20°$, (d): $\varphi_{-,0} = 23°$. The resonances are simulated with an initial pure magnetron radius of 0.01m and an excitation time of $T_{\mathrm{exc}} = 1\mathrm{ms}$.

[BAB+08].
Some selected 2-D cuts of Fig. 2.14 are plotted in Fig. 2.15. In part (a) a narrow resonance without asymmetric secondary maxima is shown, which would be the optimal case for high resolution measurements. For other amplitudes, asymmetries and double peak structures are observed as in part (b). Two examples for phase related secondary maxima are given in part (c) and (d).

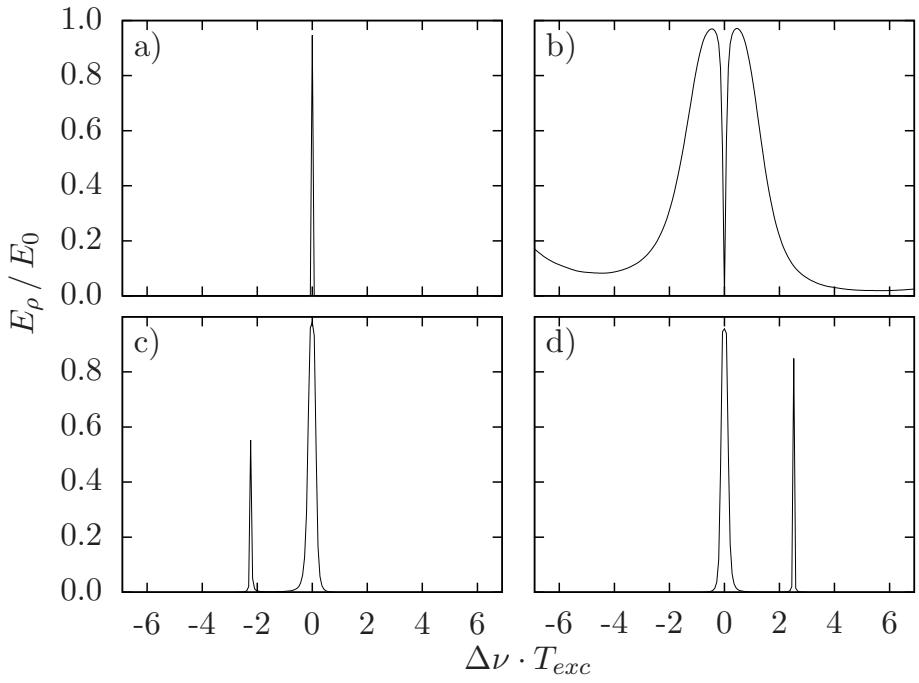

Figure 2.15: Radial energy which is normalized to the maximal energy E_ρ/E_0 as a function of the frequency detuning from 2-D cuts of Fig.2.14. (a): $\varphi_{-,0} = 0°$; $U_{\mathrm{oct}} = 20\,\mathrm{V}$, (b): $\varphi_{-,0} = 0°$; $U_{\mathrm{oct}} = 33\,\mathrm{V}$, (c): $\varphi_{-,0} = 20°$; $U_{\mathrm{oct}} = 41\,\mathrm{V}$, (d): $\varphi_{-,0} = 23°$; $U_{\mathrm{oct}} = 41\,\mathrm{V}$.

The resonances are not invariant if they are plotted with the unit $\Delta\nu \cdot T_{\mathrm{exc}}$ since $\Delta\nu_H \propto 1/T_{\mathrm{exc}}$ is not given. This has been tested in a simulation for three different excitation times as shown in Fig. 2.16. The three resonance curves are calculated with an amplitude chosen such that the first conversion is completed with $\rho_-(T_{\mathrm{exc}}) = 0$. With a longer excitation time the resonances get more narrow even if they are shown with a normalized scale. Nevertheless this scaling is applicable for a comparison with the quadrupolar excitation if the information about T_{exc} is added.

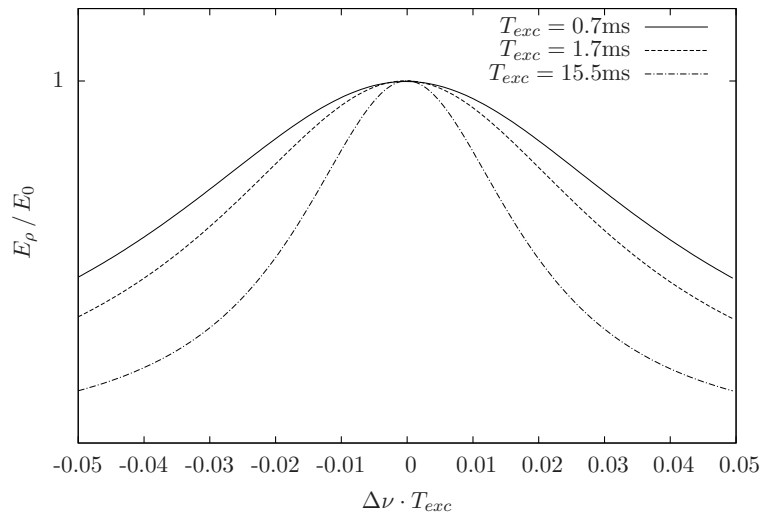

Figure 2.16: Radial energy which is normalized to the maximal energy as a function of the normalized frequency detuning. Three different excitation durations are applied.

3 Simulations

In the following, the cooling process with quadrupolar and octupolar excitation will be investigated in simulations. In addition, two different models for damping forces will be introduced and applied for realistic simulations. All simulations for this thesis are performed with a code written in C++ using a fifth order Gear method as integrator. To simplify the problem, all constant electrical fields in the trap and the excitation fields are taken from the analytical equations instead of simulating potentials from the electrode configurations.
For the simulation of cooling processes, the interaction forces between the ions are neglected. Frequency shifts due to ion ion interactions play an important role for high precision measurements, even with only a few ions in the trap. For 20 ions in the trap as for the most performed measurements, the shifted frequencies ν_{SHIFT} lead to a total deviation of $\nu_c - \nu_{\mathrm{SHIFT}} \approx 10^{-7} \cdot \nu_c$ from the cyclotron frequency [KBB+03], which has been determined with $^{36}Ar^+$ ions [KBB+03]. For accuracies of Preparation Penning Traps with $R_p \approx 10^4 - 10^5$, such effects are small as compared with the resonance width and can be neglected.
The quadrupolar excitation scheme is abbreviated with QES and the octupolar excitation scheme is abbreviated with OES.

3.1 Fifth order Gear Method

The Gear method is an integrator for differential equations which has been invented by C. W. Gear in 1971 [Gea71]. It is one of many predictor-corrector methods, which are frequently used for simulations. A predictor-corrector method includes a rough estimate for the coordinates in the next time step, followed by a correction step, which reduces the error. For the simulations, the fifth order has been chosen since the uncertainties for the third and fourth order have been too large, where too small time steps are necessary. In the Gear algorithm, the procedure for each iteration is performed in three steps. In the first step, the prediction of preliminary new coordinates is performed in five orders

$$
\begin{aligned}
\vec{r}^{\,p}_{n+1} &= \vec{r}_n + \vec{v}_n \cdot \Delta t + \vec{a}_n \cdot \Delta t 2F + \vec{d3}_n \cdot \Delta t 3F + \vec{d4}_n \cdot \Delta t 4F + \vec{d5}_n \cdot \Delta t 5F, \qquad (3.1)\\
\vec{v}^{\,p}_{n+1} &= \vec{v}_n + \vec{a}_n \cdot \Delta t + \vec{d3}_n \cdot \Delta t 2F + \vec{d4}_n \cdot \Delta t 3F + \vec{d5}_n \cdot \Delta t 4F,\\
\vec{a}^{\,p}_{n+1} &= \vec{a}_n + \vec{d3}_n \cdot \Delta t + \vec{d4}_n \cdot \Delta t 2F + \vec{d5}_n \cdot \Delta t 3F,\\
\vec{d3}^{\,p}_{n+1} &= \vec{d3}_n + \vec{d4}_n \cdot \Delta t + \vec{d5}_n \cdot \Delta t 2F,\\
\vec{d4}^{\,p}_{n+1} &= \vec{d4}_n + \vec{d5}_n \cdot \Delta t
\end{aligned}
$$

for the position $\vec{r}^{\,p}_{n+1}$, velocity $\vec{v}^{\,p}_{n+1}$, acceleration $\vec{a}^{\,p}_{n+1}$, and the third and fourth derivatives of $\vec{r}(t)$, $\vec{d3}^{\,p}_{n+1}$ and $\vec{d4}^{\,p}_{n+1}$, respectively, where the superscript p stands for "pre-

diction". The constants $\Delta t2F$, $\Delta t3F$, $\Delta t4F$ and $d\Delta t5F$ are Taylor coefficients with:

$$\Delta tnF = \frac{(\Delta t)^n}{n!}. \tag{3.2}$$

In the second step, the force $\vec{F}(\vec{r}_{n+1}, \vec{v}_{n+1}, t)$ = (trap-force + damping-force) is calculated. The third step is a correction of the preliminary calculated coordinates. The force which is derived in the second step is compared with $m\vec{a}^p_{n+1}$ where the difference between those two forces is a correction factor for all components

$$\begin{aligned}
\Delta\vec{F} &= \frac{1}{2}\Delta t^2\left(\frac{\vec{F}(\vec{r}_{n+1}, \vec{v}_{n+1}, t)}{m} - \vec{a}^p_{n+1}\right), \\
\vec{r}^c_{n+1} &= \vec{r}^p_{n+1} + c0 \cdot \Delta\vec{F}, \\
\vec{v}^c_{n+1} &= \vec{v}^p_{n+1} + c1 \cdot \Delta\vec{F}/\Delta t, \\
\vec{a}^c_{n+1} &= \vec{a}^p_{n+1} + c2 \cdot \Delta\vec{F}/\Delta t2F, \\
\vec{d3}^c_{n+1} &= \vec{d3}^p_{n+1} + c3 \cdot \Delta\vec{F}/\Delta t3F, \\
\vec{d4}^c_{n+1} &= \vec{d4}^p_{n+1} + c4 \cdot \Delta\vec{F}/\Delta t4F, \\
\vec{d5}^c_{n+1} &= \vec{d5}^p_{n+1} + c5 \cdot \Delta\vec{F}/\Delta t5F,
\end{aligned} \tag{3.3}$$

where the superscript c stands for "correction". The coefficients $c1...c5$ for the fifth order Gear method with a differential equation of second order are [Gea71]

$$\begin{aligned}
c0 &= 3/20, \\
c1 &= 251/360, \\
c2 &= 1, \\
c3 &= 11/18, \\
c4 &= 1/6, \\
c5 &= 1/60.
\end{aligned} \tag{3.4}$$

3.2 Test of the Gear method

In the Preparation Penning Trap, the radial motional frequencies involved in the simulation have ratios of typically $\omega_+/\omega_- \approx 10^3$, which implies a large number of necessary time steps in the simulation, since the fastest motion has to be resolved. The Gear method is fast as compared with many other integrators because the force is calculated only once per step, which is most important if the calculation of the force is complicated. With a fourth order Runge-Kutta algorithm, for example, the forces have to be calculated four times in every time step. A second advantage of the Gear method is its easy implementation. A disadvantage is that it does not conserve the energy. For this reason it is tested with different time steps for the simulated time interval of maximal 50ms as shown in Fig. 3.1. The energy of a particle in an ideal Penning trap, with a pure initial cyclotron motion is increasing in the simulation with the Gear method. One has always to decide which time step remains in an adequate energy range for the simulated

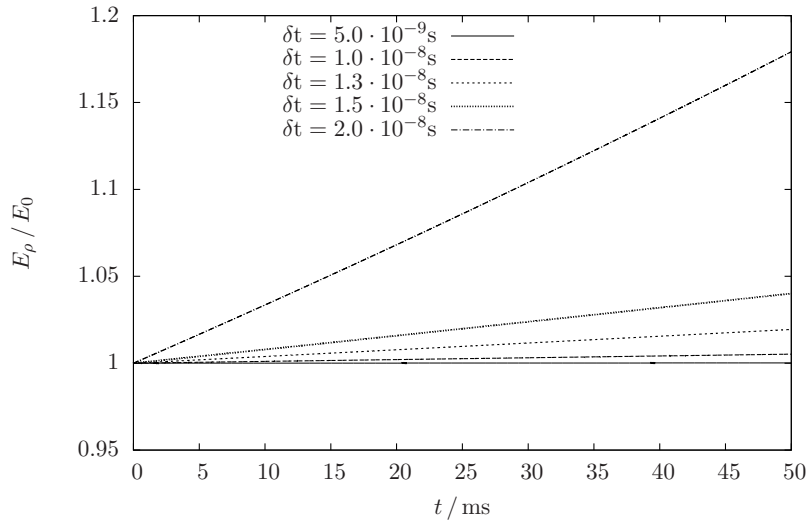

Figure 3.1: Test of the energy conservation. Radial energy normalized to the initial energy as a function of time for different time steps. The most horizontal line represents the best accuracy.

time window and which time step is reasonable for the computing time. In the further simulations for every different time window, the step is chosen so that the error for the energy is about 1% or below. Another of the most frequently used integrators is the Velocity Verlet Method [HL97] which is energy conserving, but not applicable for this problem, since it does not include a magnetic field. An energy conserving integrator for magnetic fields has been invented by J. P. Boris in 1970 but it is not easy to implement and the accuracy of the Gear method is sufficient for this case.
The simulation with the Gear method has been tested for analytical confirmed motions of a single ion in a Penning trap. As some examples, the frequencies of the radial eigenmotions, the well defined conversion frequency of a quadrupolar excitation with a certain excitation amplitude, or resonance widths for quadrupolar excitation are tested successfully.

3.3 Realistic Damping Approaches

The analytical solution for the damping of the ion motion in 2.4 includes a constant coefficient δ, where the force is directed in the opposite direction of motion. For a more realistic approach in simulations, a damping coefficient is used which depends on the relative velocity $\delta = \delta(v)$ of the ions and the buffer gas environment. A second implemented model for the simulations is a microscopic approach which takes into account the individual collisions of the ions with the buffer gas atoms and is thus the best approximation which is used for the present investigations.

3.3.1 Realistic Continuous Model with a Velocity Dependent Mobility

In this model the velocity dependency of the damping coefficient is expressed by the mobility of ions in a buffer gas. The mobility K is defined by the maximum drift speed v_d of an ion in a buffer gas affected by an electric field $\vec{E}$ [Sch08],[MM73]:

$$\vec{v}_\mathrm{d} = K \cdot \vec{E}. \tag{3.5}$$

The damping coefficient δ is related to the mobility of an ion with the mass m and the charge q by

$$\delta = \frac{q}{m} \cdot \frac{1}{K}. \tag{3.6}$$

The mobility K of an ion, colliding with buffer gas atoms of the mass M, which has the drift velocity $\vec{v}_\mathrm{d}$, is given by [Sch08]

$$K(v_d) = \frac{3e}{16 n_\mathrm{gas}} \sqrt{\frac{2\pi}{k_\mathrm{B} T_\mathrm{eff}(v_d)} \frac{m+M}{mM}} \frac{1}{\Omega(T_\mathrm{eff}(v_d))}. \tag{3.7}$$

Here n_gas is the density of the buffer gas atoms, k_B the Bolzmann constant and $T_\mathrm{eff}(v_d)$ is the effective temperature which is defined by:

$$T_\mathrm{eff} = T_{gas} + \frac{M v_d^2}{3 k_\mathrm{B}}. \tag{3.8}$$

To derive K from Eq. 3.7, the collision cross section $\Omega(T)$ has to be known. It can be calculated in the collision integral of first order, which is a theoretical expression including two integrations

$$\Omega(T) = \frac{4\pi}{(k_\mathrm{B} T)^3} \int_0^\infty e^{-\frac{E}{k_\mathrm{B} T}} E^2 \int_0^\infty (1 - \cos(\Theta(b, E))) b \,\mathrm{d}b \mathrm{d}E. \tag{3.9}$$

The first integral is summing up the square of the motional energy with the probability density of the Maxwell-Bolzmann distribution and the second integral is summing up the contribution of the scattering angle Θ in the center of mass system dependent on the impact parameter b. For a better understanding of the integral, two cases are considered. If the buffer gas would be such that the scattering angle is always zero as in a massless gas, the second integral vanishes and the mobility K is infinite, which represents the vacuum case. If the gas atoms are like fixed walls with infinite mass and infinite dimension, the scattering angle is independent of b and E and the integral diverges with the impact parameter b. Thus, the mobility would be zero.
For finite conditions the scattering angle is given by a third integration:

$$\Theta(b, E) = \pi - 2b \int_{r_a}^\infty \frac{1}{\sqrt{1 - \frac{b^2}{r^2} - \frac{V(r)}{E}}} \frac{dr}{r^2} \tag{3.10}$$

where r is the distance between the ion and the buffer gas atom and r_a the closest distance to the collision partner. For $V(r)$ realistic scattering potentials called $(n, 6, 4)$

potentials are substituted [Sch08]

$$V(r) = \frac{G}{r^n} - \frac{C_6}{r^6} - \frac{C_4}{r^4}, \tag{3.11}$$

with G, C_6, and C_4 as constants. The first term $\frac{G}{r^n}$ is a empirically determined repulsive potential and the other two terms $\frac{C_4}{r^4}$ and $\frac{C_6}{r^6}$ represent attractive interactions of the ion with electric dipolar and quadrupolar moments of the neutral atoms. For several collision partners these potentials are determined using experimental data. A discussion of such potentials is given in [Sch08] and more detailed in [MM88] and [MM73], where also the theory of collision integrals is further discussed. For the present simulations, the collision integral is calculated for ^{133}Cs ions in a ^{4}He background with different drift velocities by use of a numerical routine which has been programmed by Stefan Schwarz [Sch08]. This routine solves the three integrations for Ω including $(n, 6, 4)$ potentials. To avoid a slowing down of the simulation, the data for $\Omega(T_{\text{eff}})$ is calculated in advance for discrete values of T_{eff} and the calculated points are interpolated.

3.3.2 Elastic Collisions with Buffer Gas Atoms

In addition to the continuous damping models a routine for elastic hard sphere collisions has been programmed to investigate binary Coulomb collisions effect on the ions. Elastic hard sphere collisions are the simplest approach of a microscopic model. In every time interval Δt the probability P for the collision of an ion with a buffer gas atom is estimated by

$$P = 1 - exp(-un_{\text{gas}}\Omega(T_{\text{eff}})\Delta t) \tag{3.12}$$

with the cross section $\Omega(T_{\text{eff}})$ as used for the velocity dependent continuous damping approach. The parameter n_{gas} is the density of the buffer gas atoms as an ideal gas, Δt the time step in the simulation, and u the absolute value of the velocity difference between the collision partners with

$$\vec{u} = (v_d - v_{gas}) \cdot \vec{e}_{\text{rand}}. \tag{3.13}$$

The mean velocity of the gas atoms v_{gas} is randomly determinated by the Maxwell-Bolzmann distribution and $\vec{e}_{\text{rand}}$ is the unit vector with a random direction which is taken from a uniform distribution. The further procedure will be just briefly discussed at this point.
The initial velocity of the ion is

$$\vec{v} = \vec{v}_{c.m.} + \frac{M}{m+M}\vec{u}, \tag{3.14}$$

where $\vec{v}_{c.m.}$ is the velocity of the center of mass. And the final velocity after the collision is

$$\vec{v}' = \vec{v} + \frac{M}{m+M}\Delta\vec{u}. \tag{3.15}$$

The vector $\Delta\vec{u}$ describes the difference of the initial u to the final u' after turning $\vec{u}$ by the scattering angle Θ in axial direction and afterwards by the angle ϕ taken from

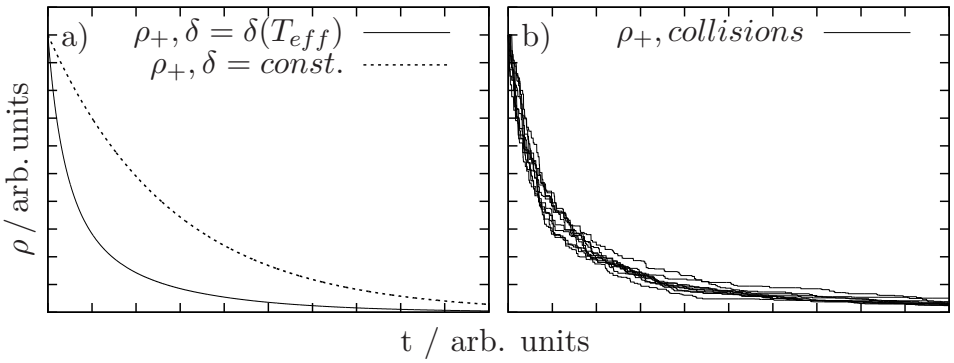

Figure 3.2: Cyclotron radius as a function of time in a buffer gas environment without excitation. (a) The motion is simulated with both a velocity independent damping force (dotted line), and a damping force using Eq.(3.7) (solid line). (b) Trajectories of 10 ions with equal initial conditions affected by elastic collisions with the buffer gas atoms.

a uniform distribution in radial direction. In the case of ideal elastic collisions the scattering angle is derived by:

$$\cos(\Theta) = 1 - 2R \tag{3.16}$$

where R is a random number from a uniform distribution from 0 to 1. The energy is conserved because the absolute value of u is not changed. A complete description of the procedure can be found in [Mat].

The radial energy loss in a buffer gas environment for the three different damping models discussed in the present thesis is illustrated in Fig 3.2. The values for the velocity independent damping constant are taken from measurements with low drift velocities [EMA+78]. It is an adequate approach to show basic effects in a cooler trap as in 2.4, but the drift velocities in the performed trap experiments are two orders of magnitude larger than in the experiments for the known mobility data. It is possible to adjust the constant also for larger drift velocities, but other experiments for the determination of the mobility have to be performed in advance. If the mobility is considered to be velocity dependent $\delta = \delta(T_{\text{eff}})$ with Eq. (3.7), the model differs from the damping model with the measured constant coefficient in the sense that the cooling time is smaller for the same pressure since there is a more rapid loss of energy for fast ions as shown in Fig 3.2 (a). In Fig 3.2 (b) the cyclotron radii of 10 ions, simulated with elastic collisions, are plotted. The motion with collisions is related to the motion with $\delta = \delta(T_{\text{eff}})$ because a fast drift velocity increases the collision rate and thus the energy loss of the ions is much faster than for slow ions. The radial energy affected by collisions is decreasing to the energy level of the background and further fluctuating around this value.

3.4 Comparison of the OES and the QES in a Simulation for the Cooling Process

A complete characteristic of an excitation scheme in a cooling process includes a determination of the resolving power $R_p = \nu_{\mathrm{exc}}/\Delta\nu_{\mathrm{H}}$, of the efficiency $N_{\mathrm{ion}}/(\text{ion counts})$, and the resulting distribution of magnetron radii of the ions as an estimate for the quality of the centering, where the remaining cyclotron radii are not considered, because they vanish quickly in a buffer gas. The centering quality is represented by the arithmetic average $\overline{\rho_{-,\mathrm{f}}} = \sum_{i=1}^{N_{\mathrm{ion}}} \rho_{-,\mathrm{f_i}}/N_{\mathrm{ion}}$ of the final magnetron radii $\rho_{-,\mathrm{f_i}}$ of the ions. N_{ion} is the total number of ions (see Fig. 3.3). To obtain results close to the experiment as a determination of the efficiency, the resonance shapes are described by the accumulated ions close to the center which means that $\rho_{-,\mathrm{f}} < \rho_{\mathrm{D}}$ after the excitation, where ρ_{D} is the radius of the diaphragm. This means that a resonance curve is represented by the counted events as a function of the frequency. Since all properties are dependent on the buffer gas pressure and the excitation amplitude, a two dimensional array of parameters is scanned to obtain an overview of the behavior. For these simulations, two damping approaches are used, the model with a velocity dependent damping coefficient $\delta = \delta(T_{\mathrm{eff}})$ and the model which implements elastic collisions with the buffer gas atoms. A fixed damping constant δ has been used only for the theoretical discussion in 2.4.

3.4.1 Procedure and Initial Conditions

The procedure of the simulation is subdivided in runs and sequences. In a run the three properties R_p, $\overline{\rho_{-,\mathrm{f}}}$, and the efficiency of the cooling process are determined for a fixed pressure and amplitude. In every run several sequences with initialization, excitation

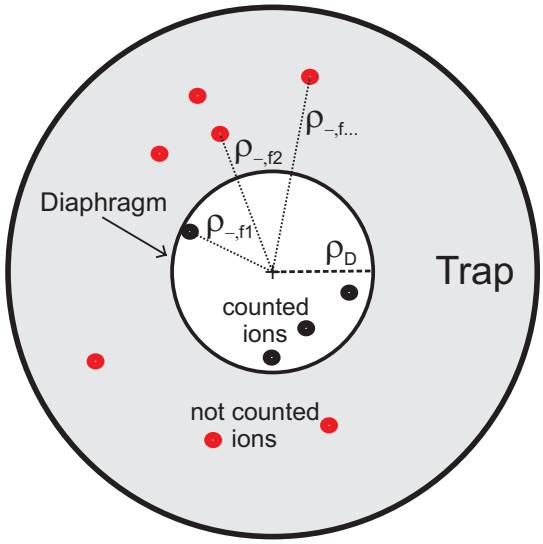

Figure 3.3: Sketch for the determination of the efficiency and the average radius of the ions.

at a certain frequency, and evaluation are performed as discussed in the following.
The simulated ion specie is $^{133}Cs^{+}$ and the buffer gas atoms are ^{4}He. In every sequence the particles are initialized with a 3-D Gaussian distribution in space which has a mean distance of 5 mm from the trap center. The radius of the diaphragm ρ_D is set to 1.5 mm as in the experiment. The width of the initial bunch is determined in simulations for ion pre-cooling, as also performed for the measurements, with statistically ideal collisions at three different pressures. The pre-cooling is simulated with respect to the applied real times in the measurement. The results are shown in Tab. (3.1). In the initialization

Table 3.1: Results from a simulation for the bunch width after pre-cooling of ions at different pressures. δ_ρ and δ_z: Standard deviation of the Distribution in radial and axial direction.

p / mbar	δ_ρ / mm	δ_z / mm
$5 \cdot 10^{-5}$	1.0	2.3
$1 \cdot 10^{-4}$	0.8	1.3
$2 \cdot 10^{-4}$	0.5	0.8

the points for the bunch-width are interpolated with lines, where the bunch width for $5 \cdot 10^{-5}$mbar is also used for pressures below. The excitation amplitude in both excitation schemes is chosen so that $U/U_B < 6$, which means that without collisions from zero up to three conversions from magnetron to cyclotron motion and vice versa are taking place for an ion which is initialized in the center of the Gaussian distribution. For the parameter area of the simulation, the maximum amplitude is divided into 100 steps and the pressure is scanned from $p = 6.0 \cdot 10^{-6}$mbar to $p = 1.74 \cdot 10^{-4}$mbar in 30 steps. After the initialization the ions are excited for 50 ms.
The first step of a run is the determination of the efficiency and the average of the final magnetron radii $\overline{\rho_{-,\mathrm{f}}}$ in five sequences for 20 ions in each sequence which are excited with the frequency $\nu_0 = \nu_c$ for quadrupolar excitation or $\nu_0 = 2\nu_c$ for octupolar excitation. As a next step the frequency is detuned to a point ν_1 where the ions are not centered and afterwards the bisection method is applied to search the half maximum of ion counts with respect to the efficiency as shown in Fig. 3.4. With the application of the bisection method the simulation can be much faster as compared with a simulation of complete resonance curves with fixed grid if the starting conditions are chosen adequate. In addition the relative uncertainty for the determination of $\Delta\nu_H$ is independent from the total width of the resonance shape, which is not the case in a simulation with fixed grid points. The process is terminated if the interval $|\nu_{n+1} - \nu_n|$ for the next bisection step is below 5% of the actual difference $|\nu_n - \nu_c|$ for the QES or $|\nu_n - 2\nu_c|$ for the OES. Finally the resolving power is estimated as $2\,|\nu_n - \nu_c|\,/\nu_c$ for quadrupolar excitation and analog for octupolar excitation with twice the cyclotron frequency. The determination of R_p is completely skipped for points (pressure, amplitude) with an efficiency lower than 30%, where R_p is set to zero.
The simulations are parallelized easily, since the procedure for each pressure and amplitude is not changing, and they are performed with up to 50 computers on a cluster, which have been offered by the COMAS group [com] for this time.

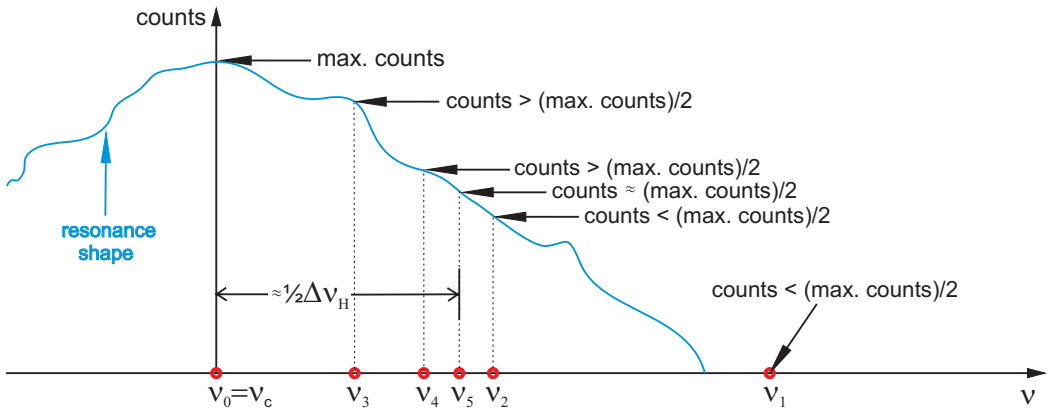

Figure 3.4: Sketch of the bisection algorithm which is searching the half maximum of the resonance shape. The number of maximal counts in the central peak is determined by the efficiency $N_{\mathrm{ion}}/(\mathrm{ion\,counts})$. The illustrated resonance shape is drawn freehand for the illustration of the method.

3.4.2 Bisection Method and Resonance Shapes

A challenge for the application of the bisection method is the shape of resonances with multi-peak structure, which leads to ambiguities of the width value as shown in Fig. 3.5 (a). Note that the resonance can be flat near the center, if all ions are centered in a

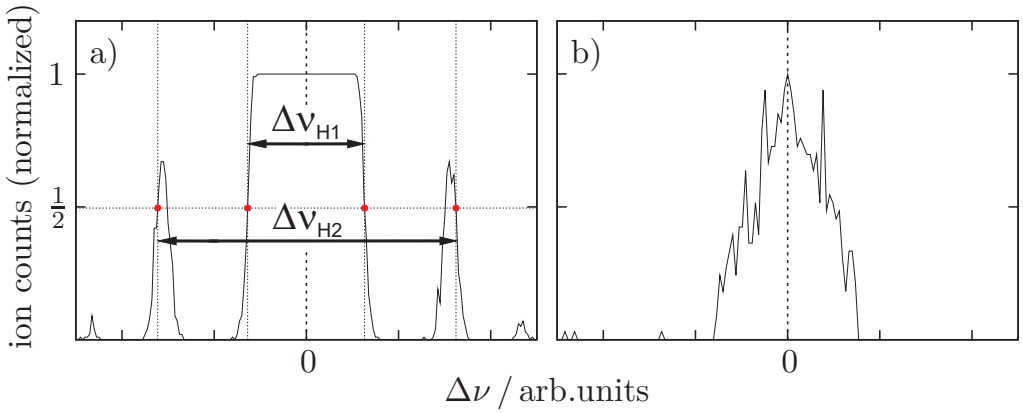

Figure 3.5: Counts of ions as a function of the frequency detuning $\Delta\nu$. Part (a): Resonance for quadrupolar excitation for $U/U_{\mathrm{B}} = 9$ with large secondary maxima. Part (b): Octupolar resonance curve from an initial Gaussian ion distribution in space.

frequency region around the resonance frequency. In advance one has to investigate, if the resonance curves are free of relevant secondary maxima inside the simulated parameter area. For the OES this is indeed the case for this simulation because the phase related secondary maxima near the central peak are smearing out to a broader peak in case of an initial Gaussian distribution of ions in space (Fig. 3.5 (b)). Some amplitudes lead to double peak structures for the OES as discussed in 2.5, thus the starting point for the binary search has to be outside of the two peaks. In a QES, the secondary maxima are not vanishing, even with a spacial ion distribution. For this reason it has been confirmed, that if the initial magnetron radius is chosen so that $\rho_{-,0} > 1.7 \cdot \rho_\mathrm{D}$ and $U/U_\mathrm{B} \leq 6$, which is always the case, the number of ions in the secondary maxima is too small for ambiguities of $\Delta\nu_\mathrm{H}$.
Furthermore, a nearly symmetric resonance shape is assumed. For a QES this assumption is valid, since the initial conditions in the simulations are chosen so that $\rho_{+,0} = 0$ and thus the motion is phase independent (see 2.3.4). For an OES this is also given because the asymmetries are caused by phase related phenomena which are averaged by the spacial ion distribution. With the assumption of a symmetric shape the simulation time is reduced by a factor of two.

3.4.3 Results for R_p and the efficiency from the Simulations with a continuous damping model $\delta = \delta(T_\mathrm{eff})$

The results for the resolving power and the efficiency of the simulation are displayed as contour plots in Fig. 3.6. In the diagrams, the efficiency has always values from 0 to 1, where 0 stands for 0 % and 1 stands for 100 %. The simulation for the QES agrees with the expectations. If the pressure is low as $4.0 \cdot 10^{-5}$mbar or below, the ions are able to leave the center for $U_\mathrm{q}/U_\mathrm{B} \neq 1, 3, 5$, which is not the case for larger pressures as $p = 8.0 \cdot 10^{-5}$mbar or higher, where the maximal possible radius $\rho_- + \rho_+$ decreases to a value below ρ_D within the excitation time. The maximal obtained values for the resolving power for single points are $R_p \approx 1.2 \cdot 10^5$ for $U_\mathrm{q}/U_\mathrm{B} \approx 1$ and pressures as $p = 5.0 \cdot 10^{-5}$mbar or below. If a few points are taken into account, the maximal mean resolving power is $R_p \approx 8.0 \cdot 10^4$ in this region. One can see that the resolving power in the QES is decreasing for $U_\mathrm{q}/U_\mathrm{B} = 3, 5$ as compared with $U_\mathrm{q}/U_\mathrm{B} = 1$ due to the broader width of the resonances for higher amplitudes (see 2.3.5). Also the decreasing of the resolving power for increased pressures, as discussed in Fig. 2.10 (b) in 2.4.1, is reproduced. If the amplitudes are chosen such that the final magnetron radius is close to the radius of the diaphragm, the resolving power is maximal (see 2.4.2). The efficiency plot for the QES shows that it is possible to center all ions if the amplitudes are chosen correctly.
For the OES, the magnitude of the resolving power is higher, and the structures in the diagrams for the resolving power and the efficiency are different from those of the QES. The most of the points in the diagram for the resolving power are plotted as black points, since the resolving power is decreasing very fast with the distance to the optimal parameters in the parameter area. The maximal obtained resolving powers are obtained for a pressure of $p = 4.0 \cdot 10^{-5}$mbar or below with values up to $R_p \approx 1.0 \cdot 10^7$. For a higher pressure as $p = 5.0 \cdot 10^{-5}$mbar, a maximal resolving power of $R_p \approx 5.0 \cdot 10^6$

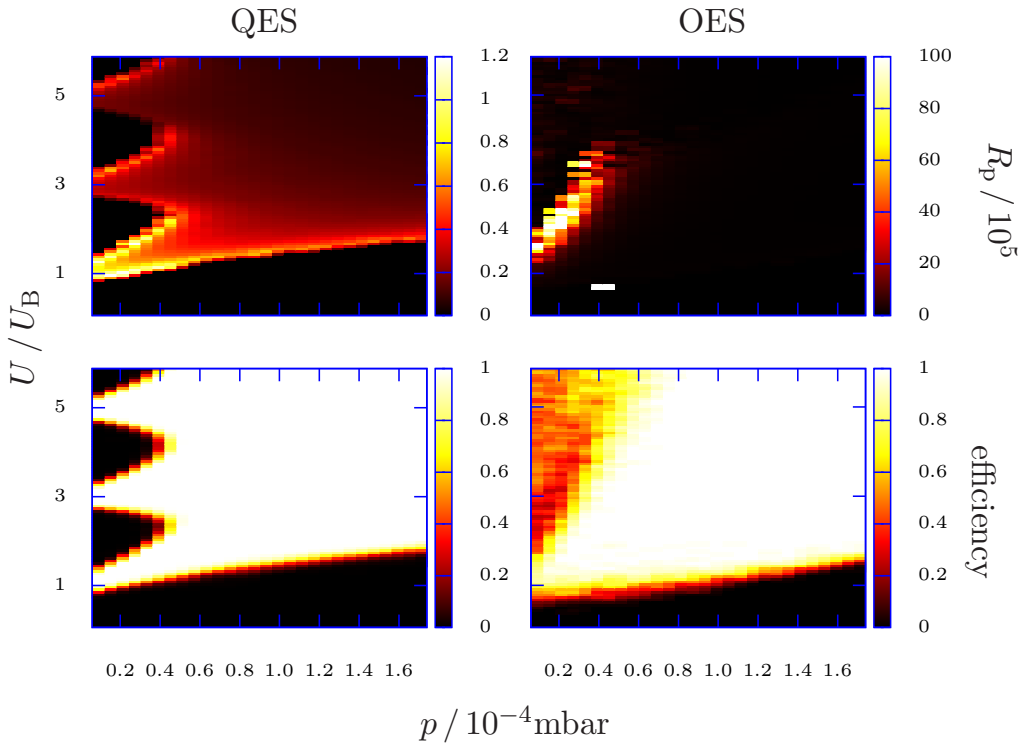

Figure 3.6: Resolving power (top) and efficiency (bottom) of the cooling process for $^{133}Cs^+$ ions as a function of the pressure and the excitation amplitude, which is normalized to U_B. The results are given for the QES (left) and the OES (right).

is obtained, and for $p = 1.0 \cdot 10^{-4}$mbar the resolving power is up to $R_p \approx 1.0 \cdot 10^5$ (not visible in the diagram), which is still in the same range as the maximum for the QES. The maximal values of the resolving power are not obtained for $U_{oct}/U_B \approx 1$ as for the QES, but for amplitudes where the ions begin to leave the trap center due to the conversion back to magnetron motion, which can be seen in the efficiency plot for the OES. For lower amplitudes, where the ions enter the trap for the first time, the resolving power does not reach the same order of magnitude as compared with amplitudes where the ions leave the trap center, except for four isolated points in a block ($p = 4.0 \cdot 10^{-5}$mbar, $U_{oct}/U_B \approx 0.5$). These isolated points are not yet understood, but the higher resolving power for amplitudes where the ions leave the trap center is obtained by the typical resonance shapes of the OES as in Fig. 2.14 in 2.5.2, which are narrow for points where the conversion back to magnetron motion is beginning.
In the plot for the efficiency of the OES, it is noticeable that for pressures as $3.0 \cdot 10^{-5}$mbar and below, the second and third maximum of the efficiencies for higher amplitudes, as obtained for the QES, is missing. This effect is obtained by the distribution of the beating frequencies ν_B as shown in Fig. 3.7. 100 Particles with a spatial Gaussian

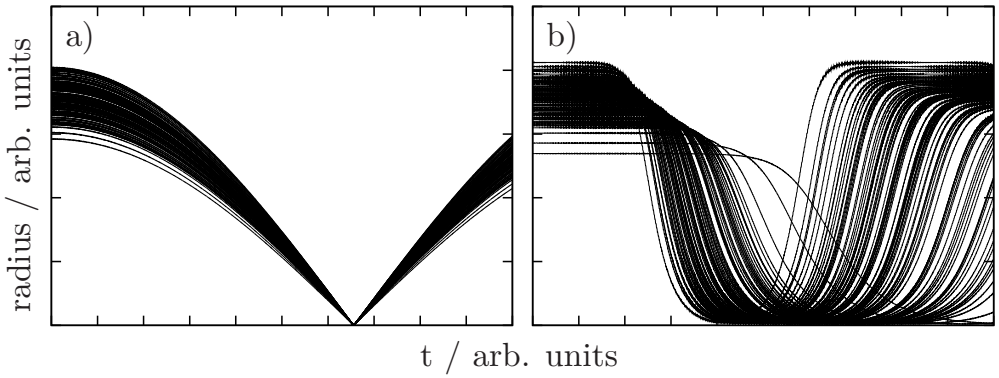

Figure 3.7: Magnetron radii of 100 equal ions as a function of the time for quadrupolar (a) and octupolar (b) excitation in a vacuum environment. The ions are initialized with a Gaussian distribution in space.

distribution are excited in a vacuum environment with a QES in (a) and with an OES in (b). The beating frequency in a QES is independent from the initial radius and thus all ions reach the trap center in the same moment. This is not the case for the OES, because the quadratic dependency of ν_B on the initial radial distance from the trap center leads to an asynchronous motion of spacial distributed ions. Note that for this reason it is not possible to define an amplitude as $U_\mathrm{oct}/U_\mathrm{B} = 1$ for all ions precisely, but for the mean of the ions, which can be seen in the efficiency plot.

3.4.4 Results for R_p and the efficiency from the Simulations with Elastic Collisions

In the experiment, the ions are colliding with buffer gas atoms. Since the ion motion in the OES results in a nonlinear behavior with a high sensitivity to the initial conditions, a continuous damping model might not be sufficient for the description of experiments with the OES. For this reason, the same simulations have been performed with a microscopic collision model. The results for the resolving power and the efficiency of the simulation with elastic collisions for both excitation schemes are displayed as 3-D contour plots in Fig. 3.8. For the QES, the simulation results in comparable values as the simulation with the continuous model, for the resolving power and also for the efficiency. The resolving power is maximal in the region where $U_\mathrm{q} \approx U_\mathrm{B}$, and decreases with every further conversion and as well for larger pressures. The highest mean values for R_p, which are simulated in the parameter area, are around $R_p \approx 8.0 \cdot 10^4$ for the QES. Single points for amplitudes, where the final ion position is close to the border of the diaphragm (see 2.4.2), have R_p values of up to $1.0 \cdot 10^5$. The maximal pressure where the ions are still able to leave the center ($p = 6.0 \cdot 10^{-5}$mbar) of the trap is higher than in the simulation with the continuous model, which can be seen also in Fig. 3.2. An

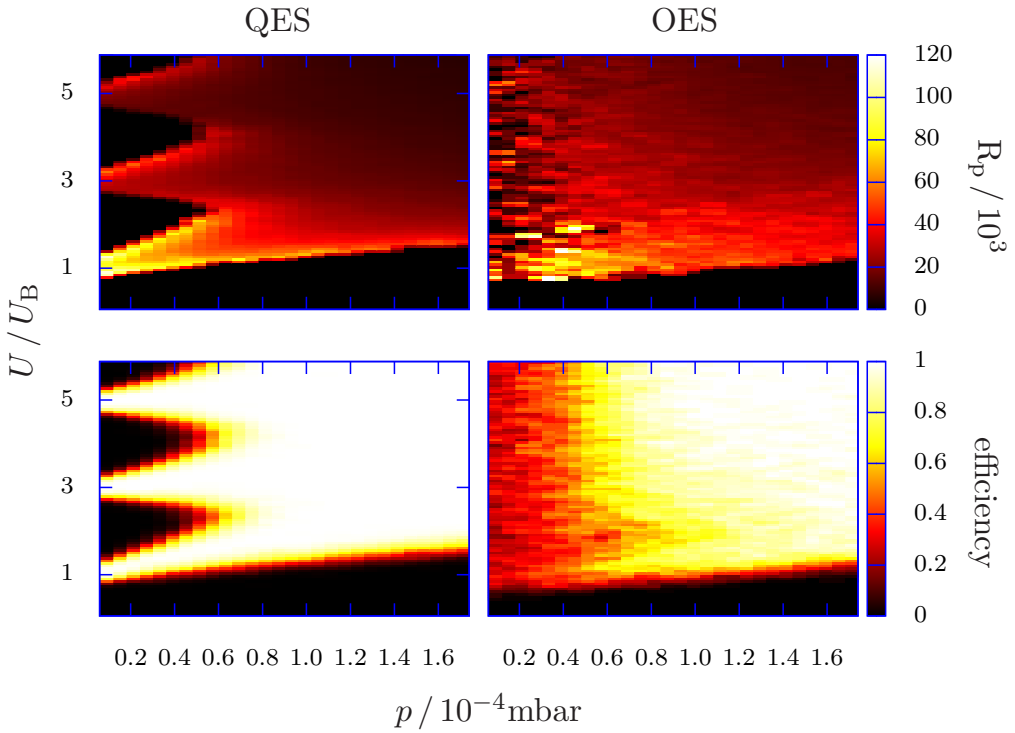

Figure 3.8: Resolving power (top) and efficiency (bottom) of the cooling process for $^{133}Cs^+$ ions as a function of the pressure and the excitation amplitude, which is normalized to U_B. The results are given for the QES (left) and the OES (right).

efficiency of 100% is always achived for correct chosen amplitudes. For the resolving power and the efficiency, both damping schemes have comparable results which means that the ion motion in a QES is stable, even if the velocity of an ion is changed instantly as in a collision scheme.
In the OES, the motional behavior differs clearly from the simulation with the continuous damping scheme. The maximal obtained resolving powers are $R_p \approx 10^5$, which is a factor of 100 less than the possible resolving power in the simulation with the continuous damping model. Thus, the R_p values of the QES and the OES can be plotted in the same range, which confirms that the disturbances in the buffer gas environment have a strong effect on the ion motion in the OES. An increased resolving power for amplitudes where the ions begin to leave the center of the trap for the first time, as obtained with the continuous damping model, can not be observed.
A significant loss of ions is obtained for pressures as $p = 8.0 \cdot 10^{-5}$mbar and below, and even for higher pressures the efficiency is decreased as compared to the simulation with the continuous model. This means that the conversions are interrupted by the collisions, since if a conversion takes place, the efficiency would be always 100 % for the higher

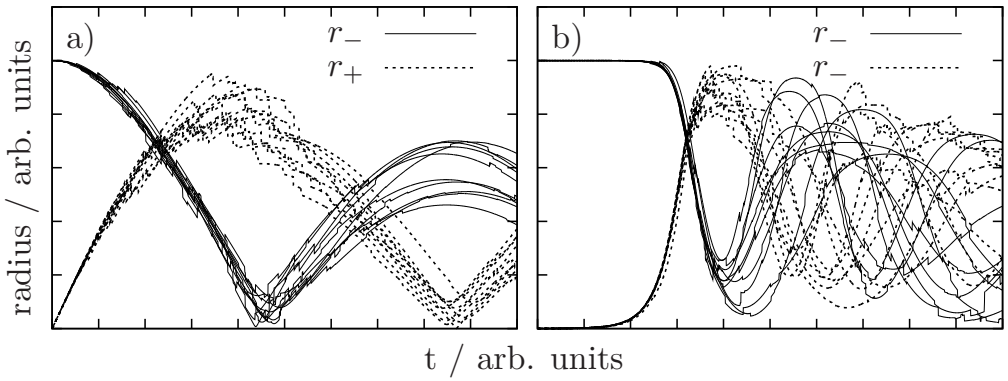

Figure 3.9: Motion of 10 $^{133}Cs^+$ ions in a QES (a) and OES (b) as a function of the time. The motion is affected by statistically ideal collisions with ^4He atoms. All ions are initialized with the same conditions.

pressures. The disturbances due to the collisions which lead to these effects can be seen in Fig. 3.9. In a QES, the conversion is disturbed, but the ions keep a motion close to the continuous damping scheme. The ions in an OES react on the new conditions after the collision and the trajectories appear to be chaotic, which prohibits a complete conversion and a good centering, especially for low pressures. The ions in Fig. 3.9 are initialized with the same conditions to show that a very precise initial distribution in space would not change these effects.

3.4.5 Results for the Centering Quality from Both Simulations

The third property which has been diagnosed is the averaged final magnetron radius $\overline{\rho_{-,\mathrm{f}}}$ when the process is finished. A small value of $\overline{\rho_{-,\mathrm{f}}}$ stand for a good quality of the ion centering. The results for both models are shown in Fig. 3.10, where the reciprocal of $\overline{\rho_{-,\mathrm{f}}}$ is plotted to obtain a visible result for small values. In the simulation with the continuous damping model, the ions are much better centered for optimal amplitudes in both excitation schemes. The shape for the QES does not change qualitatively. For the OES it is possible to center the ions, whereby the fact, that for each pressure just one optimal amplitude range exists, is understood in Fig 3.7. In the simulations with elastic collisions, the QES centers the ions much better than the OES for optimal amplitudes. In the OES, the shape of $1/\overline{\rho_{-,\mathrm{f}}}$ is flat and even in the regions where the efficiency is 100%, the ions keep a larger mean magnetron radius, which could lead to transport problems of the ions for the next experimental step. The simulations with elastic collisions predict a better experimental applicability for the QES as compared to the OES.

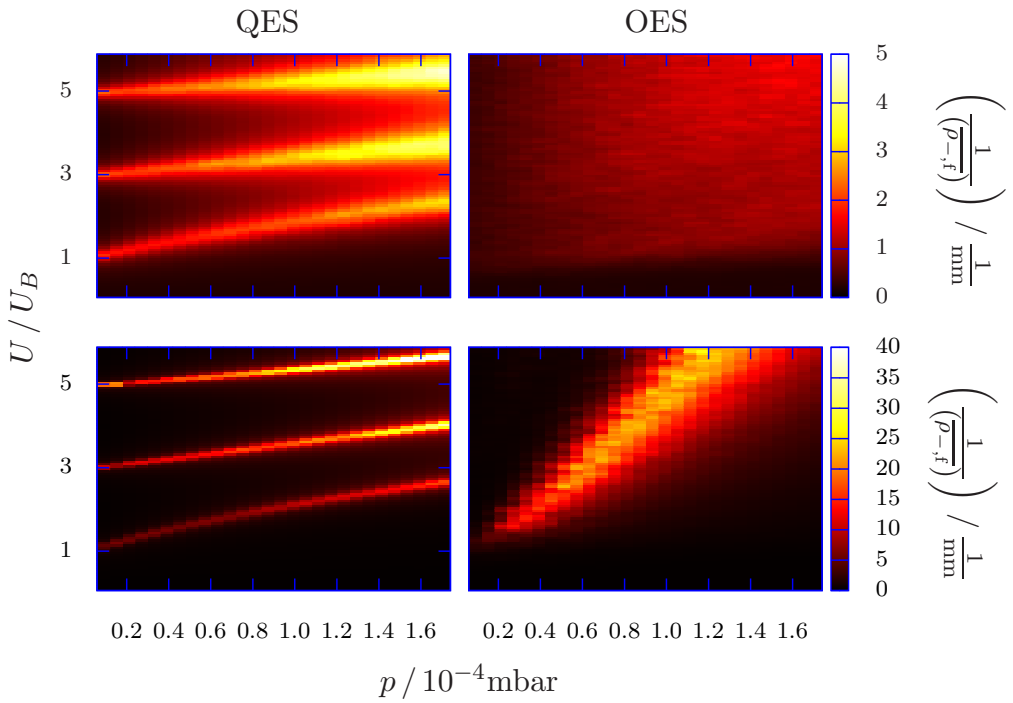

Figure 3.10: Cooling quality $1/\overline{\rho_{-,\mathrm{f}}}$ for $^{133}Cs^{+}$ ions as a function of the pressure and the excitation amplitude, which is normalized to U_B. The results are given for the elastic collision model (top), and for the continuous damping model (bottom), for both the QES (left) and the OES (right).

4 Experimental Setup

In the following the ISOLTRAP experiment with its main components, and the measurement principle will be introduced. The part of the setup, which is used for the experimental investigations in the present work, will be described in detail.

4.1 The ISOLTRAP Experiment

ISOLTRAP [MKB+04] is a mass spectrometer for high accuracy mass measurements of exotic short-lived nuclei, which is located in the ISOLDE facility at CERN. The ISOLDE facility is an on-line device for the production of radioactive ion beams. The hours or days when the beam of ISOLDE is delivered and ISOLTRAP performs the normal operation for mass measurements, are called "beam times". A large spectrum of radioactive atoms is produced by highly energetic protons which are focused on a thick target [Kug00]. The produced ensemble contains many species of radioactive elements which are later ionized and accelerated to a kinetic energy of 60 keV. The fast beam is separated in one of two different mass separators. After the separation, the beam is still contaminated with isobars and also isomers of each species. The ions are transported to the ISOLTRAP experiment and afterwards cooled, bunched, and purified from contaminants, so that the mass of a single ion specie and energetic state can be measured. For this purpose, three ion traps are used (Fig. 4.1). The first trap is a linear radio frequency quadrupole (RFQ) [HDK+01] in a high voltage cage which is floated to 60 kV, where the ions are decelerated and accumulated, cooled and bunched. The second is a cylindrical Preparation Penning Trap, where the ion bunch is further cooled and purified from isobaric and isomeric contaminants [SBB+91]. The third trap is a hyperbolic Precision Penning Trap, which is dedicated to perform mass measurements with a relative uncertainty of down to $\delta m/m = 10^{-8}$, using the ToF-ICR (time of flight ion cyclotron resonance) method. With the ToF-ICR method, the determination of the mass is performed by the determination of the cyclotron frequency ν_c. Therefore a channeltron detector is located above the Precision Penning Trap. For optimization, the system is equipped with other MCP detectors which are distributed in the setup. The transfer between the three traps is performed with a system of electrostatic einzel lenses, deflectors and two pulsed cavities. The first pulsed cavity is placed behind the RFQ in order to lower the 60 keV potential energy to 3 keV for the transport through the system and the second drift tube further decelerates the ions to a few eV for the injection into the Preparation Penning Trap (see Fig. 4.1).

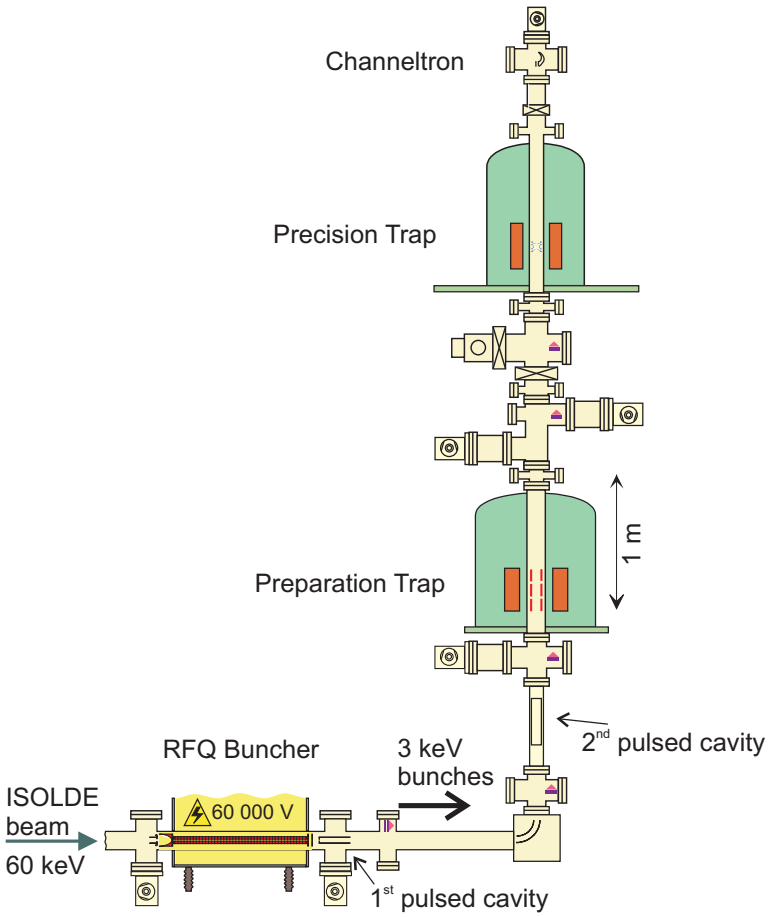

Figure 4.1: Sketch of the experimental setup of the ISOLTRAP mass spectrometer with tree ion traps for preparation, cooling and mass determination of radioactive ions from the ISOLDE facility.

4.2 RFQ Buncher

The ISOLTRAP experiment receives a continuous ion beam with a kinetic energy of 60 keV from the ISOLDE facility. The RFQ buncher [HDK+01] is a linear Paul trap which is used to decelerate the continuous beam and convert it to a discrete low energy ion bunch. The high energy ion beam is retarded to a few eV by a deceleration electrode which is installed in the injection region of the buncher and floated by the potential of the high voltage cage. After the injection which is controlled by a pulsed electric barrier (beam gate), the ions are scattering with helium buffer gas atoms. This leads to a centering of all captured ions in the radial and axial potential minimum, where the axial potential minimum is realized by a segmentation of the rods. The radial confinement is achieved by a radio frequency field. The cooled bunch of ions is further transfered towards the Preparation Penning Trap.

4.3 Preparation Penning Trap

The Preparation Penning Trap is a cylindrical trap [Bec93] which is placed in a 4.7 T superconducting magnet. It is dedicated to trap the ion bunch coming from the buncher, separate the ions of interest from contaminants, and center the selected ions. For this purpose the buffer-gas cooling technique is used [SBB+91], [KBK+95] (see 2.4.1).
The trap consists of 13 cylindrically shaped electrodes as shown on the photo in Fig. 4.2 (a). The ring electrode in the axial center is divided into eight equally sized segments for the application of excitation signals. Four electrodes on the outer side form the endcaps as illustrated in Fig. 4.2 (b). Two additional correction electrodes are placed on each side of the ring electrode to realize a well approximated harmonic axial potential [Bec93]. The applied voltages at the electrodes for the trapping mode and the ion ejection are listed in Tab.4.1, whereby the elements are listed one after another from the lower end to the upper end of the trap.
In the normal operation of ISOLTRAP, the cooling and purification process starts with the ion capture by switching the lower endcap electrodes to ground potential. The large inner radius of 20mm ensures an efficient capturing of ions. Then the lower endcap is switched to 100 V for the trapping mode. First a dipolar excitation at the magnetron frequency ($\nu_- \approx 300\,\mathrm{Hz}$) is applied to 2 ring segments whereby the magnetron motion is increased to a radius larger than the diaphragm radius with $\rho_D = 1.5\,\mathrm{mm}$ (Fig. 4.2 (b)). Then, a quadrupolar excitation signal at ($\nu_c = (1/2\pi)(q \cdot B/m) \approx 547750\,\mathrm{Hz}$ for $^{133}Cs^+$ ions) is applied to perform the buffer gas cooling technique. Afterwards, the electrodes are switched to an extraction potential (Tab.4.1) which accelerates the ions towards the Precision Penning Trap. The magnetron radius of the non resonant excited

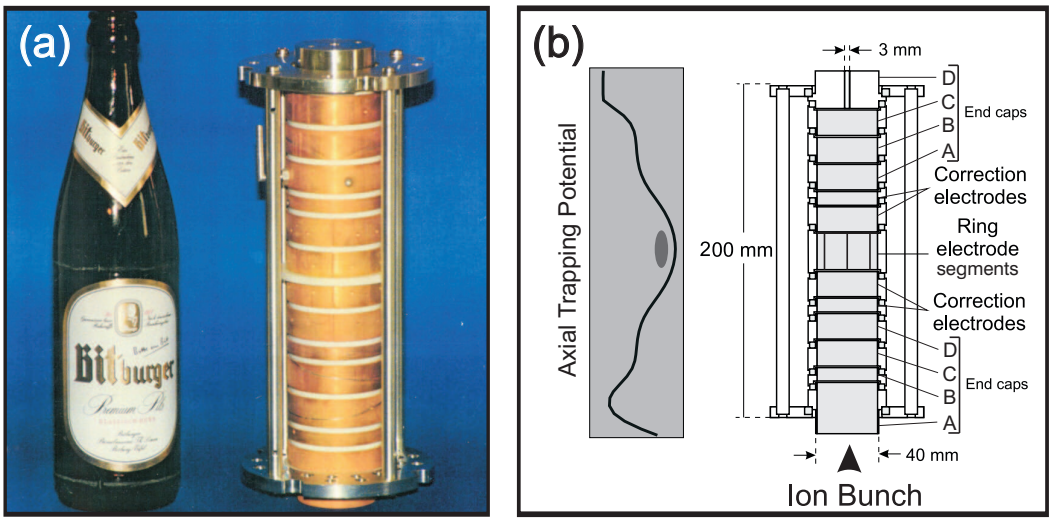

Figure 4.2: Cylindrical Preparation Penning Trap with 13 electrodes. Photo of the trap (length: 20 cm), b) sketch of the construction and the axial potential of the trap [Bec93].

Table 4.1: Voltages which are applied to the the 13 elements (first column) of the Preparation Penning Trap for the trapping mode (second column) and the ion ejection (third column) [MBB+08].

Element	Trapping Voltage/V	Ejection Voltage/V
LowerEndcapA	+100	+10
LowerEndcapB	+14	+20
LowerEndcapC	+10	+20
LowerEndcapD	+10	+20
LowerOutherCorrectionRing	+3.5	+5.2
LowerInnerCorrectionRing	−6.6	+1.5
RingElectrode	−10	−10
UpperInnerCorrectionRing	−6.6	−19.6
UpperOutherCorrectionRing	+3.5	−24.7
UpperEndcapA	+10	−30
UpperEndcapB	+10	−39
UpperEndcapC	+10.5	−45
UpperEndcapD	+100	−50

ions remains $\rho_- > \rho_D$ and they collide with the electrodes during the extraction. The Preparation Penning Trap, as used in the normal operation, has a resolving power of $2.0 \cdot 10^4$ to $1.0 \cdot 10^5$ which allows to purify the ion bunch. Further investigations of the resolving power are performed with measurements in 5.3.

4.4 Precision Penning Trap and Discussion of the Mass Measurements

The mass measurements are performed in a hyperbolic Precision Penning Trap. It is located in a superconducting magnet with $B = 5.9\,\mathrm{T}$ at the position of the trap. A photo of the trap is shown in Fig. 4.3. The Precision Penning Trap consists of a ring electrode which is divided into four segments for the realization of a dipolar and a quadrupolar excitation field, and two endcaps. The purified and cooled ion bunch, coming from the Preparation Penning Trap, enters the Precision Penning Trap with a low energy spread. A dipolar excitation with the frequency ν_-, applied to two opposite segments at the ring electrode, enlarges the magnetron radius. To obtain the same resulting magnetron radius in all experimental cycles, a phase sensitive dipolar excitation is performed. Afterwards a quadrupolar excitation with $k_0 \cdot T_{exc} = \pi/2$ (see 2.3.5) is applied with ν_q in the vicinity of $\widetilde{\nu_c}$, with $\widetilde{\nu_c}$ as the expected cyclotron frequency of the ion. If the frequency hits the cyclotron frequency ν_c of the ions, the magnetron motion is converted completely into reduced cyclotron motion and the radial energy is maximal. The obtained orbital magnetic moment μ of the ions is directly related to the radial energy [GKT80]

$$E_\rho = \mu(\nu_\mathrm{q}) \cdot B = \frac{m}{2}(4\pi^2)\left(\rho_+(\nu_\mathrm{q})\right)^2 \nu_+^2, \tag{4.1}$$

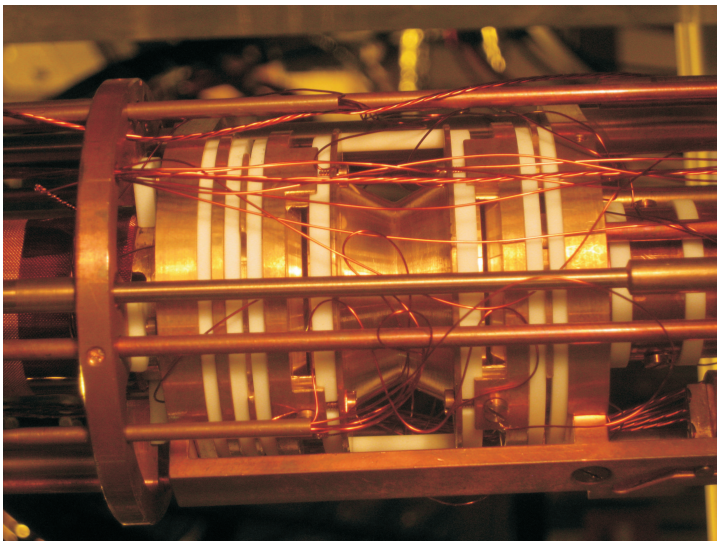

Figure 4.3: Photo of the hyperbolic Precision Penning Trap of ISOLTRAP [SBB+90],[OBS+93].

with

$$\mu \approx \pi q \cdot (\rho_+(\nu_\mathrm{q}))^2 \cdot \nu_+ \tag{4.2}$$

under the assumption that $\omega_- \ll \omega_+$. After the excitation, the ions are ejected from the trap and pass the inhomogeneous region of the magnetic field on the way to the detector as shown in Fig. 4.4. In the gradient of the magnetic field ($\partial B/\partial z$), the ions

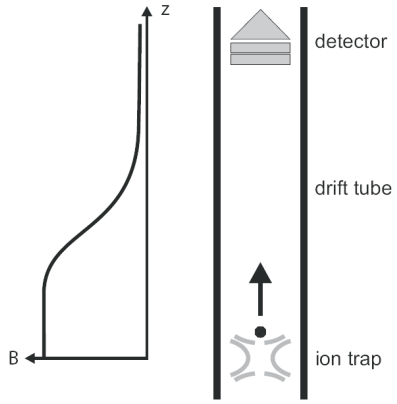

Figure 4.4: Sketch of the Precision Penning Trap and ToF section with the gradient of the magnetic field.

are accelerated due to their magnetic moment [GKT80].

$$\vec{F} = \vec{\mu}\left(\vec{\nabla} \cdot \vec{B}\right) \tag{4.3}$$

This happens in a drift section with a constant electrical potential. If $\nu_q \neq \nu_c$, the conversion is not complete as discussed in 2.3.5 and the time of flight is not decreased. To determine the cyclotron frequency, the quadrupolar excitation frequency is scanned in the vicinity of $\tilde{\nu}_c$, with $\tilde{\nu}_c$ as the expected ν_c. In Fig. 4.5, the result of a measurement is illustrated, which shows a ToF resonance of the new isotope $^{229}Rn^+$, which has been discovered at ISOLTRAP in 2008 [NAB+09].
The magnetic field is time dependent due to temperature shifts and it has to be calibrated by frequency measurements of a well known reference ion such as $^{133}Cs^+$, $^{85}Rb^+$, or carbon clusters [MKB+04]. The frequency of the ion of interest is measured in between two reference measurements, whereby the two measured points for the magnetic field are approximated with a straight line. The mass of interest is then calculated with

$$\frac{m_{\text{ion}}}{m_{\text{ref}}} = \frac{(\nu_{\text{ref}\,1} + \nu_{\text{ref}\,2})/2}{\nu_{\text{ion}}}, \tag{4.4}$$

$$m_{\text{ion}} = \frac{(\nu_{\text{ref}\,1} + \nu_{\text{ref}\,2})/2}{\nu_{\text{ion}}} \cdot m_{\text{ref}}, \tag{4.5}$$

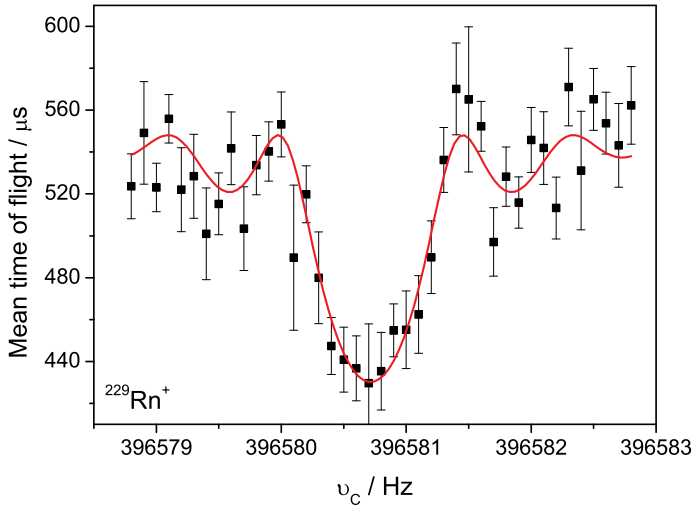

Figure 4.5: ToF resonance: mean time of flight as a function of the excitation frequency ν_q for $^{229}Rn^+$ ions. The minimum in the main peak is centered at the ions cyclotron frequency.

where $\nu_{\mathrm{ref}\,1,2}$ are the determined cyclotron frequencies of the reference ion before and after the measurements of ν_{ion}. Eq. (4.4) and (4.5) are limited to the case that the measurement for the ion of interest is in the middle of the time window between the two reference ions.

4.5 Off-Line Reference Ion Sources

At the present, two independent reference ion sources are placed at ISOLTRAP as shown in Fig. 4.6. On the ISOLDE side of the RFQ buncher, a surface ion source is installed in the high voltage cage and produces alkali nuclides like ^{39,41}K, ^{85,87}Rb, and ^{133}Cs. Behind the RFQ, a laser ion source for the production of carbon cluster bunches is placed. Both sources are perpendicular oriented to the beam line. The ions of both sources are guided into the beam line with 90° deflector systems. The surface ion source (Fig. 4.7 (a)), has a pellet holder with an alkali pellet which is heated by a current. The surface of the hot pellet is continuously evaporating alkali ions, which are accelerated in a electric gradient and transported through a system of lenses and steerers to the beam line. The continuous alkali ion beam is further injected into the RFQ buncher, and continues the same way as the ion beam from the ISOLDE facility.

The laser ion source [Boe09], [MKB$^+$04] is producing carbon clusters from a pellet (Fig. 4.7 (b)). A frequency doubled Nd:YAG laser is shooting on the pellet through a view port from outside. A bunch of charged clusters with different sizes is formed in a formation chamber due to a laser induced plasma. The clusters are accelerated and transported to the beam line via einzel lenses and deflectors [Boe09], [MKB$^+$04]. The present measurements have been performed exclusively with ^{133}Cs$^+$ ions from the surface ion source.

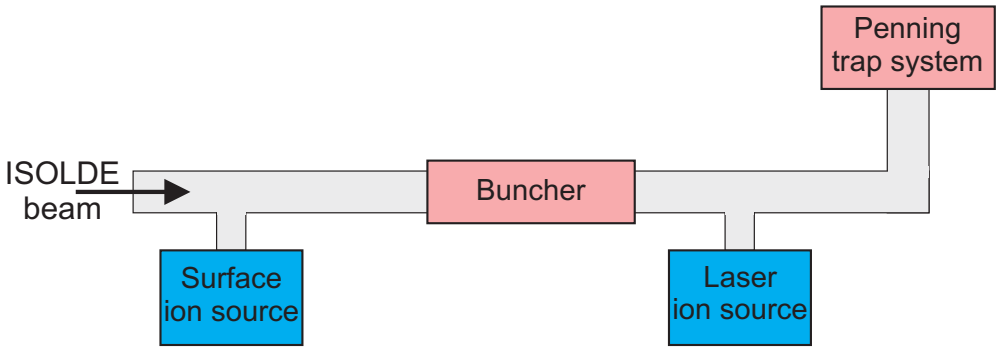

Figure 4.6: Schematic sketch of the ISOLTRAP beam line with the reference ion sources which are assembled perpendicular to the beam line. The surface ion source produces a continuous beam of alkali ions and the cluster source produces discrete ion bunches of carbon clusters.

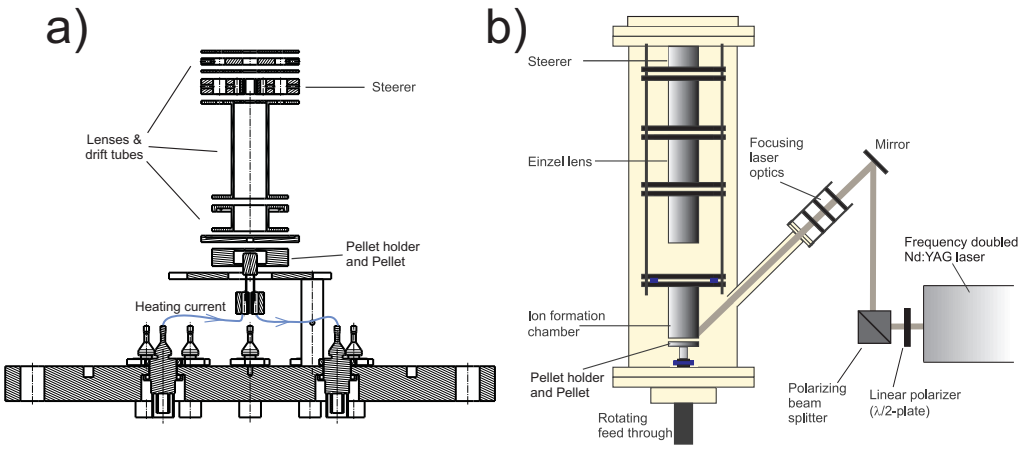

Figure 4.7: Sketch of the reference ion sources at ISOLTRAP. (a): Surface source with a heated pellet of alkali elements. (b): Carbon cluster source with a Nd:YAG laser which is shooting on a carbon pellet [Boe09]. Both sources have lenses and deflectors to guide the ions to the beam line.

4.6 Experimental Setup for the Investigation of Excitation Modes in Cooling Processes

All investigations for the present thesis are performed in the Preparation Penning Trap, which is operated with $^{133}Cs^{+}$ ions from the alkali source. The Preparation Penning Trap, which is loaded with the ion bunch from the RFQ buncher, is used with an MCP detector which is located on a linear feedthrough (Fig. 4.8). Three turbo molecular pumps are pumping this section. The pressure readout is located above the trap region at circa one meter distance from the trap center. The pressure at the readout is in the order of 10^{-7} mbar to 10^{-6} mbar, whereby in the trap a pressure in the order of 10^{-5} mbar to 10^{-4} mbar is assumed [Bec93]. The detector on a linear feedthrough can be replaced by a drift tube to transfer the ions to the Precision Penning Trap.
After the ejection of the cooled ions, the ToF duration from the Preparation Penning Trap to the detector is 57.5 μs. The counted events are added in a ToF spectrum, where the total number of events is evaluated. An example for a ToF spectrum of cooled ions is shown in Fig. 4.9. The typical width of the ToF peak is 1.0 μs. The transfer of the ions is optimized such that all ions hit the detector surface. The alkali source, the RFQ, and the transfer section between the RFQ buncher and the Preparation Penning Trap are not further investigated and can be regarded as a combined ion source.

4.7 Procedure and Time Structure for the Measurement of Cooling Resonances

Most of the measurements are performed in order to record cooling resonances with a QES or with an OES. A cooling resonance is the application of the buffer gas cooling

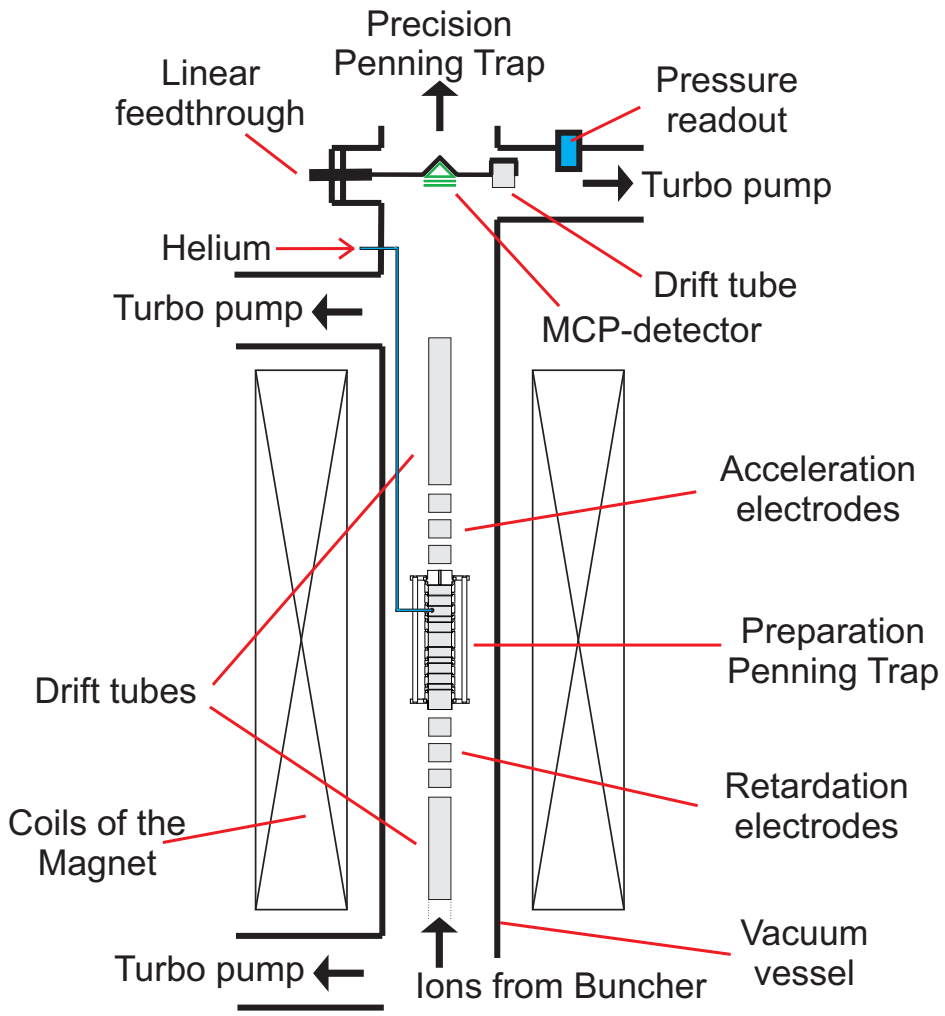

Figure 4.8: ISOLTRAP section with the Preparation Penning Trap and a MCP detector (not to scale). Retardation electrodes are located in front of the trap, for a slow injection of the ions. Behind the trap the ions are accelerated, pass a drift tube, and hit the detector.

technique with frequencies in the vicinity of ν_c for a QES and $2\nu_c$ for an OES. If the excitation frequency is close to the resonance frequency, the ions are centered and reach the detector. The larger the distance to the resonance frequency, the less ions can be detected.

The characterization of a cooling process includes information about the resolving power, the cooling efficiency $N_{\mathrm{ion}}/(\mathrm{ion\,counts})$, and the quality of the ion cooling (see 5.4) and centering, which can be estimated by the energy distribution and also by the efficiency, since a loss of ions includes a broad spacial distribution of ions in the trap. In every experimental cycle, a pre-cooling process with a quadrupolar excitation ($\nu_{\mathrm{exc}} = \nu_c$) is applied, which results in a centering of all ions in advance and reduces the bunch width

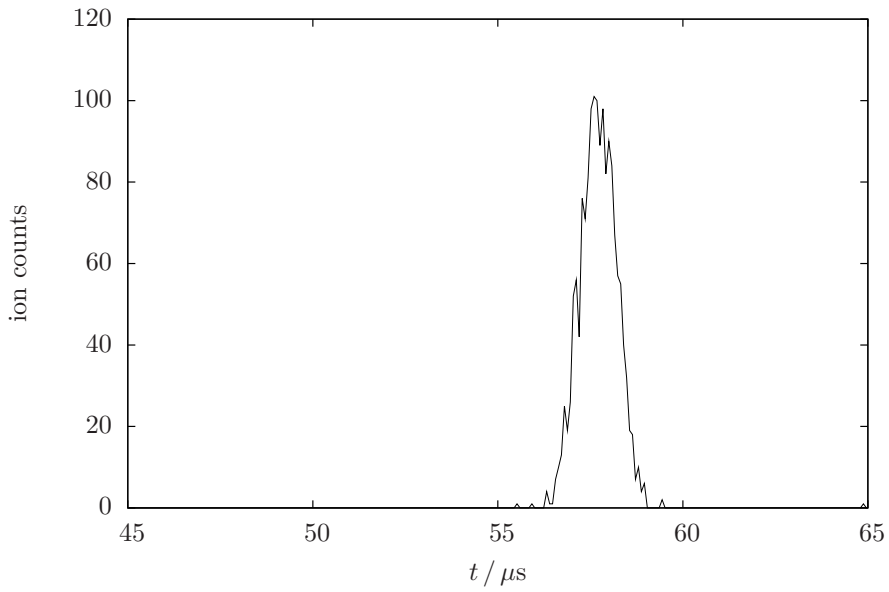

Figure 4.9: Counted events as a function of the time of flight of the ions to the detector behind the Preparation Penning Trap.

and thus the distribution of the initial conditions from the ion transfer. Another advantage of the pre-cooling is, that with an ejection of such prepared ions, it is possible to measure the total number of available ions for the determination of the efficiency in the later cooling process. With the measurement of total ions for every resonance measurement in advance, also the yield of the alkali source is monitored. Thus the influence of source instabilities is compensated.
A resonance measurement starts with the determination of the maximal ion count rate with 10 experimental cycles where 150 to 300 ions are averaged over the cycles. Then follows a rough search for a frequency window around ν_c for the QES or $2\nu_c$ for the OES, in order that the recorded resonance curve fills the window. The frequency is scanned in minimum 30 equal steps, where for every frequency step minimum 10 experimental cycles are performed which includes that at least 100 ions are collected at the resonance frequency. In the following, the excitation which is applied to perform the cooling process is called main excitation. The time structure of an experimental cycle is illustrated in Fig. 4.10. When the buncher delivers the ions, a capture pulse is triggering the lower endcap to change the potential of endcap A from 100 V to ground potential for 30μs to load the trap. A waiting time is implemented to cool the axial oscillations of the ion motion. After that, a quadrupolar excitation is applied to center all ions radially as a pre-cooling. A waiting time for radial cooling is afterwards implemented to decrease the remaining reduced cyclotron radius after the conversion. Then the ions are increased in their magnetron radius by a dipolar excitation for 20 ms, and the main excitation is applied for 50 ms, 100 ms, or in one of the measurements up to 1 s. Afterwards, a second radial-cooling waiting time is added. An extraction pulse ejects the centered

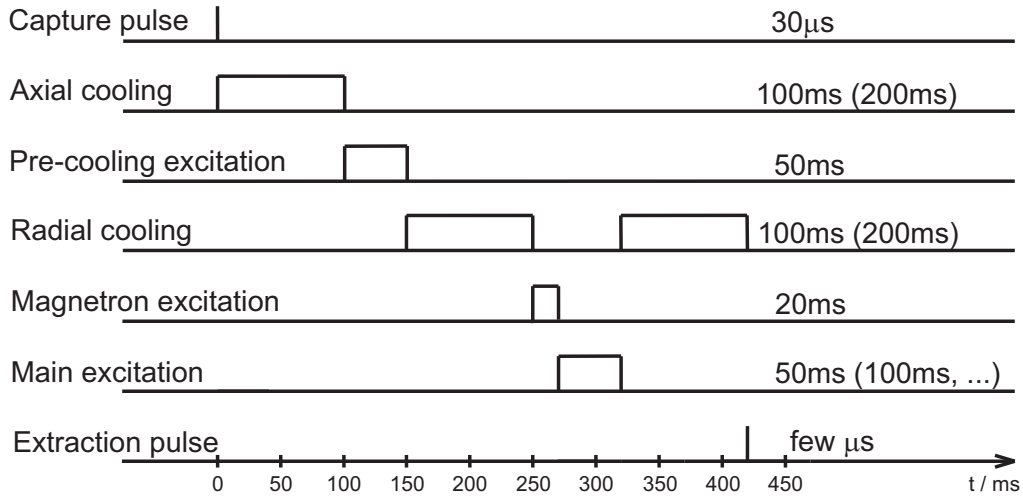

Figure 4.10: Time structure of an experimental cycle in a cooling resonance measurement.

ions towards the detector.

4.8 Application of Excitation schemes

To abbreviate the names of the circular polarized excitation schemes, the circular polarized dipolar excitation scheme is called CPDES, and the standard linear dipolar excitation scheme is called LPDES. In the same way, the circular and linear quadupolar excitation scheme are called CPQES and LPQES, respectively. In order to realize the application of different excitation schemes, several devices has been used which are listed in Tab. 4.2. Beside the measurements of cooling resonances, a comparison of the LPDES and the CPDES was performed. The setup for the test of a CPDES is shown in Fig. 4.11. A frequency generator with two phase-locked outputs [AM300] produces a sine and a cosine function to realize a phase difference of 90° between the two signals. These signals are applied to perpendicular pairs of electrodes, with one signal per pair inverted. For this reason four linear fan-in-fan-out channels were needed. Since this modules have a small attenuation effect, also the not-inverted signals are applied via fan-in-fan-out channels to avoid asymmetries. The configuration of the signals has been investigated by performing a Fourier analysis of the radial multipoles [BMSS90], [BBB+08]

$$F(n) = \sum_{n=0}^{\infty} \left(\frac{1}{2\pi} \int_0^{2\pi} \Phi(\varphi) \cdot e^{\mathrm{i}n\cdot\varphi} d\varphi \right) \cdot e^{\mathrm{i}n\cdot\varphi} \cdot U_{\mathrm{exc}} \cdot \left(\frac{\rho}{\rho_0} \right)^n , \tag{4.6}$$

with $\Phi(\varphi)$ as the azimuthal potential and U_{exc} as the excitation amplitude. This results in a dipolar term as the main component. Higher terms are neglected since the characteristic resonance frequencies are in higher orders of magnitude, and the influence close

Table 4.2: List of devices which have been used for the application of excitation schemes. First column: Type of the device. Second column: Name of the device. Third Column: Manufacturer of the device. Fourth column: Special features of the device.

Type	Name	Manufacturer	Features
Frequency Generator	DS345	SRS	Burst mode compatible
Frequency Generator	33250A	Agiland	Burst mode compatible
Frequency Generator	AM300	Rhode und Schwarz	Burst mode compatible, Two phase-locked outputs
Radio Frequency Amplifier	KL-500	RM Italy	-
Linear fan-in/fan-out	428F	LeCroi	Phase inverter

to the center of the trap is weak, since the field is decreasing radially, dependent on the order of the multipole field $|\vec{E}_n| \propto \left(\frac{\rho}{\rho_0}\right)^{n-1}$ [BMSS90], [BBB$^+$08]. The quadrupolar excitation for the pre-cooling is applied with just one signal phase on two opposite electrodes, whereas the other electrodes are grounded during the excitation. This results in a monopole term and a quadrupole term, oscillating with the frequency ν_c. A monopole term causes an axial parametric excitation, but the influence is negligible because the frequency is far away from ν_z. After the pre-cooling process, the ions are excited until the magnetron radius is larger than ρ_D and the ions are not detected. For the comparison with a linearly polarized dipolar excitation, the second output of the frequency generator is switched to 0 V.
To obtain a cooling resonance, three frequency generators are used in order to perform a pre-cooling excitation, a magnetron excitation, and the main excitation. To test the CPQES, the allocation is more complicated since more phase inverters are necessary as shown in Fig. 4.12. Eight linear fan-in-fan-out channels are used, which can be switched to invert the signal. For the comparison with a linear quadrupolar excitation scheme, the second output is switched to 0 V. Note that with this symmetric allocation for the trap segments, the monopole term in the CPQES and the LPQES vanishes automatically. With this configuration of the fan-in-fan-out channels it is not possible to apply a symmetric magnetron excitation. The signal is applied to a single electrode, which results in a monopole, a dipole, a quadrupole, and higher moltipoles. The magnetron frequency is low as compared with ν_z for an axial excitation, or as compared with ν_c and the resonance frequencies of higher radial multipoles, so that disturbing effects as a loss of ions are not observed.

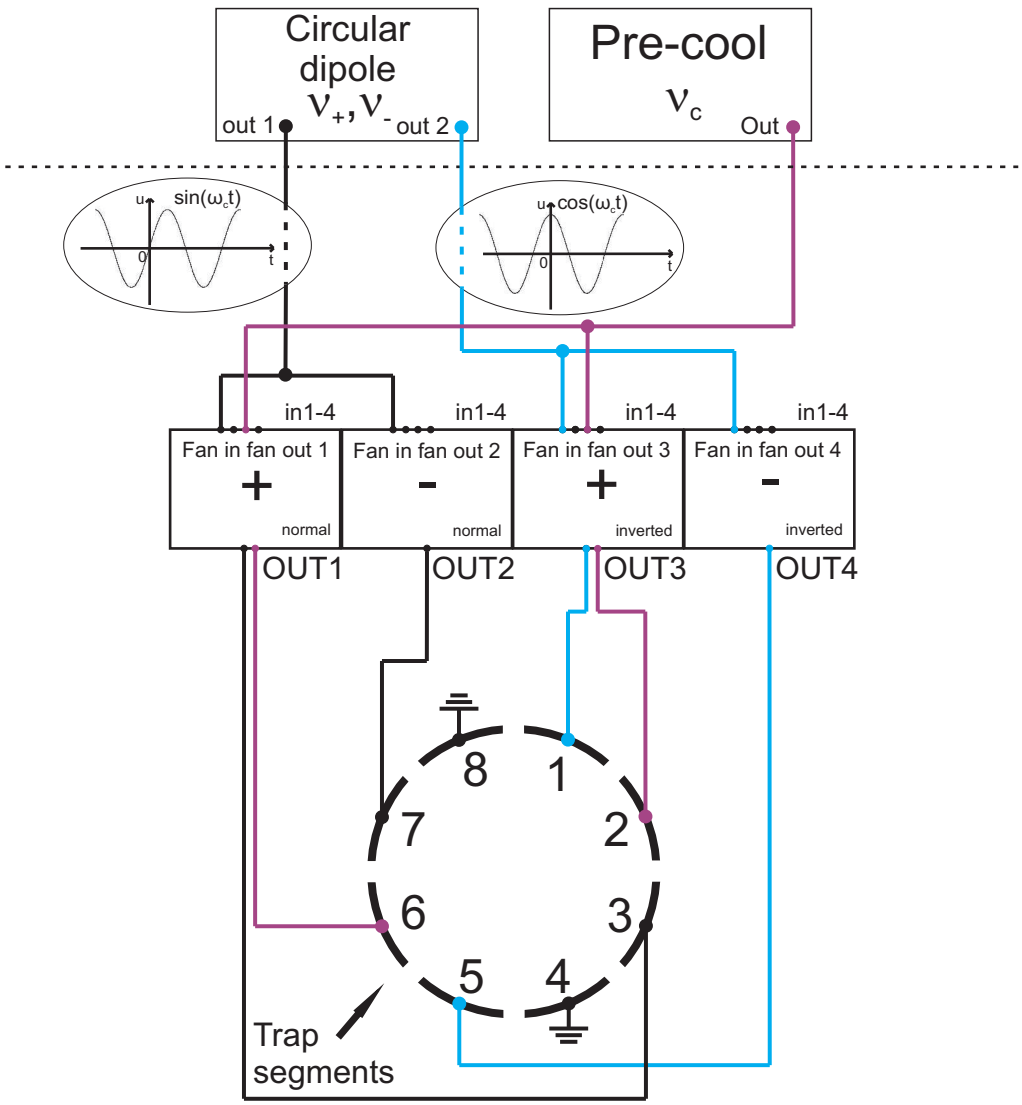

Figure 4.11: Sketch of the ring segment allocation for the test of the circularly polarized dipolar excitation scheme.

For the measurement with octupolar excitation, the allocation of the segments is performed as in Fig. 4.13. The octupole signal has to be amplified because the field in the center region of the trap is weak $E_{\mathrm{oct}} \propto \left(\frac{\rho}{\rho_0}\right)^3$. An allocation of all eight electrodes with the octupolar signal also requieres fan-in-fan-out modules to couple into the pre-cooling signal and the magnetron excitation. The usage of such modules is not possible for the OES, since the required voltages would exceed the limits of the modules. Thus, four segments are used which results in a monopole term, an octupole term and negligible

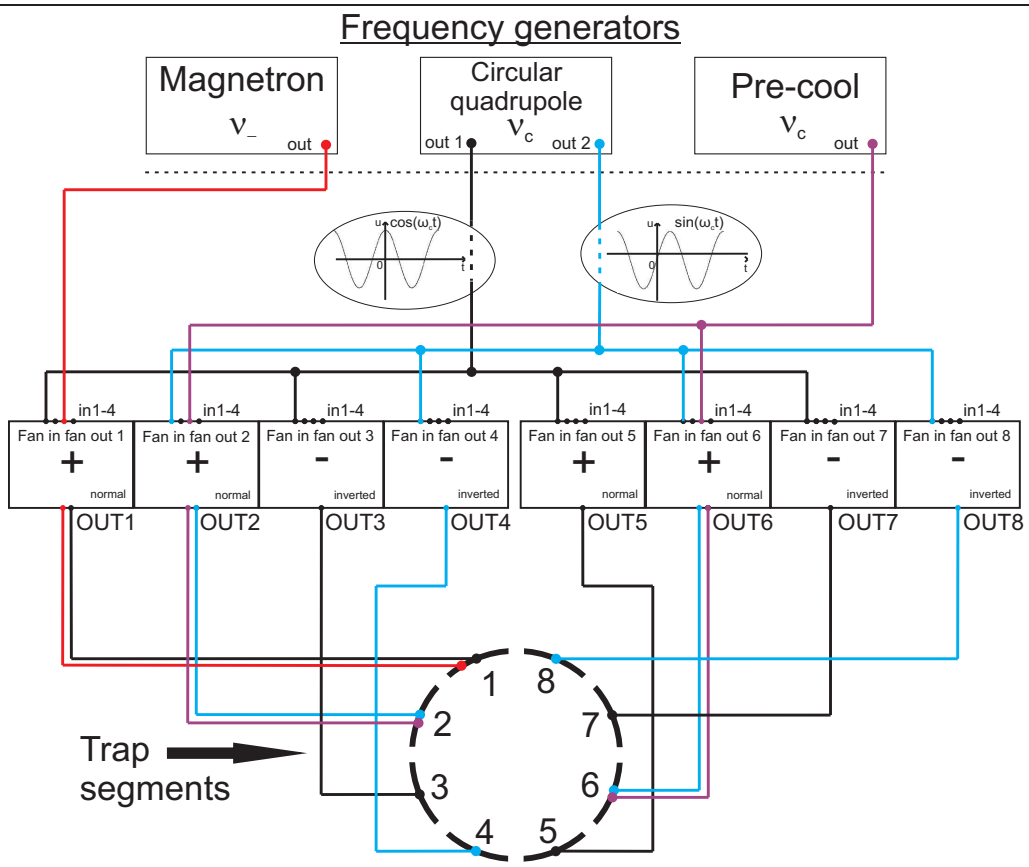

Figure 4.12: Sketch of the ring segment allocation for the test of the circularly polarized quadrupolar excitation scheme.

terms of higher orders. In order to perform a fast and convenient switching to the QES for the comparison, the amplifier is by-passed, the frequency changed, and one pair of opposite electrodes is grounded. This results in the same scheme as the pre-cooling excitation. The magnetron excitation is applied on a single segment as for the circuit for the CPQES.

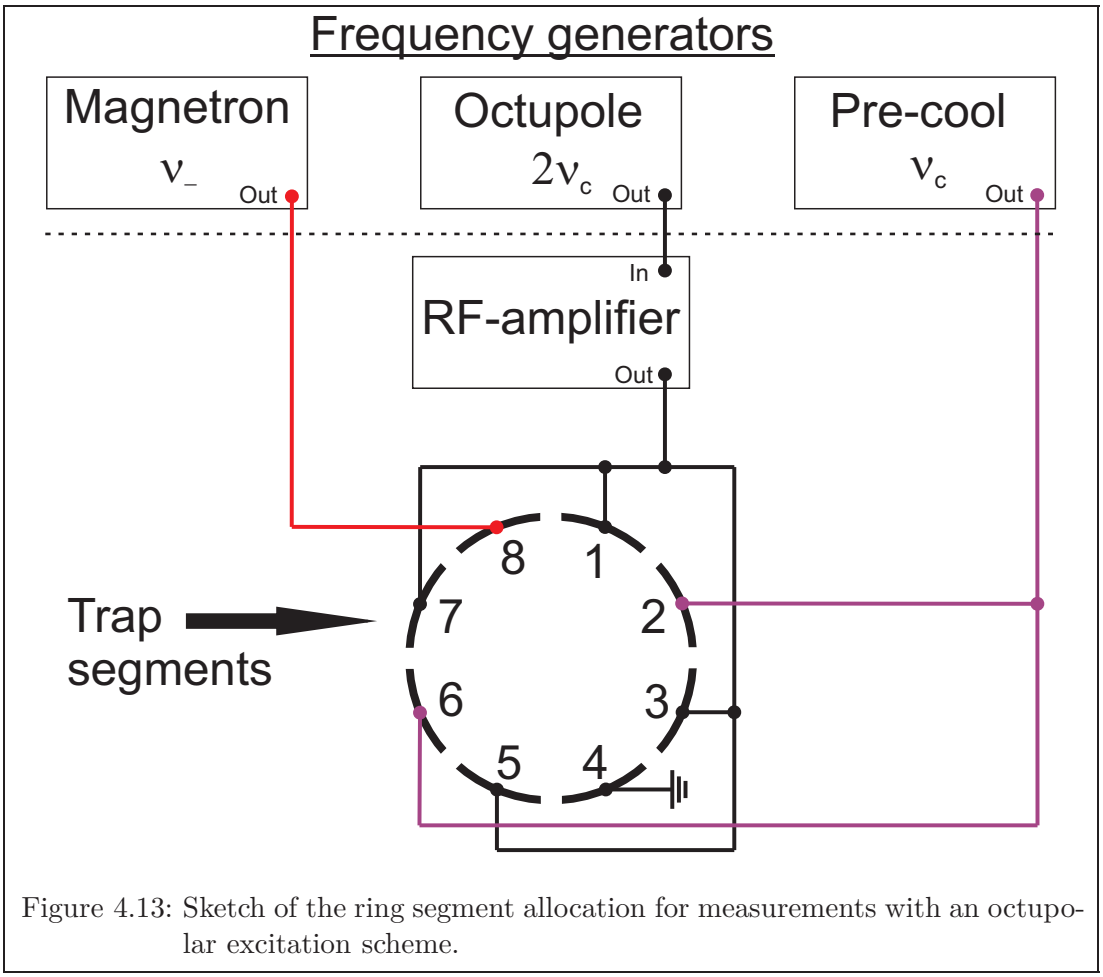

Figure 4.13: Sketch of the ring segment allocation for measurements with an octupolar excitation scheme.

5 Measurements and Discussion

In the following, the experimental results are presented. This includes a test for the circularly polarized dipolar and quadrupolar excitation scheme, and the investigation and comparison of an OES and a QES.

5.1 Investigation of Circularly Polarized Excitation Schemes

5.1.1 Confirmation of the Predictions for the CPDES

In 2.3.2 it was predicted that the radius of the eigenmotion which is excited resonantly is doubled for the CPDES as compared to the LPDES for the same amplitude and excitation time. To compare a CPDES with a LPDES, an amplitude scan is performed to determine the point where the ions leave the center region of the trap. The excitation signal is applied with the frequency $\nu_\mathrm{d} = 301\,\mathrm{Hz}$, the magnetron frequency ν_- of $^{133}Cs^+$ ions in the Preparation Penning Trap, and with a duration of 20 ms. The signals are applied as shown in Fig. 4.11 in 4.8. The result of the amplitude scan of both dipolar excitation schemes is shown in Fig. 5.1. The data points are fitted with the logistic function, which produces an adequate approximation

$$y = \frac{A_1 - A_2}{1 + (x/x_0)^\beta} + A_2. \tag{5.1}$$

The variables A_1,A_2,β, and x_0 are the fit parameters. The parameters A_1 and A_2 determine the difference between the lower and the upper limit of the curve, where A_2 is the offset of the lower limit. The parameter β determines the growth rate of the function. In the present case $A_2 = 0$, thus $y = A_1/2$ for $x = x_0$. The amplitudes, for which half of the ions are lost, have the ratio $21.0 \pm 1.0\,\mathrm{mV}/41.6 \pm 2.5\,\mathrm{mV} = 0.505 \pm 0.04 \approx \frac{1}{2}$, which confirms the predictions from 2.3.1 and 2.3.2 with a deviation below 2 %. To measure the ratio more precisely, the setup with the Preparation Penning Trap is not adequate, since the ions are distributed in space and buffer-gas effects are disturbing the motion. In addition the radii of the ions can not be determined precisely since a counting of events at the detector does not give enough information about the position. Note that the oscillations for the increasing of the radius with a LPDES as shown in Fig. 2.3 in 2.3.1 can not be measured as well. For these purposes, FTICR (Fourier-transform ICR) methods [Com78] could be used.
Furthermore it was predicted that the radius of the ion is not increasing if the rotational direction of the CPDES is opposite to the motion of the ion. In order to confirm this prediction, the amplitude was set to a value where no ions were detected for the correct rotational direction of the field. Afterwards, the rotational direction has been changed and the ions did not leave the center region and have thus been detected.

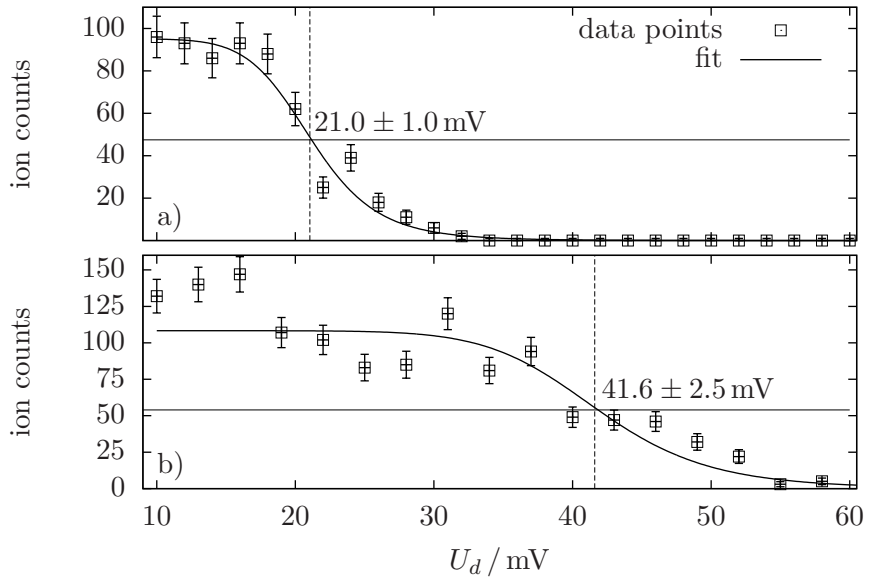

Figure 5.1: Ion counts as a function of the excitation amplitude U_d for a CPDES (a) and for a LPDES (b).

5.1.2 Confirmations of the Predictions for the CPQES

In order to confirm that the beating frequency ν_B of a CPQES is two times that of a LPQES for the same amplitude, an amplitude scan of U_q for a fixed T_exc, or a scan of T_exc for a fixed amplitude can be performed. It is chosen not to scan the excitation duration, because collisions with the buffer gas atoms are accumulating with the time, thus an amplitude scan is performed. The used electrode configuration at the ring segments is shown in Fig. 4.12 in 4.8. If the excitation amplitude is large enough to perform a conversion, the ions are centered and detected. A halved required amplitude for the CPQES compared to a LPQES leads directly to the doubled ν_B for the CPQES if the chosen amplitudes are equal for both excitation schemes, since $\nu_\mathrm{B} \propto U_\mathrm{q}$. The excitation time T_exc is 100 ms and the excitation frequency $\nu_\mathrm{q} = 547753\,\mathrm{Hz}$, which has been determined by cooling resonances in advance. The pressure is chosen low with $7 \cdot 10^{-7}$mbar at the Penning gauge, to reduce collisional effects, whereas the pressure for the normal procedure with the ISOLDE beam is between $1.2 \cdot 10^{-6}$mbar and $1.7 \cdot 10^{-6}$mbar. The result of the amplitude scans is illustrated in Fig. 5.2. The ratio of the amplitudes which center half of the ions is $170 \pm 2.5\,\mathrm{mV} / 342 \pm 5.0\,\mathrm{mV} = 0.497 \pm 0.01 \approx \frac{1}{2}$, which confirms the expectations with a deviation below 1%.
The analytical solutions in 2.3.3 and 2.3.6 predicts furthermore that both excitation schemes are equal, if the amplitude for the CPQES is halved compared to the LPQES. The high frequency effects are neglected. To confirm this, two cooling resonances are

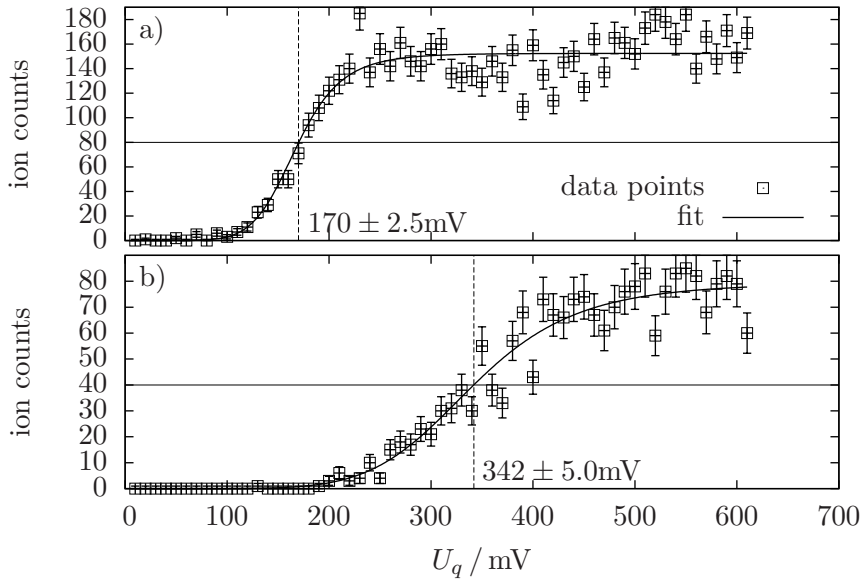

Figure 5.2: Counts of centered ions as a function of the excitation amplitude for a CPQES (a) and for a LPQES (b).

measured with the same conditions. The excitation time is chosen to $T_{\mathrm{exc}} = 100\,\mathrm{ms}$, and the amplitudes are chosen to 255 mV and 510 mV for the CPQES and the LPQES, respectively. The resulting resonance curves are shown in Fig. 5.3. Both resonances have a resolving power of $R_p = \nu_c/\Delta\nu_{\mathrm{H}} \approx 5,21 \cdot 10^4$ with an uncertainty of about 6%. The errorbars in Fig. 5.3 illustrate the statistical error $\sqrt{(\mathrm{ion\,counts})}$, where the error for the FWHM is determined from the Gaussian fit with the respective uncertainties.
The last aspect which has been investigated is that the conversions are not performed if the excitation field is rotating against the motion of the ions. Therefore the cables at the outputs of the frequency generator have been exchanged, with the result that no ions were centered.

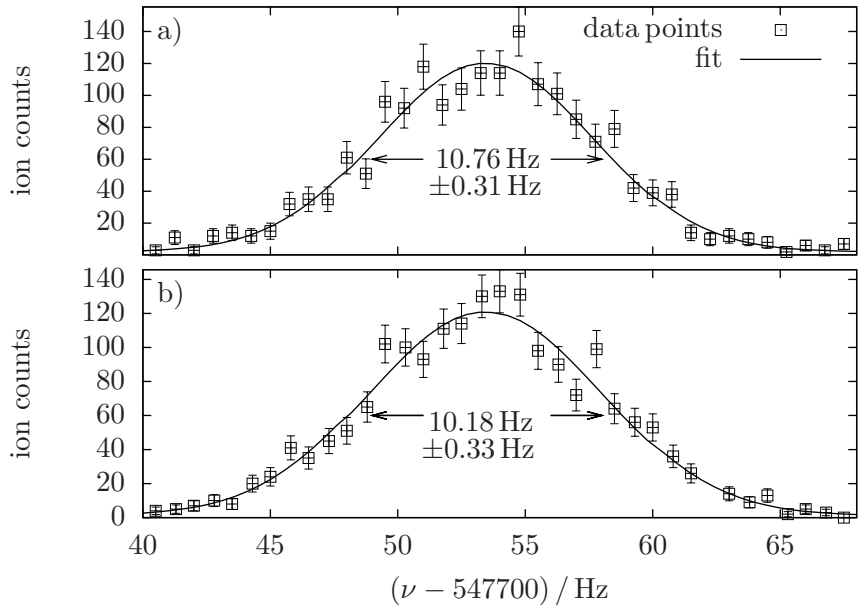

Figure 5.3: Ion counts as a function of the frequency from cooling resonances in a LPQES (a) and a CPQES (b). The solid lines are a Gaussian fit to the measured data.

5.2 Test of the Ion cooling with Octupolar Excitation

The series of experiments with respect to the OES was started with an amplitude scan in order to test the ion centering at $2\nu_c \approx \nu_{\mathrm{oct}} = 1095508\,\mathrm{Hz}$. The used electrode configuration is shown in Fig. 4.13 in 4.8. The pressure was set to $1.2 \cdot 10^{-6}\,\mathrm{mbar}$ as for the standard QES procedure and the main excitation time $T_{\mathrm{exc}} = 50\,\mathrm{ms}$. The axial and the radial cooling time was 100 ms, and the pre-cooling time 50 ms. The result is shown in Fig. 5.4 (a). For an excitation amplitude of 8 V, the growth of the curve exceeds, whereby it is assumed to be that $U_{\mathrm{oct}}/U_{\mathrm{B}} = 1$ for the mean of the ions. For this amplitude, a cooling resonance is recorded as shown in Fig. 5.4 (b). The shape of the resonance is close to a Gaussian distribution as in a QES (see Fig. 5.3).

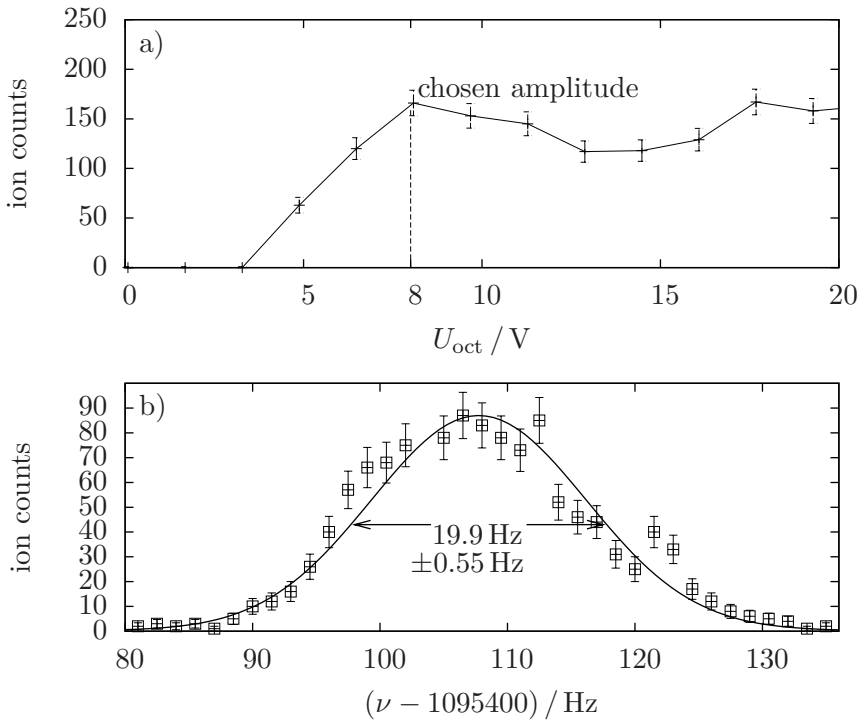

Figure 5.4: (a) Ion counts as a function of U_{oct} for an OES with the frequency 1095508 Hz. The points are connected with straight lines to guide the eye. (b) Ion counts as a function of the frequency for $U_{\mathrm{oct}} =$ 8 V. The solid line in part (b) is a Gaussian fit to the data.

The narrow resonance shapes from the single ion simulations (see 2.5.2) are not reproduced in a buffer gas environment as already predicted from the obtained resolving powers in the simulations with elastic collisions in 3. The uncertainties of the initial conditions in radius and phase and the buffer-gas collisions lead to a mixing of different resonance shapes, which results in an averaged shape as assumed in 3.4.2. The resolving power is determined with $R_p = 2\nu_c/\Delta\nu_{\mathrm{H}} = 5.51(15) \cdot 10^4$. This is in the same range as the resolving power from the QES in Fig. 5.3, whereas the resolving powers can not be compared directly, since the applied pressures are not equal.

5.3 Discussion of OES and QES in cooling processes

The aim is to characterize the OES for different experimental parameters for the cooling process and to compare the quality with the standard QES for the applicability in mass measurements. Therefore their properties are investigated via cooling resonances for different excitation amplitudes, pressures, and excitation times, whereby the efficiency is always monitored via a direct ejection of the ions after the pre-cooling process. The measurements which have been performed for an excitation time of 50 ms are compared with the simulations with elastic collisions in 3.4.4.

5.3.1 Amplitude Scans with the Resonance Frequency

The first investigation for the characterization of both schemes is performed by amplitude scans for different pressures. For this, the pre-cooled ions are moved to larger magnetron radii with an excitation at the frequency ν_- for 20ms and an amplitude of 1.2 V and afterwards excited at ν_c for a QES and at $2\nu_c$ for an OES. Four amplitude scans for a QES with 50 ms duration of the main excitation are recorded as shown in Fig. 5.5. To compare the results also with the collision simulation, 2-D cuts from the efficiency plots in 3.4.4 are added in the diagrams. The amplitude has been fitted to the measured data via the visible conversions in Fig. 5.5 (a) and (b). The best agreement which is found for (a) and (b) has been used also for (c) and (d). Since the pressure inside the Preparation Penning Trap is not known, the measured shapes in Fig. 5.5 are compared with the simulated shapes for different pressures, where the ratio of the measured pressures to the lowest pressure p/p_0 in the simulation is the same as in the experiment ($3.0 \cdot 10^{-7}$ mbar $= p_0$, $6.0 \cdot 10^{-7}$ mbar $= 2p_0$, $1.2 \cdot 10^{-6}$ mbar $= 4p_0$, $1.7 \cdot 10^{-6}$ mbar $= 5.7p_0$). The best agreement is found for $p_0 = 2.4 \cdot 10^{-5}$ mbar in the simulation (Tab. 5.1). Note that the pressures at the Penning gauge in the experiment can not be replaced by the simulated pressures, since the model does not include an individual derivation of scattering angles, or partial pressures of other elements than helium.
In (a) and (b), the experimental pressures are chosen so that several full conversions with radii larger than ρ_D are performed. Thus for ($U_\mathrm{q}/U_\mathrm{B} = 1, 3, ...$) the ions are centered, and they are absent for ($U_\mathrm{q}/U_\mathrm{B} = 2, 4, ...$). For higher pressures as in part c) and d), the radius is decreased to $\rho < \rho_\mathrm{D}$ within the excitation time, and the oscillation of the ion counts is vanishing. The maximal measured efficiency is written in the diagrams,

Table 5.1: Simulated pressures with the best approximation of the experimental results (see text). First column: Pressure at Penning gauge. Second column: Pressure in the simulation. Third column: Ratio of pressures to lowest pressure.

p / mbar (experiment)	p / mbar (simulation)	ratio p/p_0
$3 \cdot 10^{-7}$	$2.4 \cdot 10^{-5}$	1
$6 \cdot 10^{-7}$	$4.8 \cdot 10^{-5}$	2
$1.2 \cdot 10^{-6}$	$9.6 \cdot 10^{-5}$	4
$1.7 \cdot 10^{-6}$	$1.38 \cdot 10^{-4}$	5.7

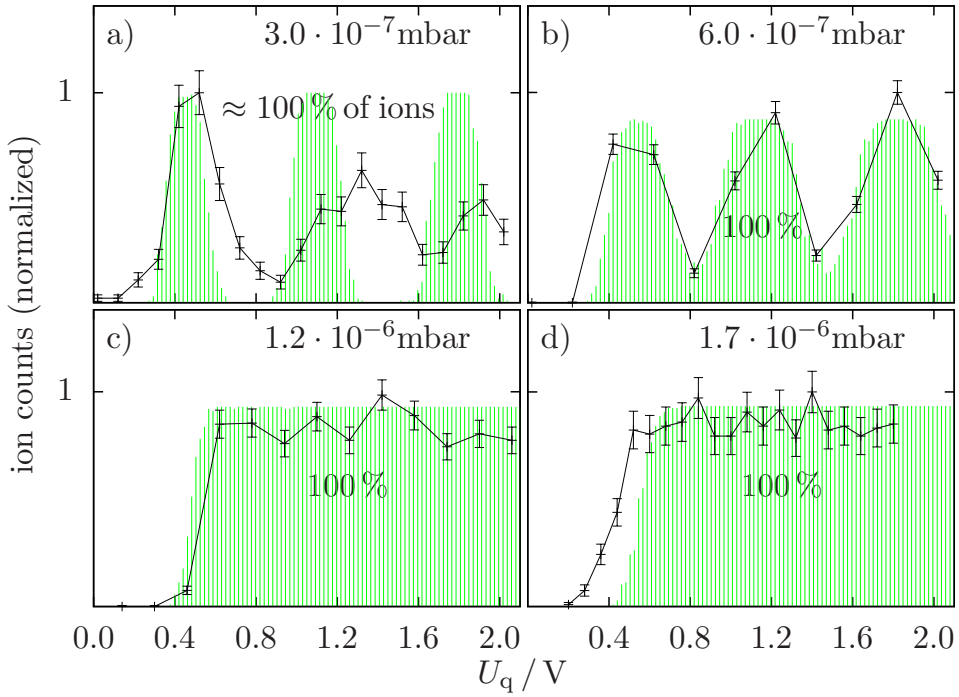

Figure 5.5: Normalized ion counts as a function of the excitation amplitude for a QES at several pressures ((a): $3.0 \cdot 10^{-7}$ mbar, (b): $6.0 \cdot 10^{-7}$ mbar, (c): $1.2 \cdot 10^{-6}$ mbar, (d): $1.7 \cdot 10^{-6}$ mbar). The measured points are connected with straight lines for a better overview. The results from the simulation in 3.4.4 are added with green bars.

where for the QES it is 100 % for all pressures in the experiment and simulations for correct amplitudes. The number of ion counts from the simulation in the diagrams N_{sim} is extrapolated via the maximum of the measured ion counts $N_{\mathrm{max,exp}}$ and the measured efficiency

$$N_{\mathrm{sim}} = N_{\mathrm{max,exp}} \cdot \frac{1}{\mathrm{efficiency}}. \tag{5.2}$$

In Fig. 5.5 (b), (c) and (d), the simulated values provide a sufficient approximation to the measured data. For the pressure which is chosen for (a), the measured ion counts for the second and third centering of the ions is decreased. Such an effect is not predicted from the simplified model in the simulation. Broader initial energy distributions or heavier neutral collision partners for example, have not been implemented in the simulation. The higher partial pressure of other collision partners at a low helium rate, e.g. nitrogen, oxygen, or water could be the reason for a stronger disturbance of the conversion of the radii and leads to an incomplete centering. It is assumed, that a disturbance by collisions in the beginning is propagated by further collisions with heavier partners. A

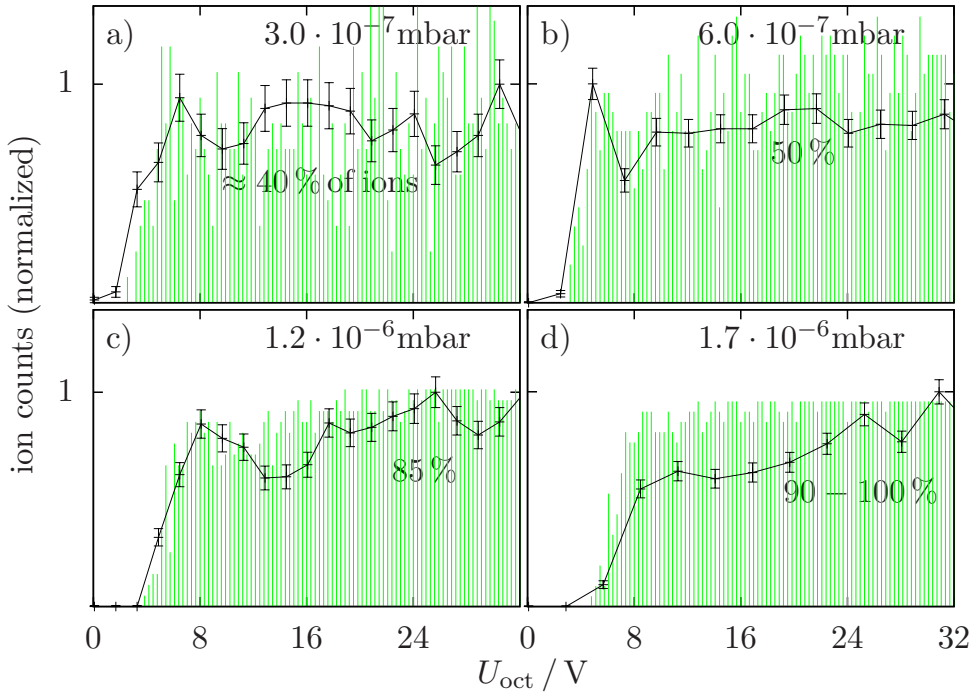

Figure 5.6: Normalized ion counts as a function of the excitation amplitude for an OES at several pressures ((a): $3.0 \cdot 10^{-7}$ mbar, (b): $6.0 \cdot 10^{-7}$ mbar, (c): $1.2 \cdot 10^{-6}$ mbar, (d): $1.7 \cdot 10^{-6}$ mbar). The measured points are connected with straight lines for a better overview. The results from the simulation are added with green bars.

large initial energy distribution in addition could be the case if the applicability of the pre-cooling is limited for lower pressures as $3.0 \cdot 10^{-7}$ mbar (see 5.4). The shapes of amplitude scans in an OES differs from those of the QES as shown in Fig. 5.6. The main differences to the results from the QES is a vanishing of oscillations for the counts at pressures as in (a) and (b), and a decreased efficiency. The shapes from the simulations differ partly from those of the measurement, nevertheless they reproduce the measured differences to the QES, and the mean of the simulated efficiency as $\approx 40\,\%$ in Fig. 5.6 (a) or $\approx 50\,\%$ in (b) is sufficiently approximating the measured results. The low efficiency is understood as described in Fig. 3.7 and Fig. 3.9 in 3.4.4. The ions enter and leave the center region asynchronously due to the distribution of ν_B, and in addition, they show a random behavior with collisions. To center all ions, one has to increase the excitation time or the pressure. Note that the results of the measurements for the OES differ from the simulation with the continuous model in 3.4.3, where an efficiency of $100\,\%$ is predicted for most of the parameters. For the OES, it is also observed that the counts for larger pressures as in (d) are increasing very slowly with increasing excitation amplitudes and thus it is rather difficult to define a voltage like U_B, but it is aimed

to normalize the conditions for the different pressures. If a maximum exists in the amplitude scan as for Fig. 5.6 (a), (b) or (c), this value is taken for $U_{\mathrm{oct}}/U_{\mathrm{B}} = 1$.

5.3.2 Cooling Resonances as a Function of the Excitation Amplitude at a Pressure of $p = 3.0 \cdot 10^{-7}$ mbar

The single ion resonances in an OES without damping show a much higher resolving power than those of a QES, whereas the simulations with statistical collisions predict comparable values for both schemes in the same order of magnitude. To determine the resolving power, resonances are measured systematically. The resolving power R_p and the efficiency are determined at a pressure of $3.0 \cdot 10^{-7}$ mbar and amplitude steps of about $0.25 \cdot U_{\mathrm{B}}$ as shown in Fig. 5.7, where $U_{\mathrm{B}} = 0.2\,\mathrm{V}$ for the QES and $U_{\mathrm{B}} = 4.8\,\mathrm{V}$ for the OES. The pressure is chosen low with the aim to keep the characteristic effects as oscillations of the counts visible. The measured values for the efficiency are directly comparable with the corresponding amplitude scan in 5.3.1, where an efficiency of 1 in

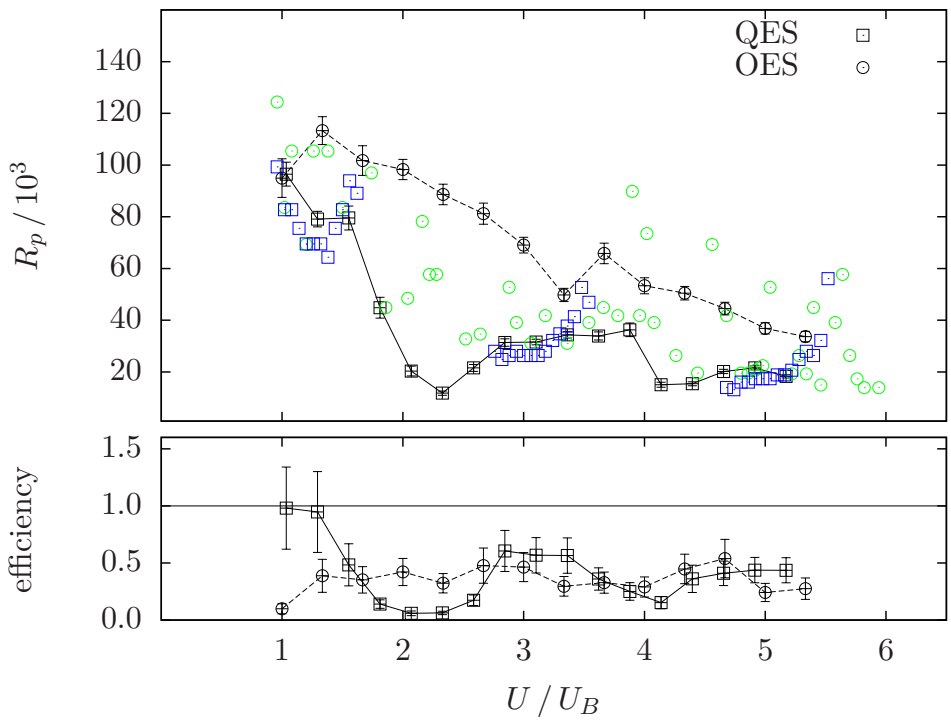

Figure 5.7: Resolving power and efficiency as a function of the normalized amplitude U/U_{B} ($U = U_{\mathrm{q}}$ for the QES or $U = U_{\mathrm{oct}}$ for the OES, respectively) at a pressure of $3.0 \cdot 10^{-7}$mbar at the Penning gauge. The measured points for the OES are illustrated with a circle and those for the QES with a square. The colored points are taken from the simulation with elastic collisions. Blue sqares: QES, green circles: OES.

the diagram means 100% of centered ions. The measured R_p values for the QES are oscillating with the efficiency values, where the highest resolving power $R_p = 9.64(46) \cdot 10^4$ is determined with $U_\mathrm{q}/U_\mathrm{B} = 1$. This behavior is in agreement with the predictions for the quadrupolar resonance shapes (see 2.3.5). The simulations for the QES are reproducing the measured values even quantitatively, regarding the values at the plateaus, whereas the quantity from the simulation is obtained by the choice of the initial radius $\rho_{-,0}/\rho_\mathrm{D}$. The increased values for R_p from the simulated data at the amplitudes, where final magnetron radius of resonant excited ions $\overline{\rho_{-,\mathrm{f}}}$ is close to the diaphragm border, as discussed in 2.4.2, is not visible in the experiment. In the experiment, the wall of the diaphragm is not so perfectly shaped as in the simulations and it is assumed that the ions with $\overline{\rho_{-,\mathrm{f}}} \approx \rho_\mathrm{D}$ are disturbed by image charges and other wall effects, such that they miss the detector or go lost at the walls. Furthermore, the width of the ion cloud in the experiment can be larger than assumed for the simulation at this pressure.
The measured R_p values of maximum $R_p = 1.133(54) \cdot 10^5$ for the OES are up to 1.7 times higher than those of the QES for $U/U_\mathrm{B} = 1, 3, 5$. The shape is roughly linear with just small oscillations, even for this low pressure. The simulated points for the OES are broader distributed around the measured values and alternating, but nevertheless the order of magnitude is reproduced. The comparison of the simulated and the measured data confirms, that a consideration of buffer gas collisions is necessary reproduce the R_p values of the OES in the experiment.

5.3.3 Cooling Resonances for Different Excitation Amplitudes and Pressures

For the comparison of both schemes, a larger number of cooling resonances has been measured, which is a significant cost of experimental time. The results of ≈ 120 resonances are presented as data points in this thesis. Thus, the cooling and waiting times as in Fig. 4.10 in 4.7 for the QES and the OES are adjusted depending on the pressure as shown in Tab. (5.2). The settings for the OES include a longer duration for the preparation and cooling of the ions compared to the QES, since the OES requires well determined initial conditions. Nevertheless the preparation times were not increased further for practical reasons. On the other hand the QES is not so sensitive to the initial conditions and the results are not significantly influenced by this choice of decreased waiting times.
Resonances are recorded systematically for $U/U_\mathrm{B} = 1, 3, 5, 7, 9$ at four different pressures in order to test the applicability of an OES in the beam times. The excitation time was chosen with 100 ms in order to obtain higher efficiencies for the OES, since the radii of the ions have more time to decrease during the excitation. Furthermore 100 ms is a commonly used excitation time. The results for two lower pressures are shown in Fig. 5.8. For the OES, a relatively high resolving power of $2.87(10) \cdot 10^5$ is determined for $U_\mathrm{oct}/U_\mathrm{B} = 1$ and a pressure of $3.0 \cdot 10^{-7}$ mbar at the Penning gauge, where the belonging resonance curve is shown in Fig. 5.9. The loss of ions is more than 50 % also with the used excitation times. For all excitation amplitudes, the widths of the resonances heve been comparable for both schemes. E.g. in the case of $U/U_\mathrm{B} = 1$, the width of the resonances for both schemes has been $\Delta\nu_\mathrm{H} \approx 3.5$ Hz for a pressure of

$3.0 \cdot 10^{-7}$ mbar and $\Delta\nu_{\mathrm{H}} \approx 7.5\,\mathrm{Hz}$ for a pressure of $6.0 \cdot 10^{-7}$ mbar at the Penning gauge.

Table 5.2: Waiting-time (forst column) settings for different pressures (second column), for the QES (third column) and the OES (fourth column).

time	pressure/mbar	QES-time/ms	OES-time/ms
Axial cooling	$3.0 \cdot 10^{-7}$	200	200
	$6.0 \cdot 10^{-7}$	200	200
	$1.2 \cdot 10^{-6}$	100	200
	$1.7 \cdot 10^{-6}$	100	200
Pre-cooling excitation	$3.0 \cdot 10^{-7}$	50	200
	$6.0 \cdot 10^{-7}$	50	200
	$1.2 \cdot 10^{-6}$	50	200
	$1.7 \cdot 10^{-6}$	50	200
Radial cooling	$3.0 \cdot 10^{-7}$	200	150
	$6.0 \cdot 10^{-7}$	200	150
	$1.2 \cdot 10^{-6}$	100	150
	$1.7 \cdot 10^{-6}$	100	150

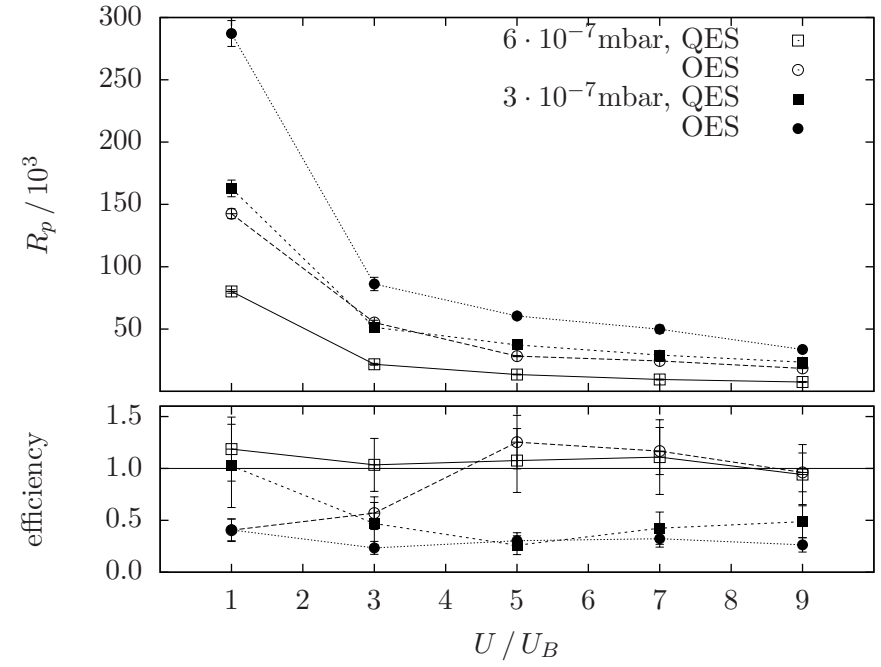

Figure 5.8: Resolving power and efficiency for odd integer of U/U_{B} with a pressure of $6.0 \cdot 10^{-7}$ mbar (open symbols) and $3.0 \cdot 10^{-7}$ mbar (full symbols). The data points are connected with lines to guide the eye.

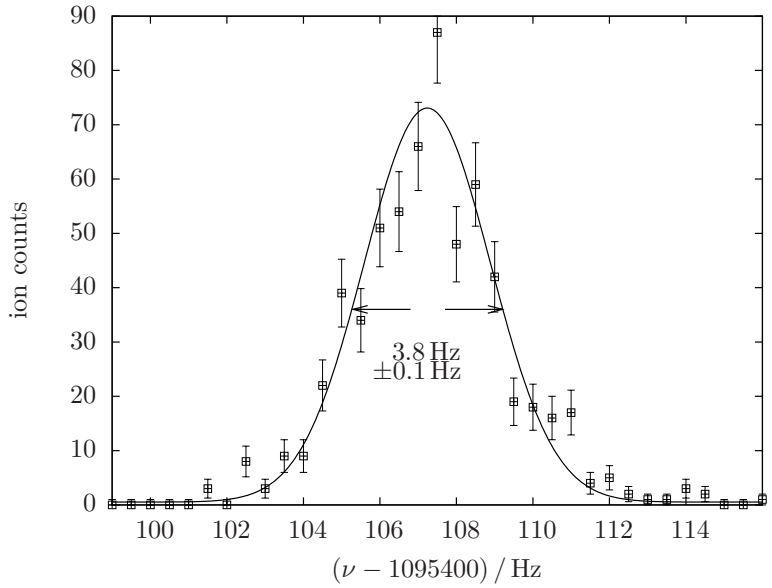

Figure 5.9: Ion counts as a function of the frequency for the OES with a pressure of $p = 3.0 \cdot 10^{-7}$ mbar at the Penning gauge. The solid line is a Gaussian fit to the data.

The doubled resolving power R_p for the OES as compared to the QES is obtained by the doubled excitation frequency $\nu_{\mathrm{exc}} = 2\nu_c$. For higher amplitudes, the R_p values of both schemes are decreasing, but the efficiency for a pressure of $6.0 \cdot 10^{-7}$ mbar is increasing for the OES to the value of the QES. An explanation for the increased efficiency in the OES could be the large distribution of different beating frequencies ν_{B}, since the conversion for many ions, which are less distant to the center can be too slow to be centered for lower excitation amplitudes as $U_{\mathrm{oct}}/U_{\mathrm{B}} = 1, 3$.
The same measurement has been performed for larger pressures as shown in Fig. 5.10. The R_p values for this measurements are smaller, but the quality of centering for the ions at larger pressures is always improved as compared to a lower pressure, which is also reflected by the better efficiencies for the OES which are improved by a factor of 2 for $U_{\mathrm{oct}}/U_{\mathrm{b}} = 3$ as compared to Fig. 5.8. Even for these pressures and $U_{\mathrm{oct}}/U_{\mathrm{B}} = 1$, the efficiency in the OES is not more than 70%. For $U/U_{\mathrm{B}} = 1$ the R_p value for the OES is not reaching the double of that of the QES, which includes furthermore that the resonance widths for the OES are even broader than those of the QES. For all larger amplitudes, the OES shows better properties than the QES.
Nevertheless, also observed for the OES, $U/U_{\mathrm{B}} = 1$ is the only applicable region of excitation amplitudes for the preparation of mass measurements, since the resolving power is the most crucial parameter. There exists only a small amplitude range around $U/U_{\mathrm{B}} = 1$ for each of the investigated pressures to obtain a useful resolving power.

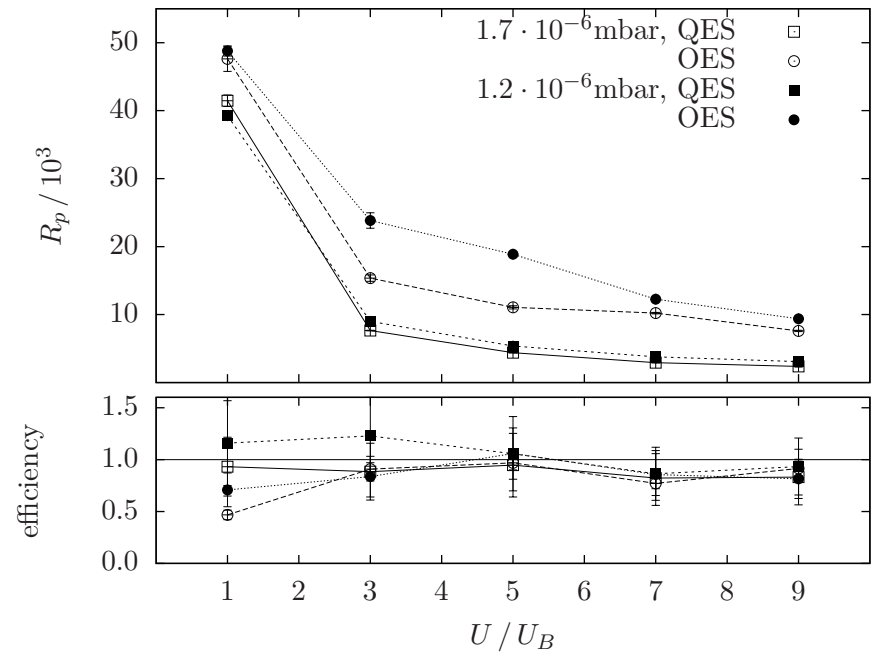

Figure 5.10: Resolving power and efficiency for odd integer of U/U_b with a pressure of $p = 1.7 \cdot 10^{-6}$ mbar (open symbols) and $p = 1.2 \cdot 10^{-6}$ mbar (full symbols). The data points are connected with lines to guide the eye.

5.3.4 Maximal Resolving Power as a Function of the Pressure

For a sufficient cooling of ions, it is always adequate to choose a high pressure inside the trap. In order to investigate the applicability of higher pressures, the maximal R_p value for different pressures and 50ms excitation time is determined for both schemes. The amplitudes are chosen as low as possible around $U/U_\mathrm{B} = 1$ to obtain a high resolving power, therefore the loss of some ions is accepted. A centering of all ions can be performed for high pressures as $2.0 \cdot 10^{-6}$ mbar or higher, but tests have shown, that the R_p values are decreased (see also Fig. 3.8 in 3.4.4). In Fig. 5.11 the maximal R_p values are given as a function of the pressure in the Preparation Penning Trap. For increasing pressures from $5 \cdot 10^{-7}$ mbar to $5 \cdot 10^{-6}$ mbar, R_p drops about an order of magnitude. The R_p values of the OES are approaching those of the QES for $5 \cdot 10^{-6}$ mbar, and thus the advantage of the OES vanishes. Furthermore, a use of the OES with an efficiency of 100 % at high pressures does not result in an adequate resolving power (not plotted here). The simulated data is added in the diagram. The points for the resolving power from the simulation have been averaged for amplitudes in the vicinity of $U/U_\mathrm{B} = 1$ to eliminate the fluctuations for the OES (see Fig. 5.7). The simulated pressures are fitted to the measured pressures as in Tab. 5.1. The higher resolving power of the OES as compared with the QES are reproduced by the simulation, whereas the absolute values

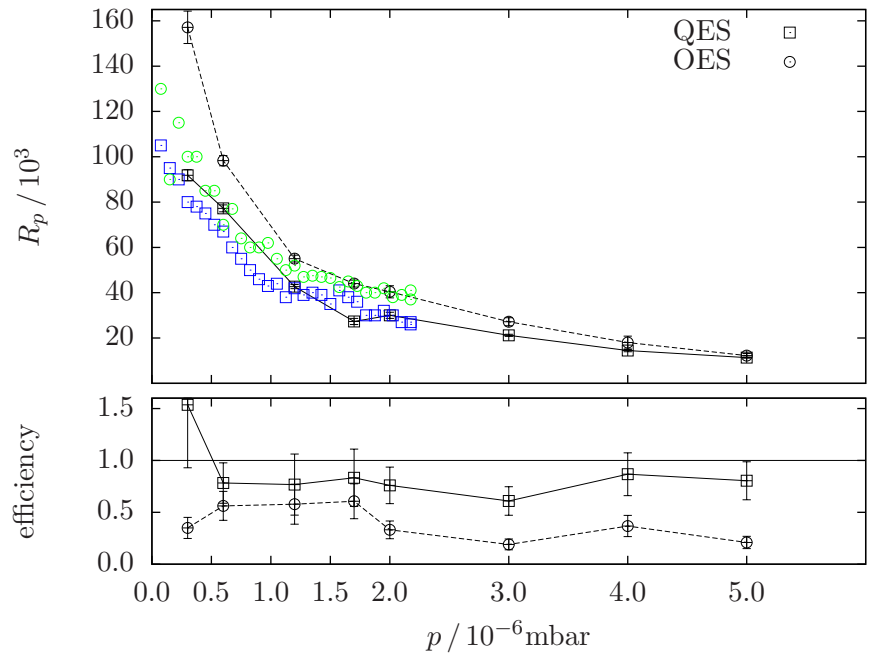

Figure 5.11: Resolving power and efficiency as a function of the pressure for $U/U_\mathrm{B} \leq 1$ and 50ms duration of the excitation. The colored points are taken from the simulation with elastic collisions. Blue sqares: QES, green circles: OES.

for the OES are too small, especially at low pressures. Nevertheless for many points, the simulation gives an adequate approximation of the measured data. For pressures as $p = 3.0,\ 4.0,\ 5.0 \cdot 10^{-6}$ mbar the simulation has not been performed.

5.3.5 Maximal Resolving Power as a Function of the Excitation Time

For the application in the on-line experiment, the QES and OES were tested for long durations of the main excitation. Also for this investigation it is tried to obtain the highest possible resolving power and a loss of some ions is accepted. The excitation times ($T_{\mathrm{exc}} = 20, 50, 100, 200, 500, 750, 1000$ ms) have been used. The results for the QES are illustrated in Fig. 5.12. The R_p values are compared to those of a quadrupolar resonance curve in a vacuum for the magnetron motion $\Delta\nu_{\mathrm{H}} = 0.53/T_{\mathrm{exc}}, R_p = \nu_c \cdot T_{\mathrm{exc}}/0.53$ (see 2.4.2). The R_p values are converging for longer T_{exc} and do not follow the theoretical line. An excitation time longer than 200 ms is not further increasing the resolving power, except for $3.0 \cdot 10^{-7}$ mbar with 500 ms. The maximal resolving power is determined by the pressure. Ions which are not excited in resonance, and thus perform only the partly conversion between the eigenmotions, require a longer time to move to the center, but this time is given by a long duration of the excitation. This effect is compensating the theoretical expected decreased width of the resonance for longer excitation times

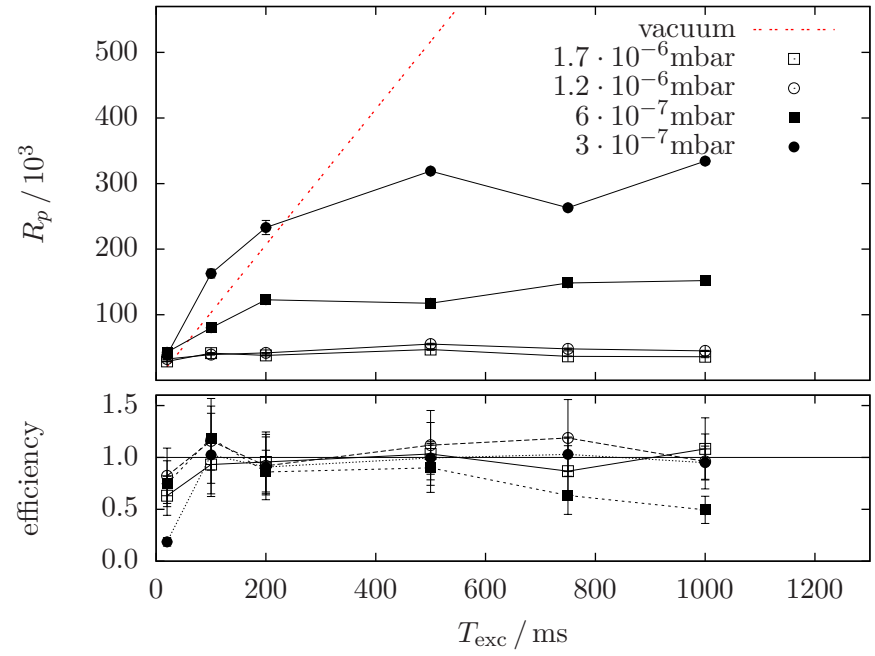

Figure 5.12: Resolving power and efficiency for $U/U_{\mathrm{B}} \leq 1$ as a function of the excitation duration for the QES at different pressures. The red line shows the R_p values for the magnetron motion of a resonance for the QES in a vacuum.

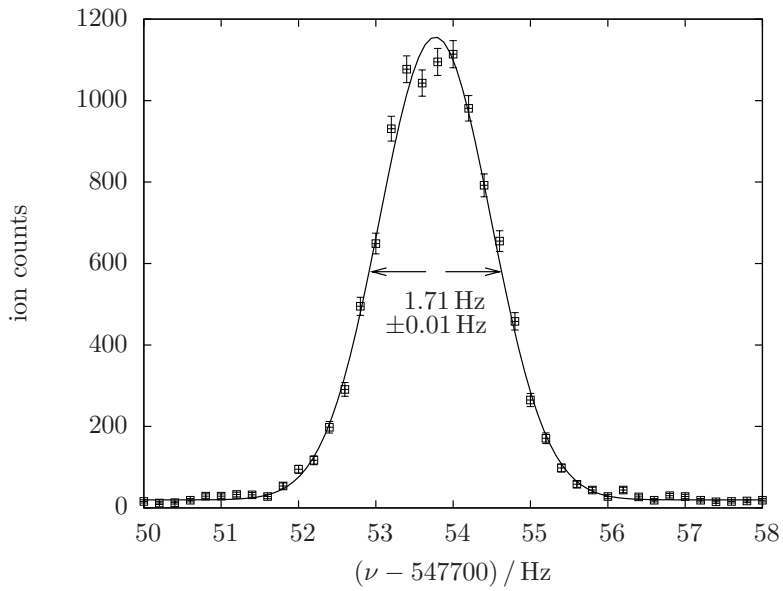

Figure 5.13: Ion counts as a function of the frequency for the QES with a pressure of $p = 3.0 \cdot 10^{-7}$ mbar at the Penning gauge and an excitation time of 500 ms.

and thus R_p is not further improved. For $3.0 \cdot 10^{-7}$ mbar and 50 ms, the resolving power is even higher than the theoretical values, which is related to the diaphragm $(\rho_{-,0}/\rho_{\mathrm{D}})$ as discussed in 2.4.2. For an excitation time of 500 ms, a high resolving power of $3.19(2) \cdot 10^5$ is achieved. Figure 5.13 shows the related measurement of the resonance curve.
The results for the OES are illustrated in Fig. 5.14. The R_p values as a function of T_{exc} for an OES are also converging to a maximum value as in a QES. For $3.0 \cdot 10^{-7}$ mbar, the resolving power is increased until $T_{\mathrm{exc}} = 750$ ms with $R_p = 4.16(9) \cdot 10^5$. Figure 5.15 shows the related measurement of the resonance curve. For all other pressures, the maximal maningful excitation time is 200 ms as obtained for a QES. For $3.0 \cdot 10^{-7}$ mbar the efficiency as obtained for the OES is increased for $T_{\mathrm{exc}} > 500$ms due to the long excitation time, which means, that the OES might be applicable for the preparation of longer lived ions. In this case the complete preparation would take more than 1 s if all other cooling and waiting times are taken into account.
To conclude the performed comparison of the OES with the QES, the result is that the OES is applicable for certain scenarios of mass measurements, since the resolving power is higher than in a QES. The main problem of the OES is a reduced efficiency and thus a not well performed ion centering. Due to this fact it can be a challenge to use such prepared ions for the next experimental step. It has been confirmed that the performed simulations with elastic collisions gives an adequate qualitative description of the experimental process.

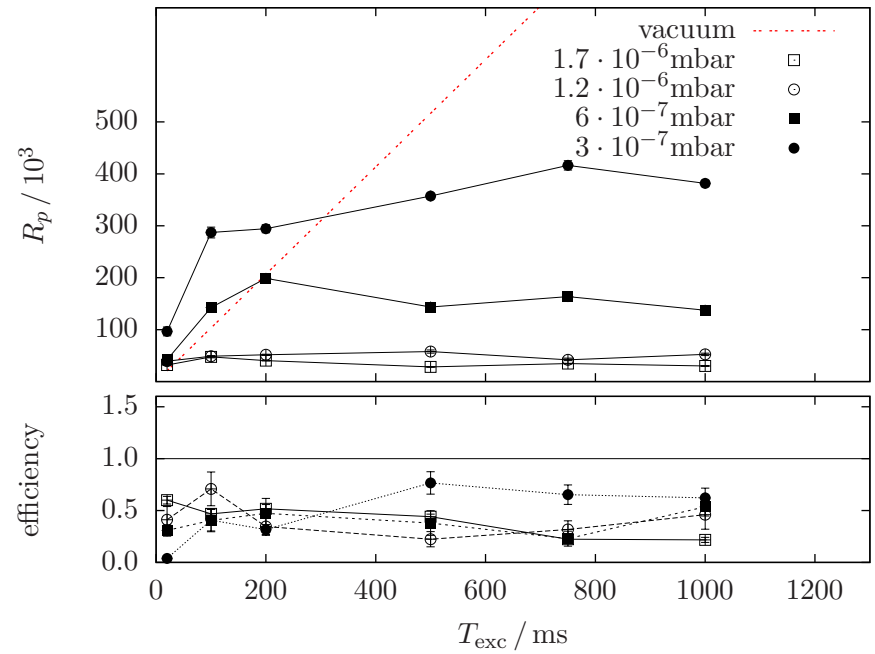

Figure 5.14: Resolving power and efficiency for $U/U_{\mathrm{B}} \leq 1$ as a function of the excitation duration for the OES at different pressures. Red line as in Fig. 5.12

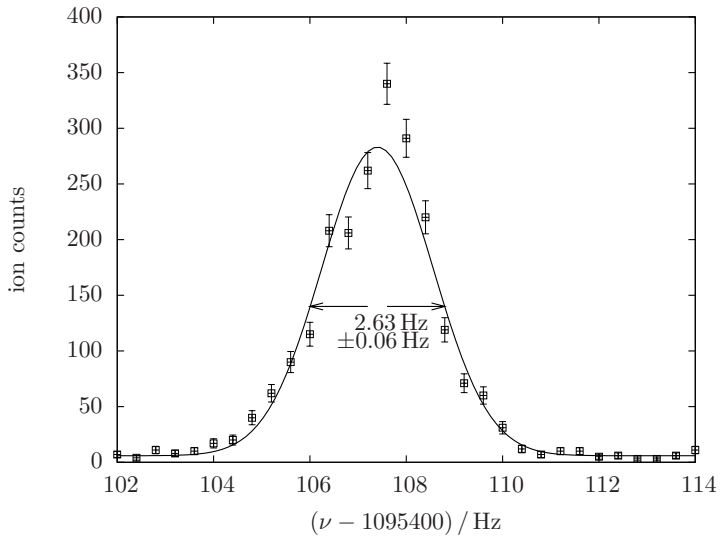

Figure 5.15: Ion counts as a function of the frequency for the OES with a pressure of $p = 3.0 \cdot 10^{-7}$ mbar at the Penning gauge and an excitation time of 750 ms.

5.4 Energy Distribution of Pre-Cooled Ions

For mass measurements, the ions have to be well prepared for the injection in the Precision Penning Trap. To investigate the quality of the ion bunch, additional parts of the ISOLTRAP setup are used. The ions are transfered from the preparation trap through the precision trap to the detector behind as shown in Fig. 4.1 in 4.1. Note that the precision trap is not switched to the trapping mode for this measurement. When the ions pass through the Precision Penning Trap, the electrical potential on the trap electrodes slows the ions down. The ions with a kinetic energy lower than the potential difference between the Precision Penning Trap and the previous drift section, are reflected and less ions are detected behind the Precision Penning Trap. Figure. 5.16 a) shows the number of detected ions as a function of the potential on the trap electrodes. The data points are fitted with the logistic fit function (Eq. (5.1)). The derivative of the fitted curve from the measurement as shown in Fig. 5.16 (b), gives an estimate for the energy distribution of the ion bunch. The same procedure is performed for different pressures (Fig. 5.17), in order to test, if low pressures as $3.0 \cdot 10^{-7}$ mbar or $6.0 \cdot 10^{-7}$ mbar as used for the previous measurements are applicable for mass measurements, since the R_p values of the resonances are high for these conditions. For pressures higher than

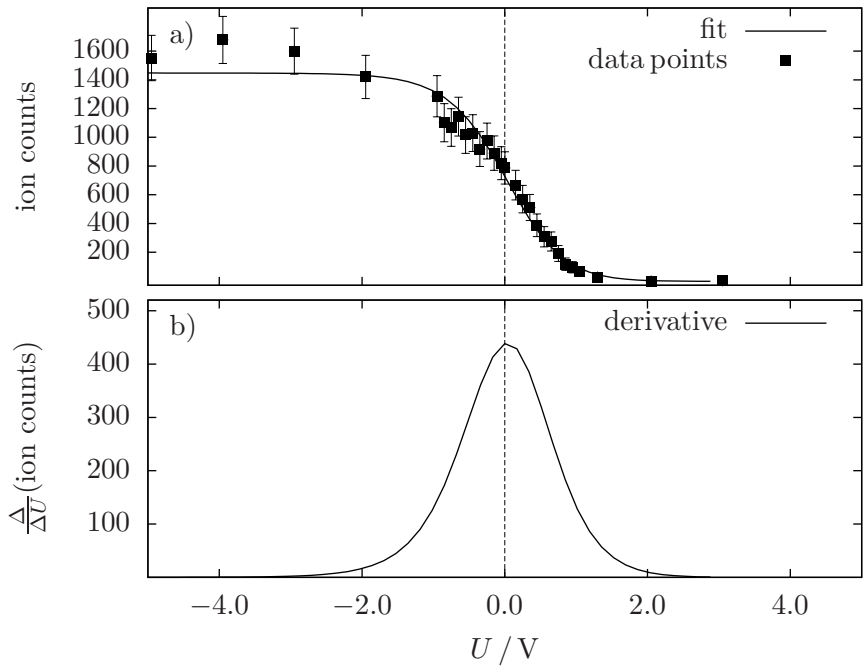

Figure 5.16: (a) Ion counts as a function of the potential, which is applied to the electrodes of the Precision Penning Trap, and a logistic fit (solid line) to the measured data. (b) Derivative of the curve. The value of the potential is set to zero at the point where the derivative has its maximum.

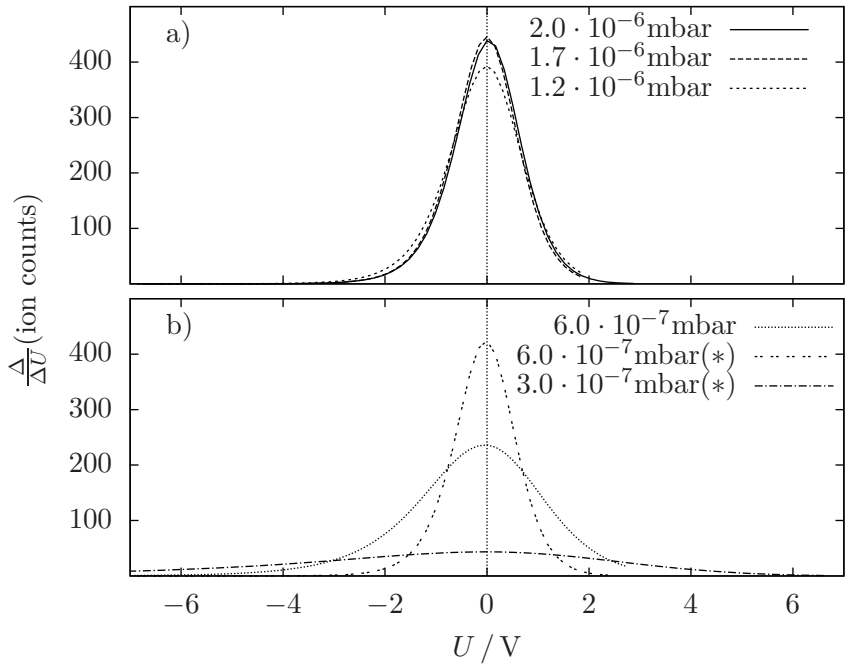

Figure 5.17: Derivatives of fitted data points as a function of the potential, which is applied to the trap electrodes in the precision trap as in Fig.5.16 (b). Curves with asterisk: 300 ms axial cooling time, 200 ms pre-cooling excitation time, and 150 ms radial cooling time. Curves without asterisk: 150 ms axial cooling time, 50 ms pre-cooling excitation time, and 150 ms radial cooling time.

$1.2 \cdot 10^{-6}$ mbar as commonly used for on-line experiments (Fig. 5.17 (a)), the energy distribution is adequate for the mass measurements. Figure 5.17 (b) shows that the use of low pressures is a challenge. With $6.0 \cdot 10^{-7}$ mbar it was possible to reach an energy distribution as for the higher pressures by using long waiting times (curve with asterisk in Fig. 5.17 (b)), but a pressure of $3.0 \cdot 10^{-7}$ mbar is not applicable, since the cooling process would need much longer than with the commonly used time settings. The curve with the long time setting is already very flat for $3.0 \cdot 10^{-7}$ mbar and a measurement with the shorter time setting could not be performed because the ions get lost on the way to the Precision Penning Trap. Thus, pressures down to $6.0 \cdot 10^{-7}$ mbar at the Penning gauge can be used, but they are more adequate for long lived nuclei, where the cooling times can be increased.

5.5 Test of the Conservation of the Motional Phases in a Buffer Gas Environment

In a buffer-gas environment the motional phases φ_+ and φ_- are affected by collisions with the neutral background atoms. In order to test if a phase sensitive excitation with the OES would be possible for future applications in a buffer gas environment, the conservation time of the motional phases has been determined. To investigate these conservation times, a dipolar signal from the AM300 frequency generator, which is used in the burst mode, is applied to opposite ring segments of the trap. The ions are excited and brought to a radius which is larger than the radius of the diaphragm. After a variable waiting time t_{wait}, the ions are excited twice with the same signal. If the difference between motional phase and the phase of the second signal is $\varphi_{\mathrm{d}} - \varphi_{\pm} \approx 180°$, the ions are moved back towards the center as discussed in 2.3.1. Figure 5.18 shows a test measurement, where the ions are excited in the same way, at their reduced cyclotron frequency $\nu_+ = \nu_c - \nu_- = 547453\,\mathrm{Hz}$, with exact 20 complete cycles of a sine function. The corresponding excitation time for the 20 cycles is $T_{\mathrm{exc}} = 36.5\,\mu\mathrm{s}$. The amplitude has to be at least 93 V to achieve a radius larger than ρ_D within this short excitation time. Thus the dipolar signal is amplified by the radio frequency amplifier in Tab. 4.2 in 4.8. The ions are, as long as the phase is conserved, centered for $t_{\mathrm{wait}} = (n+1/2)\cdot T_+$ with $T_+ = 1/\nu_+ = 1.827\mu\mathrm{s}$ and n as integer. To determine the conservation time of the reduced cyclotron phase, t_{wait} is increased in steps of $(m + 1/2) \cdot n \cdot T_+$, where m

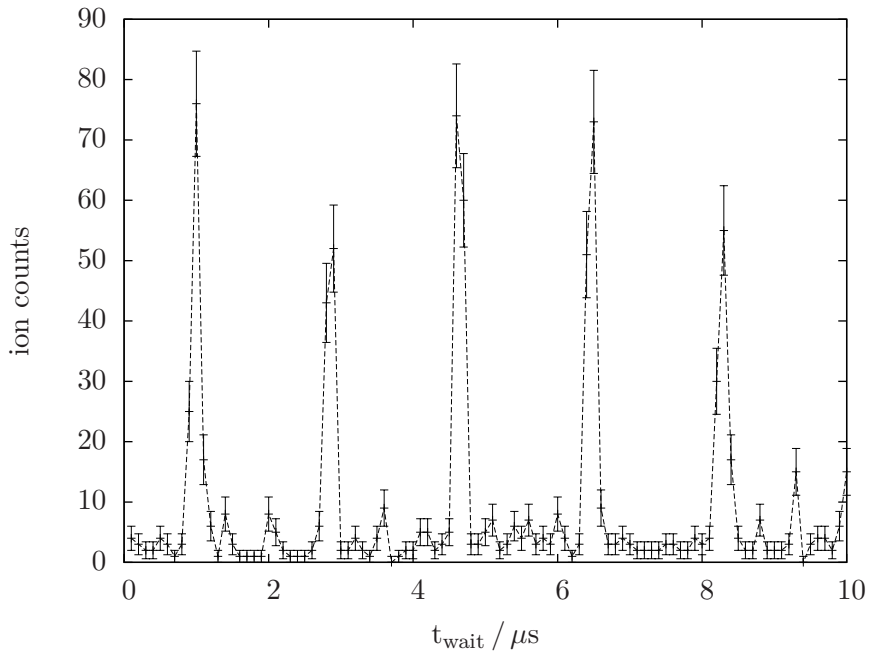

Figure 5.18: Ion counts as a function of the waiting time between two dipolar excitation signals at the reduced cyclotron frequency.

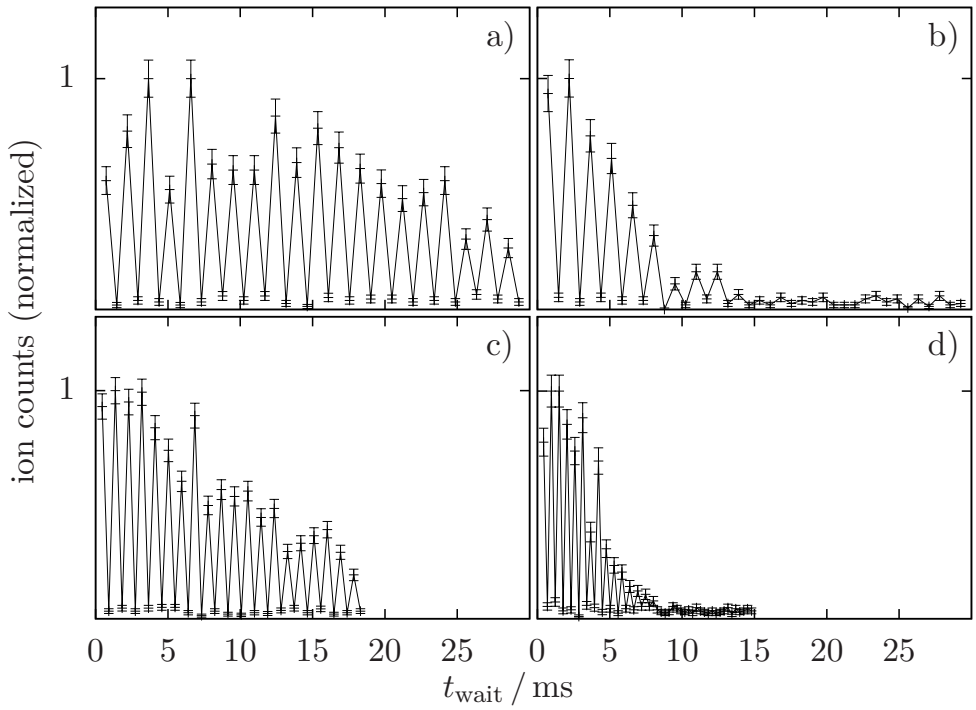

Figure 5.19: Normalized ion counts as a function of time. For every integer n (see text) a few measurement cycles are performed to collect statistical significant data. a) $p = 6.0 \cdot 10^{-7}$ mbar, $U_{\mathrm{d}} = 93\,\mathrm{V}$, and $m = 400$; b) $p = 6 \cdot 10^{-7}$ mbar, $U_{\mathrm{d}} = 186\,\mathrm{V}$, and $m = 400$; c) $p = 1.2 \cdot 10^{-6}$ mbar, $U_{\mathrm{d}} = 93\,\mathrm{V}$, and $m = 250$ d) $p = 1.2 \cdot 10^{-6}$ mbar, $U_{\mathrm{d}} = 186\,\mathrm{V}$, and $m = 180$.

is a fixed integer which is adapted to the measured time window. Independent from m, this results in a detection of the ions for $(n = 1, 3, 5, ...)$ and an absence of ions for $(n = 2, 4, 6, ...)$, as long as the phase is conserved. This is given in Fig. 5.19. The conservation time of the cyclotron phase is measured for two different initial radii after the first excitation ($\rho_1 \approx \rho_{\mathrm{D}}$, $\rho_2 \approx 2\rho_{\mathrm{D}}$), and two different pressures. To achieve the radius $2\rho_{\mathrm{D}}$, the amplitude is chosen to be $186\,\mathrm{V} = 2 \cdot 93\,\mathrm{V}$. It can be seen, that the influence of doubling the radius on the conservation time (right part of Fig. 5.19) is stronger than the influence of doubling the pressure (lower part of Fig. 5.19). This effect is assumed to be related to a velocity dependent mobility of the ions in the buffer gas as discussed in 3.3.
The conservation time is estimated with the first point for t_{wait}, where less than half of the ions are centered as compared to the maximum counts. The results are summarized in Tab. 5.3. The measurements for higher pressure as in part (c) are also performed for the magnetron phase φ_-, where the conservation time is about 200 ms. Thus the phase

Table 5.3: Measured conservation times for the phase of the reduced cyclotron motion. First column: Applied Pressure. Second column: Initial radius. Third column: Determined conservation time.

p / mbar	ρ_0	conservation time / ms
$3 \cdot 10^{-7}$	ρ_D	21
$3 \cdot 10^{-7}$	$2\rho_\mathrm{D}$	6.5
$6 \cdot 10^{-7}$	ρ_D	11.5
$6 \cdot 10^{-7}$	$2\rho_\mathrm{D}$	3

conservation time is limited by the reduced cyclotron motion.
Based on this results it can be tested tested to perform a phase sensitive excitation with an OES for a pressure of $p = 6.0 \cdot 10^{-7}$ mbar and an excitation time of less than $T_\mathrm{exc} \leq 20\,\mathrm{ms}$ to obtain higher resolving powers. These tests have not been performed in the present thesis, but for future applications they are of interest.

6 Summary and Outlook

In this thesis, alternative excitation schemes for the application in Penning traps have been investigated, with a main focus on the purification and cooling of ions in the Preparation Penning Trap of ISOLTRAP.
A simulation of ion motions in Penning traps with different excitation schemes has been developed in C++ via using a fifth order Gear method. Thus, different excitation schemes could be investigated and characterized in preparation of the measurements. In order to investigate cooling processes, different damping models have been tested: an approach with a continuous force, and an approach for elastic collisions with buffer gas atoms. The resolving power R_p of the simulated resonances was determined by the application of the bisection method, which ensures that the relative accuracy is independent of the total width of the simulated resonance curve.
A circular polarization for the dipolar and for the quadrupolar excitation scheme has been investigated by simulations and measurements, and compared with commonly used linearly polarized excitation schemes.
The result of the LPDES [Koe91] is a linearly with time increasing radus, modulated with additional oscillations. An excitation with the CPDES [SA93] results in the double of the radius in the same time for the same amplitude, and a vanishing of the modulation for the increasing radii as compared to the LPDES. Furthermore it has been obtained from a simulation, that if the CPDES is rotating against the ion motion, the radius is not increased and the ion performs small oscillations. The predictions for the CPDES have been confirmed by measurements.
For the ion motion in a CPQES, a solution has been obtained analytically, where it was possible to use the same approach as for the LPQES [BMSS90]. The beating frequency of the eigenmotions ν_{B} is doubled with a CPQES as compared with a LPQES for the same excitation amplitude. The LPQES and the CPQES have the same properties, if the amplitude which is used for the CPQES is half of the amplitude as used for the LPQES. Differences in high frequency terms are neglected. Furthermore the conversions of eigenmotions are not performed if the field of the CPQES is rotating against the motion of the ions. In this case, only high frequency oscillations are performed. These effects are confirmed by measurements.
As an approach for mass selective buffer-gas cooling with higher resolving powers, the OES has been investigated. In simulations with a single ion, it has been observed, that the motion of an ion is much more sensitive to the initial conditions due to a radial nonlinearity of the field. The resonance curves show different shapes, which depend on the parameters for the excitation as the excitation amplitude, the initial motional phases, and the initial radii. For well chosen parameters it is possible to obtain a resolving power which is two orders of magnitude higher than obtained from the QES. The OES and the QES have been investigated by simulations for the application in a buffer gas cooling process using a continuous damping force and using the elastic collision model

for a helium buffer gas, respectively. The simulation with the continuous damping force model predicted a high efficiency for both excitation schemes and much higher resolving powers for the OES as compared to the QES. The simulations of ions which are affected by collisions, predicted comparable resolving powers for both excitation schemes, and a lower efficiency for the OES, whereas the results for the QES did not change significantly as compared with the continuous damping approach. A sufficient approximation of the measurements with cooling processes is obtained by using the model with elastic collisions.

The OES and the QES have been furthermore compared in systematic measurements of cooling resonances for $^{133}Cs^{+}$ ions in the Preparation Penning Trap. The resolving power of the OES and the QES are in the same range for both excitation schemes for pressures as commonly used for the preparation of mass measurements. For pressures below, the resolving power for the OES is about two times higher as compared with the QES. For parameters as used for mass measurements, the efficiencies which have been measured for the OES are always lower as compared to the QES. Thus the OES is of limited applicability.

For the future, investigations using heavier ion masses in an OES are of interest, since the ion motion is more stable under influence of collisions. This could be investigated with carbon clusters from the laser ion source at ISOLTRAP. Furthermore the pre-cooling mechanism could be improved by a time dependent pressure inside the Preparation Penning Trap via implementing a Piezo valve. The axial cooling, the pre-cooling, and the radial cooling are performed at high pressures, whereas the main excitation takes place in a low-pressure environment. This would decrease the bunch width and thus reduce the distribution of ν_B for the OES on one hand, and ensures a high resolving power with low pressures on the other hand. In addition, a phase sensitive excitation with the OES for longer excitation times would be possible.

Precision measurements with an OES are as well an interesting topic for future applications. It might be well applicable in a Precision Penning Trap with single ions, if the initial conditions are defined very precisely. This could be performed in modern cryogenic traps in vacuum environments.

An investigation of a circularly polarized octupolar excitation would be of interest, but a trap with a 16 fold ring electrode would be necessary to perform these measurements.

A Solution of the Equations of motion in the Quadrupolar excitation scheme

An analytical solution for a radial quadrupolar excitation [BG86], [BMSS90] will be discussed in detail in the following. Starting from Eq. (2.41) for the V-components

$$\begin{aligned}\dot{V}_x^{\pm} &= -\omega_{\pm} V_y^{\pm} + kV_x^{+} - kV_x^{-}\\ \dot{V}_y^{\pm} &= \omega_{\pm} V_x^{\pm} - kV_y^{+} + kV_y^{-}.\end{aligned}$$

The equations for V^+ and V^- are coupled for quadrupolar excitation. To solve Eq. (2.41), the ansatz

$$\begin{aligned}V_x^{\pm} &= A_x^{\pm}(t) e^{\pm \mathrm{i}\omega_{\pm} t}\\ V_y^{\pm} &= A_y^{\pm}(t) e^{\pm \mathrm{i}\omega_{\pm} t},\end{aligned} \tag{A.1}$$

is used [BMSS90].

A substitution of Eq. (A.1) in Eq. (2.41) with $\dot{\vec{V}}^{\pm} = \dot{\vec{A}}^{\pm} e^{\pm \mathrm{i}\omega_{\pm} t} \pm \mathrm{i}\omega_{\pm} \vec{A} e^{\pm \mathrm{i}\omega_{\pm} t}$ and rewriting the cosine function $\cos(\omega_{\mathrm{q}} t) = \frac{1}{2}(e^{\mathrm{i}\omega_{\mathrm{q}} t} + e^{-\mathrm{i}\omega_{\mathrm{q}} t})$ leads to

$$\begin{aligned}&\dot{A}_x^{\pm} e^{\pm \mathrm{i}\omega_{\pm} t} \pm \mathrm{i}\omega_{\pm} A_x^{\pm} e^{\pm \mathrm{i}\omega_{\pm} t} = \\ &\qquad - \omega_{\pm} A_y^{\pm} e^{\pm \mathrm{i}\omega_{\pm} t} + \frac{k_0}{2}\left(e^{\mathrm{i}\omega_{\mathrm{q}} t} + e^{-\mathrm{i}\omega_{\mathrm{q}} t}\right)\left(A_x^{+} e^{\mathrm{i}\omega_{+} t} - A_x^{-} e^{-\mathrm{i}\omega_{-} t}\right).\\ &\dot{A}_y^{\pm} e^{\pm \mathrm{i}\omega_{\pm} t} \pm \mathrm{i}\omega_{\pm} A_y^{\pm} e^{\pm \mathrm{i}\omega_{\pm} t} = \\ &\qquad \omega_{\pm} A_x^{\pm} e^{\pm \mathrm{i}\omega_{\pm} t} - \frac{k_0}{2}\left(e^{\mathrm{i}\omega_{\mathrm{q}} t} + e^{-\mathrm{i}\omega_{\mathrm{q}} t}\right)\left(A_y^{+} e^{\mathrm{i}\omega_{+} t} - A_y^{-} e^{-\mathrm{i}\omega_{-} t}\right).\end{aligned} \tag{A.2}$$

Dividing by $e^{\pm \mathrm{i}\omega_{\pm} t}$ and expanding gives

$$\begin{aligned}&\dot{A}_x^{\pm} \pm \mathrm{i}\omega_{\pm} A_x^{\pm} = \\ &\quad - \omega_{\pm} A_y^{\pm} + \frac{k_0}{2}\Big(A_x^{+} e^{\mathrm{i}\omega_{\mathrm{q}} t} e^{\mathrm{i}\omega_{+} t} e^{\mp \mathrm{i}\omega_{\pm} t} - A_x^{-} e^{\mathrm{i}\omega_{\mathrm{q}} t} e^{-\mathrm{i}\omega_{-} t} e^{\mp \mathrm{i}\omega_{\pm} t}\\ &\quad + A_x^{+} e^{-\mathrm{i}\omega_{\mathrm{q}} t} e^{\mathrm{i}\omega_{+} t} e^{\mp \mathrm{i}\omega_{\pm} t} - A_x^{-} e^{-\mathrm{i}\omega_{\mathrm{q}} t} e^{-\mathrm{i}\omega_{-} t} e^{\mp \mathrm{i}\omega_{\pm} t}\Big),\\ &\dot{A}_y^{\pm} \pm \mathrm{i}\omega_{\pm} A_y^{\pm} = \\ &\quad + \omega_{\pm} A_x^{\pm} - \frac{k_0}{2}\Big(A_y^{+} e^{\mathrm{i}\omega_{\mathrm{q}} t} e^{\mathrm{i}\omega_{+} t} e^{\mp \mathrm{i}\omega_{\pm} t} - A_y^{-} e^{\mathrm{i}\omega_{\mathrm{q}} t} e^{-\mathrm{i}\omega_{-} t} e^{\mp \mathrm{i}\omega_{\pm} t}\\ &\quad + A_y^{+} e^{-\mathrm{i}\omega_{\mathrm{q}} t} e^{\mathrm{i}\omega_{+} t} e^{\mp \mathrm{i}\omega_{\pm} t} - A_y^{-} e^{-\mathrm{i}\omega_{\mathrm{q}} t} e^{-\mathrm{i}\omega_{-} t} e^{\mp \mathrm{i}\omega_{\pm} t}\Big).\end{aligned} \tag{A.3}$$

After comparing the parts for A^+ and A^- and using symmetries in Eq. (A.3), one can write

$$\begin{aligned}
&\dot{A}_x^{\pm} \pm \mathrm{i}\omega_{\pm} A_x^{\pm} = \\
&\quad - \omega_{\pm} A_y^{\pm} \pm \frac{k_0}{2}\left(A_x^{\pm}\left(e^{\mathrm{i}\omega_\mathrm{q} t} + e^{-\mathrm{i}\omega_\mathrm{q} t}\right) - A_x^{\mp}\left(e^{\pm\mathrm{i}(\omega_\mathrm{q}-\omega_c)t} + e^{\mp\mathrm{i}(\omega_\mathrm{q}+\omega_c)t}\right)\right), \\
&\dot{A}_y^{\pm} \pm \mathrm{i}\omega_{\pm} A_y^{\pm} = \\
&\quad + \omega_{\pm} A_x^{\pm} \mp \frac{k_0}{2}\left(A_y^{\pm}\left(e^{\mathrm{i}\omega_\mathrm{q} t} + e^{-\mathrm{i}\omega_\mathrm{q} t}\right) - A_y^{\mp}\left(e^{\pm\mathrm{i}(\omega_\mathrm{q}-\omega_c)t} + e^{\mp\mathrm{i}(\omega_\mathrm{q}+\omega_c)t}\right)\right),
\end{aligned} \tag{A.4}$$

with the sum of the eigenfrequencies $\omega_c = \omega_+ + \omega_-$. For weak excitations, $k_0 \ll \omega_-$, and an excitation frequency $\omega_\mathrm{q} \approx \omega_c$, a slow change of the amplitudes A^+ and A^- with the frequency $\omega_\mathrm{q} - \omega_c$ is obtained which is modulated with the frequencies $\omega_\mathrm{q} + \omega_c$ and ω_q which are very high with respect to $\omega_\mathrm{q} - \omega_c$. The negligence of the high frequency terms gives

$$\begin{aligned}
\dot{A}_x^{\pm} &= \mp\mathrm{i}\omega_{\pm} A_x^{\pm} - \omega_{\pm} A_y^{\pm} \mp \frac{k_0}{2} A_x^{\mp} \cdot e^{\pm\mathrm{i}(\omega_\mathrm{q}-\omega_c)t}, \\
\dot{A}_y^{\pm} &= \mp\mathrm{i}\omega_{\pm} A_y^{\pm} + \omega_{\pm} A_x^{\pm} \pm \frac{k_0}{2} A_y^{\mp} \cdot e^{\pm\mathrm{i}(\omega_\mathrm{q}-\omega_c)t}.
\end{aligned} \tag{A.5}$$

If $\omega_+ \gg \omega_-$ like in most experiments, one can assume that the cyclotron motion is close to a circle. This leads to a further simplification for the amplitudes which turn in the complex plane with positive rotational direction for A^+ and negative rotational direction for A^-

$$\begin{aligned}
A_y^+ &= -\mathrm{i}A_x^+ = -\mathrm{i}A^+, \\
A_y^- &= \mathrm{i}A_x^- = -\mathrm{i}A^-.
\end{aligned} \tag{A.6}$$

The first two terms in Eq. (A.6) are eliminated and it results in

$$\begin{aligned}
\dot{A}^+ &= -\frac{k_0}{2} A^- \cdot e^{\mathrm{i}(\omega_\mathrm{q}-\omega_c)t}, \\
\dot{A}^- &= +\frac{k_0}{2} A^+ \cdot e^{-\mathrm{i}(\omega_\mathrm{q}-\omega_c)t}.
\end{aligned} \tag{A.7}$$

To solve this equation, the ansatz

$$\begin{aligned}
A^+ &= A_0^+ e^{\mathrm{i}(\xi_+ t + \varphi_{B+})}, \\
A^- &= A_0^- e^{\mathrm{i}(\xi_- t + \varphi_{B-})},
\end{aligned} \tag{A.8}$$

is used [BMSS90] with ξ_+ and ξ_- as constants.
Substituting the ansatz into Eq. (A.7) for the resonant case $\omega_\mathrm{q} = \omega_c$ gives

$$\begin{aligned}
\dot{A}^+ &= \mathrm{i}A_0^+ \xi_+ e^{\mathrm{i}(\xi_+ t + \varphi_{B+})} = -\frac{k_0}{2} A_0^- e^{\mathrm{i}(\xi_- t + \varphi_{B-})}, \\
\dot{A}^- &= \mathrm{i}A_0^- \xi_- e^{\mathrm{i}(\xi_- t + \varphi_{B-})} = +\frac{k_0}{2} A_0^+ e^{\mathrm{i}(\xi_+ t + \varphi_{B+})}.
\end{aligned} \tag{A.9}$$

The isolation of A_0^+ in Eq. (A.10)

$$A_0^+ = \frac{2\mathrm{i}}{k_0} A_0^- \xi_- \frac{e^{\mathrm{i}(\xi_- t + \varphi_{B-})}}{e^{\mathrm{i}(\xi_+ t + \varphi_{B+})}}, \tag{A.10}$$

and the substitution into Eq. (A.9) leads to the relation

$$\xi_+ \xi_- = \left(\frac{k_0}{2}\right)^2, \tag{A.11}$$

and the division of Eq. (A.9) by Eq. (A.10)

$$\frac{A_0^+ \xi_+ e^{\mathrm{i}(\xi_+ t + \varphi_{B+})}}{A_0^- \xi_- e^{\mathrm{i}(\xi_- t + \varphi_{B-})}} = -\frac{A_0^- e^{\mathrm{i}(\xi_- t + \varphi_{B-})}}{A_0^+ e^{\mathrm{i}(\xi_+ t + \varphi_{B+})}}, \tag{A.12}$$

results in the relation

$$\frac{\xi_+}{\xi_-} = -\left(\frac{A_0^-}{A_0^+}\right)^2 e^{2i((\xi_- - \xi_+)t + \varphi_{B-} - \varphi_{B+})}. \tag{A.13}$$

Since ξ_+ and ξ_- are not time dependent, the right hand side of Eq. (A.13) is nether. Hence the time dependency in the exponent has to be eliminated and thus $\xi_+ = \xi_- = \xi = \pm k_0/2$. Furthermore if A_0^+ and A_0^- are real numbers the exponential function is also real. For this condition $\varphi_{B-} - \varphi_{B+} = \pm\pi/2$ and thus the value of the exponential function is -1. In that case $A_0^+ = A_0^-$ satisfies the left hand side. From the substitution of $\xi = \pm k_0/2$ into Eq. (A.9) or Eq. (A.10), a condition for ξ and $\varphi_{\pm,conv}$ is obtained

$$\begin{aligned} \xi = +\frac{k_0}{2} &\rightarrow \varphi_{B+} = \varphi_{B-} + \frac{\pi}{2}, \\ \xi = -\frac{k_0}{2} &\rightarrow \varphi_{B+} = \varphi_{B-} - \frac{\pi}{2}. \end{aligned} \tag{A.14}$$

The two possibilities for ξ allow two solutions for each Eq. (A.9) and Eq. (A.10). With the A_0 written as α and Eq. (A.14) the sum of the two solutions for A^+ and A^- is

$$\begin{aligned} A^+ &= \alpha_1 e^{\mathrm{i}(\varphi_{B-} + \pi/2 + k_0/2t)} + \alpha_2 e^{\mathrm{i}(\varphi_{B-} - \pi/2 - k_0/2t)} \\ A^- &= \alpha_1 e^{\mathrm{i}(\varphi_{B-} + k_0/2t)} + \alpha_2 e^{\mathrm{i}(\varphi_{B-} - k_0/2t)} \end{aligned} \tag{A.15}$$

Since the ansatz in Eq. (A.1) is equal to Eq. (2.23), the radii $\rho_+(t)$ and $\rho_-(t)$ are obtained like in Eq. (2.26). After expanding Eq. (A.15) with sine and cosine functions and isolating the real part, one obtaines

$$\begin{aligned} \rho_+(t) &= \rho_{+,0} \cos\left(\frac{k_0}{2}t\right) - \rho_{-,0} \sin\left(\frac{k_0}{2}t\right), \\ \rho_-(t) &= \rho_{-,0} \cos\left(\frac{k_0}{2}t\right) + \rho_{+,0} \sin\left(\frac{k_0}{2}t\right), \end{aligned} \tag{A.16}$$

with initial radii which are determined by α_1, α_2, and φ_{B-}

$$\rho_{+,0} = \frac{\alpha_2 - \alpha_1}{\omega_+ - \omega_-} \sin(\varphi_{B-}), \tag{A.17}$$
$$\rho_{-,0} = \frac{\alpha_2 + \alpha_1}{\omega_+ - \omega_-} \cos(\varphi_{B-}).$$

The initial radii determine the coefficients α_1, α_2, and the initial phase φ_{B-}. The phase $\varphi_{B\pm}$ belongs to the slow oscillation with the beating frequency $\omega_\mathrm{B} = k_0/2$. The most interesting setting for the initial conditions is $\rho_{\pm,0} = 0$ with $\rho_{\mp,0} \neq 0$ which is achieved by $\alpha_1 = \pm\alpha_2$ with $\varphi_{B-} = 0$ for $\alpha_1 = +\alpha_2$, and $\varphi_{B-} = \pi/2$ for $\alpha_1 = -\alpha_2$. With these conditions, periodic total conversions of the two eigenmotions with the beating frequency ω_B are performed.
The initial conditions are now chosen such that $\varphi_{B-} = 0$ and $\alpha_1 = +\alpha_2 = \alpha$. In this case Eq. (A.16) is reduced to

$$\rho_+(t) = \rho_0 \sin(\omega_\mathrm{B} t), \tag{A.18}$$
$$\rho_-(t) = \rho_0 \cos(\omega_\mathrm{B} t),$$

with

$$\rho_0 = \frac{2\alpha}{\omega_+ - \omega_-}. \tag{A.19}$$

Thus a pure initial magnetron motion is fully converted into cyclotron motion and vice versa. For this choice of parameters the spacial coordinates $x(t)$ and $y(t)$ are calculated as follows. With the solution for $A^\pm$, the components for $V^\pm$ are obtained using Eq. (A.6) and Eq. (A.1)

$$V_x^+ = \alpha \left(e^{\mathrm{i}((\omega_+ + \omega_\mathrm{B})t + \pi/2)} + e^{\mathrm{i}((\omega_+ - \omega_\mathrm{B})t - \pi/2)} \right), \tag{A.20}$$
$$V_x^- = \alpha \left(e^{-\mathrm{i}(\omega_- - \omega_\mathrm{B})t} + e^{-\mathrm{i}(\omega_- + \omega_\mathrm{B})t} \right),$$
$$V_y^+ = -\mathrm{i} V_x^+,$$
$$V_y^- = \mathrm{i} V_x^-.$$

After the transformation to sine and cosine functions and isolating the real part of the terms, the components are

$$V_x^+ = +2\alpha \sin(\omega_+ t) \sin(\omega_\mathrm{B} t), \tag{A.21}$$
$$V_x^- = -2\alpha \sin(\omega_- t) \cos(\omega_\mathrm{B} t),$$
$$V_y^+ = -2\alpha \cos(\omega_+ t) \sin(\omega_\mathrm{B} t),$$
$$V_y^- = +2\alpha \cos(\omega_- t) \cos(\omega_\mathrm{B} t).$$

After the transformation to $x(t)$ and $y(t)$ with Eq. (2.24), the result is Eq. (2.43) in 2.3.3, where the initial phases φ_+ and φ_- are chosen to be zero if $t = 0$ and $\vec{\rho} = (x, y) =$

$((\rho_{+,0} + \rho_{-,0}), 0)$:

$$x(t) = \rho_0 \left(\cos\left(\omega_+ t\right) \sin\left(\omega_\mathrm{B} t\right) + \cos\left(\omega_- t\right) \cos\left(\omega_\mathrm{B} t\right)\right),$$
$$y(t) = \rho_0 \left(\sin\left(\omega_+ t\right) \sin\left(\omega_\mathrm{B} t\right) + \sin\left(\omega_- t\right) \cos\left(\omega_\mathrm{B} t\right)\right).$$

Bibliography

[BAB+08] S. Baruah, G. Audi, K. Blaum, M. Dworschak, S. George, C. Guénaut, U. Hager, F. Herfurth, A. Herlert, A. Kellerbauer, H.-J. Kluge, D. Lunney, H. Schatz, L. Schweikhard, C. Yazidjian, *Mass Measurements beyond the Major r-Process Waiting Point ^{80}Zn*, Phys. Rev. Lett., 101(26):262501, **2008**

[BBB+08] M. Breitenfeldt, S. Baruah, K. Blaum, A. Herlert, M. Kretzschmar, F. Martinez, G. Marx, L. Schweikhard, N. Walsh, *The elliptical Penning trap: Experimental investigations and simulations*, Int. J. Mass Spectrom., 275(1-3):34 – 44, **2008**

[Bec93] D. Beck, *Diplomarbeit: Aufbau einer zylindrischen Penningfalle zum Einfang und Kühlen von Ionen*, Dissertation, Johannes Gutenberg-Universität Mainz, **1993**

[Bec97] D. Beck, *Massenbestimmung instabiler Isotope der Seltenen Erden um ^{146}Gd mit dem ISOLTRAP-Spektrometer*, Dissertation, Johannes Gutenberg-Universität Mainz, **1997**

[BG86] L. S. Brown, G. Gabrielse, *Geonium theory: Physics of a single electron or ion in a Penning trap*, Rev. Mod. Phys., 58(1):233–311, **1986**

[Bla06] K. Blaum, *High-accuracy mass spectrometry with stored ions*, Phys. Rep., 425(1):1 – 78, **2006**

[BMSS90] G. Bollen, R. B. Moore, G. Savard, H. Stolzenberg, *The accuracy of heavy-ion mass measurements using time of flight-ion cyclotron resonance in a Penning trap*, J. of Appl. Phys., 68(9):4355–4374, **1990**

[Boe09] C. Boehm, Dissertation, Universität Mainz, **2009**

[BZH+07] M. Breitenfeldt, F. Ziegler, A. Herlert, G. Marx, L. Schweikhard, *Simultaneous monitoring of the radial modes of the ion motion and their manipulation in Penning traps by FT-ICR mass spectrometry*, Int. J. Mass Spectrom., 263(1):94 – 100, **2007**

[com] *Group for Computational Material Science Universität Greifswald Germany*

[Com78] M. B. Comarisov, *Theory of Fourier-transform ion-cyclotron resonance mass-spectroscopy. 2. Signal modeling for ion-cyclotron resonance*, J. Chem. Phys., 69(9):4097–4104, **1978**

[DAB+06] P. Delahaye, G. Audi, K. Blaum, F. Carrel, S. George, F. Herfurth, A. Herlert, A. Kellerbauer, H.-J. Kluge, D. Lunney, L. Schweikhard, C. Yazidjian, *High-accuracy mass measurements of neutron-rich Kr isotopes*, Phys. Rev. C, 74(3):034331, **2006**

[EBC+07] S. Eliseev, M. Block, A. Chaudhuri, F. Herfurth, H.-J. Kluge, A. Martin, C. Rauth, G. Vorobjev, *Octupolar excitation of ions stored in a Penning trap mass spectrometer–A study performed at SHIPTRAP*, International Journal of Mass Spectrometry, 262(1-2):45 – 50, **2007**

[EMA+78] H. W. Ellis, E. W. McDaniel, D. L. Albritton, L. A. Viehland, S. L. Lin, E. A. Mason, *Transport properties of gaseous ions over a wide energy range. Part II*, Atomic Data and Nuclear Data Tables, 22(3):179 – 217, **1978**

[Gea71] C. W. Gear, *Numerical Initial Value Problems in Ordinary Differential Equations*, Prentice Hall PTR, Upper Saddle River, NJ, USA, **1971**

[GKT80] G. Gräff, H. Kalinowsky, J. Traut, *A Direct Determination of the Proton Electron Mass Ratio*, Z. Phys. A, 297(1):35–39, **1980**

[HAB+04] F. Herfurth, G. Audi, D. Beck, K. Blaum, G. Bollen, P. Delahaye, C. Guénaut, A. Kellerbauer, H.-J. Kluge, D. Lunney, D. Rodríguez, S. Saxena, S. Schwarz, L. Schweikhard, G. Sikler, C. Yazidjian, *Masses along the rp-process path and large scale surveys on Cu, Ni and Ga with ISOLTRAP*, Nucl. Phys. A, 746:487 – 492, proceedings of the Sixth International Conference on Radioactive Nuclear Beams (RNB6), **2004**

[HDK+01] F. Herfurth, J. Dilling, A. Kellerbauer, G. Bollen, S. Henry, H.-J. Kluge, E. Lamour, D. Lunney, R. B. Moore, C. Scheidenberger, S. Schwarz, G. Sikler, J. Szerypo, *A linear radiofrequency ion trap for accumulation, bunching, and emittance improvement of radioactive ion beams*, Nuclear Instruments and Methods in Physics Research Section A: Accelerators, Spectrometers, Detectors and Associated Equipment, 469(2):254 – 275, **2001**

[HL97] W. Huang, B. Leimkuhler, *The Adaptive Verlet Method*, SIAM J. Sci. Comput., 18(1):239–256, **1997**

[KAB+04] A. Kellerbauer, G. Audi, D. Beck, K. Blaum, G. Bollen, B. A. Brown, P. Delahaye, C. Guénaut, F. Herfurth, H.-J. Kluge, D. Lunney, S. Schwarz, L. Schweikhard, C. Yazidjian, *Direct Mass Measurements on the Super-allowed Emitter ^{74}Rb and Its Daughter ^{74}Kr: Isospin-Symmetry-Breaking Correction for Standard-Model Tests*, Phys. Rev. Lett., 93(7):072502, **2004**

[KBB+03] A. Kellerbauer, K. Blaum, G. Bollen, F. Herfurth, H.-J. Kluge, M. Kuckein, E. Sauvan, C. Scheidenberger, L. Schweikhard, *From direct to absolute mass measurements: A study of the accuracy of ISOLTRAP*, Eur. Phys. J. D, 22(1):53–64, **2003**

[KBK+95] M. König, G. Bollen, H.-J. Kluge, T. Otto, J. Szerypo, *Quadrupole excitation of stored ion motion at the true cyclotron frequency*, Int. J. Mass Spectrom., 142(1-2):95 – 116, **1995**

[Koe91] M. Koenig, *Diploma Thesis: Massenspektrometrische Auflösung von Isomer und Grundzustand in der Penningfalle und Untersuchungen zur Coulombwechselwirkung gespeicherter Ionen*, Dissertation, Johannes Gutenberg-Universität Mainz, Germany, **1991**

[Kre91] *Particle motion in a Penning trap*, Eur. J. Phys., 12(2-3):240 – 246, **1991**

[Kug00] E. Kugler, *The ISOLDE facility*, Hyperfine Interactions, 129:23– 42, **2000**

[Mat] K. Matyash, *Kinetic Modeling of Multi-Component Edge Plasmas*, Dissertation, Univerität Greifswald

[MBB+08] M. Mukherjee, D. Beck, K. Blaum, G. Bollen, J. Dilling, S. George, F. Herfurth, A. Herlert, A. Kellerbauer, H.-J. Kluge, S. Schwarz, L. Schweikhard, C. Yazidjian, *ISOLTRAP: An on-line Penning trap for mass spectrometry on short-lived nuclides*, Eur. Phys. J. A, 35(1):1–29, **2008**

[MF09] M. G. S. L. W. N. Martinez F., Herlert A., *Unintended parametric ejection of ions from an ion cyclotron resonance trap by two- electrode axialization*, EJMS, 15:283–291, **2009**

[MKB+04] M. Mukherjee, A. Kellerbauer, D. Beck, K. Blaum, G. Bollen, F. Carrel, P. Delahaye, J. Dilling, S. George, C. Guénaut, F. Herfurth, A. Herlert, H.-J. Kluge, U. Köster, D. Lunney, S. Schwarz, L. Schweikhard, C. Yazidjian, *The Mass of $Mg22$*, Phys. Rev. Lett., 93(15):150801, **2004**

[MM73] McDaniel, E. Mason, *The Mobility and Diffusion of Ions in Gases*, Wiley,New York, **1973**

[MM88] E. Mason, McDaniel, *Transport Properties of Ions in Gases*, Wiley,New York, **1988**

[NAB+09] D. Neidherr, G. Audi, D. Beck, K. Blaum, C. Böhm, M. Breitenfeldt, R. B. Cakirli, R. F. Casten, S. George, F. Herfurth, A. Herlert, A. Kellerbauer, M. Kowalska, D. Lunney, E. Minaya-Ramirez, S. Naimi, E. Noah, L. Penescu, M. Rosenbusch, S. Schwarz, L. Schweikhard, T. Stora, *Discovery of [sup 229]Rn and the Structure of the Heaviest Rn and Ra Isotopes from Penning-Trap Mass Measurements*, Phys. Rev. Lett., 102(11):112501, **2009**

[OBS+93] T. Otto, G. Bollen, G. Savard, L. Schweikhard, H. Stolzenberg, G. Audi, R. B. Moore, G. Rouleau, J. Szerypo, Z. Patyk, *Penning-trap mass measurements of neutron-deficient Rb and Sr isotopes*, Nuclear Physics A, 567(2):281 – 302, **1993**

[RBS+07] R. Ringle, G. Bollen, P. Schury, S. Schwarz, T. Sun, *Octupolar excitation of ion motion in a Penning trap–A study performed at LEBIT*, International Journal of Mass Spectrometry, 262(1-2):33 – 44, **2007**

[RKA+05] D. Rodríguez, V. S. Kolhinen, G. Audi, J. Äystö, D. Beck, K. Blaum, G. Bollen, F. Herfurth, A. Jokinen, A. Kellerbauer, H.-J. Kluge, M. Oinonen, H. Schatz, E. Sauvan, S. Schwarz, *Mass measurement on the rp-process waiting point 72Kr*, Eur. Phys. J. A, 25(Supplement 1):s1.41–s1.43, **2005**

[SA93] Schweikhard, M. A.G., *Excitation modes for Fourier transform-ion cyclotron resonance mass spectrometry*, Bd. 4, **1993**

[SBB+90] H. Stolzenberg, S. Becker, G. Bollen, F. Kern, H. Kluge, T. Otto, G. Savard, L. Schweikhard, G. Audi, R. Moore, *Accurate mass determination of short-lived isotopes by a tandem penning-trap mass spectrometer*, **1990**

[SBB+91] G. Savard, S. Becker, G. Bollen, H.-J. Kluge, R. Moore, T. Otto, L. Schweikhard, H. Stolzenberg, U. Wiess, *A New Cooling Technique For Heavy-Ions In A Penning Trap*, Phys. Lett. A, 158(5):247–252, **1991**

[Sch08] S. Schwarz, *Simulations for Ion Traps - Buffer Gas cooling*, Lect. Notes Phys., 749:97–117, **2008**

[SZBL95] L. Schweikhard, J. Ziegler, H. Bopp, K. Lützenkirchen, *The trapping condition and a new instability of the ion motion in the ion cyclotron resonance trap*, International Journal of Mass Spectrometry and Ion Processes, 141(1):77 – 90, **1995**

Danksagung

Ich möchte mich an dieser Stelle herzlich bei allen die mich bei dieser Arbeit Unterstützt haben bedanken. Ganz besonders möchte ich mich bei Professor Schweikhard bedanken, der mir die Aufnahme in die Arbeitsgruppe ermöglicht und mit vielen Ideen und Anstößen zur Entstehung der Arbeit beigetragen hat. Besonderer Dank gilt ebenfalls meinem Betreuer Martin Breitenfeldt, der mich am Experiment ISOLTRAP ausgebildet hat und mir bei vielen Problemen tatkräftig zur Seite stand. Ebenso gilt dieser Dank allen weiteren Mitwirkenden am Experiment ISOLTRAP: Dennis Neidherr, Sarah Naimi, Dr. Magdalena Kowalska, Christine Böhm, Christopher Borgmann, Dr. Sebastian George, Dr. Alexander Herlert und dem Leiter der Kollaboration, Professor Klaus Blaum. Sie alle haben zum Erfolg meiner Messungen maßgeblich beigetragen. Weiterhin danke ich allen Mitgliedern (auch ehemaligen Mitgliedern) der Arbeitsgruppe in Greifswald: Dr. Gerrit Marx, Dr. Noelle Walsh, Steffi Bandelow, Falk Ziegler, Martin Arndt, Martin Breitenfeldt, Franklin Martinez, Albert Vass, Robert Wolf, Christian Droese, Hagen Ritter und Dr. Sudarshan Baruah. Ich möchte mich herzlich bei Ralf Schneider und der COMAS Gruppe für sehr viel Hilfe bei meinen Fragen zu Simulationen und natürlich für die vielen Computer bedanken, die die ausgeführten Simulationen erst ermöglichten. Ebenso danke ich Dr. Stefan Schwarz, der mir Tipps gegeben und ein Programm zur Verfügung gestellt hat, dass für meine Simulationen benötigt wurde. Ich danke allen Freunden und Bekannten die mir in dieser Zeit zur Seite gestanden haben: Janek Lengsfeld, Thomas Schuhmann, Paul Waschkowitz, Oliver Behnke, Steve Zander, Sven Krüger, Thomas Wagner, Helge Grosch und allen Anderen, sowie den Mitgliedern des Do Shin Aikido Vereins und meinem Lehrer Fred Gebler. Alle haben zu mir gehalten, obwohl sie für ein ganzes Jahr sehr oft auf meine Anwesenheit verzichten mussten. Ich widme die Arbeit meinen Eltern Klaus und Hedwiga sowie meiner Schwester Sindy, wegen der vielen Unterstützung aller Art, ohne die diese Arbeit nicht möglich gewesen wäre.